UNIVERSITY OF CALIFORNIA, SAN DIEGO

Modeling diffusion in cerebellar glomeruli

A Dissertation submitted in partial satisfaction of the
Requirements for the degree of Doctor of Philosophy

in

Biology

by

Vladimir Mitsner

Committee in Charge:

Professor Terrence J. Sejnowski, Chair
Professor Darwin K. Berg
Professor Edward M. Callaway
Professor Mark H. Ellisman
Professor Maryann E. Martone

2007

The dissertation of Vladimir Mitsner is approved, and it is acceptable in quality and form for publication on microfilm:

_____

_____

_____

_____

_____

Chair

University of California, San Diego

2007

Table of contents

List of figures

List of tables

Acknowledgements

I would like to thank Olivier Coenen and David Eagleman for their help with calcium modeling. Further gratitude and appreciation goes to Kevin Franks and Tom Bartol who made invaluable contribution to the development of the model. I would also like to thank Peter Thomas for his help in math. I would like to thank Justin Kinney, Dan Keller, Rex Kerr and Jay Coggan for their help in developing the glutamate model and with reconstructions. Of course, this list would be incomplete without mentioning Jed Wing who helped a great deal with some of the programming for analyzing reconstruction geometry. A great deal of my gratitude goes to the computer support people, Jorge Aldana, Chris Adams, Chris Hiestand and Lee Campbell who can finally reboot my computer.

In addition, I would like to tank everyone at NCMIR who had to put up with me. It goes without saying that I would like to thank Ying Jones, who generated the tomograms for me and Masako Terada who converted the tilt series into 3D data.

Lastly I would like to thank my committee for all their help.

Vita

1999	Bachelor of Science, California Institute of Technology
2003	Master of Science, University of California, San Diego
2007	Doctor of Philosophy, University of California, San Diego

ABSTRACT OF THE DISSERTATION

Modeling diffusion in cerebellar glomeruli

by

Vladimir Mitsner

Doctor of Philosophy in Biology

University of California, San Diego, 2007

Professor Terrence J. Sejnowski, Chair

The goal of this dissertation was to examine role played by the geometry of extracellular space in influencing physiological function of neurons. Specifically we examined geometry cerebellar glomeruli – complex synaptic structure whose physiology and morphology indicate that glomerular structure may mediate glomerular function. For one cerebellar glomeruli experience tight glial ensheathment which could limit the rates of ion flow in and out of glomeruli. In addition, several lines of evidence indicate that synaptic connections within glomeruli experience cross-talk via neurotransmitter spillover. Furthermore neurotransmitter receptors whose activation could be dependent on their position as they are placed away from neurotransmitter release sites and potentially close to the neurotransmitter uptake sites. Properties described above implicate a strong relationship between the function of glomeruli and their structure. We chose to further examine this relationship in complex mathematical models of cerebellar function that preserved cerebellar geometry.

Initially we used a stylized glomerular geometric model that aimed to preserve the known structural features of glomeruli. As calcium is an important second messenger that plays an integral role in synaptic plasticity, we, used the model to examine whether the structure of the glomeruli, specifically glial ensheathment could limit the flow of calcium in and out of glomeruli. In addition we investigated whether glutamate - important excitatory neurotransmitter in the glomeruli - could activate sites that lay outside of the release sites. Lastly, we extended the complexity of our model geometry by introducing morphology based on EM tomograms of rat glomeruli where we re-addressed calcium flow into glomeruli and neurotransmitter spillover.

Our results using stylized model showed that calcium flow into the glomeruli is highly sensitive to the degree of glial ensheathment. Moreover, quality of ensheathment, such as the distance to which glial cells wrap around objects entering glomeruli, could influence the rate of calcium flow. We got consistent results using realistic reconstruction with calcium refilling glomeruli with 16 ms time constant. We also showed that high rates of neurotransmitter release in a stylized glomerulus could successfully activate all sites regardless of their position. While time constraints did not allow us to model multiple release events within models based on EM reconstructions, we did model a single release event that showed that activation at distal sites is dependent on the relative position of the distal sites to the release sites.

1. Motivation and Outline.

1.1 Introduction.

1.1.1 Cerebellum.

A useful time saving device commonly found in many airports is a moving walkway. The experience of using this device is an excellent illustration of the brain's ability to rapidly adapt our movement and posture to new circumstances. Imagine a passenger stepping onto a moving walkway. Within a second he is able to successfully adjust to the acceleration, changed surface (from hard marble or cement to the yielding rubber mat), and the sudden disassociation between movement in his visual field and his own motion. Another second passes and he is able to walk on the rolling rubber mat as well as he did on the static hard floor two seconds ago. And he will likely never stop to marvel at how quickly and efficiently his body adjusted its movement to the new surface and new visual experience.

The process that leads to such smooth transition is manifest through intricate cooperation between the brain and the skeletal muscles. Movement commands are analyzed and necessary adjustments made in the context of rapidly changing environmental cues, while the general goal – walking – remains the same. In vertebrate animals, the region in the brain that lies at the center of this flurry of activity is the cerebellum.

One of the primary roles of the cerebellum is to assist in generating smooth and coordinated movements. This was known almost 200 years ago when studies of cerebellar ablations linked function of the cerebellum to motor control as cerebellar damage resulted in postural and movement deficiencies. As the body of knowledge about the function and anatomy of the cerebellum grew, understanding of cerebellar function was expanded to include ability for adaptive on-line motor control (Ito, 1984). In addition, a number of anatomical studies (reviewed in Brodal and Bjaalie, 1997; Middleton and Strick, 1997) and introduction of new techniques, such as positron emission tomography (PET) and functional magnetic resonance imaging (fMRI) have offered a more all-around view of cerebellar function suggesting a role for cerebellum in cognitive tasks such as attention, speech, procedural learning, and others (reviewed in Courchesne and Allen, 1997).

The cells in the cerebellum believed to be responsible for the alacrity of the adaptation described in the first paragraph are granule cells of the cerebellum, located in the cortex (figure 1.1). Specifically, it is theorized that Purkinje cells believed to be responsible for storage and retrieval of different motor adjustment routines must choose the appropriate routine for a given circumstance in the presence of highly overlapping signals carried by mossy fiber terminals. A way to facilitate this discrimination for Purkinje cells is to present them with highly distinctive input patterns for each input entering into the cerebellum. It has been proposed that granule cells of the cerebellum are responsible for this discrimination. It could be achieved by sparcifying granule cell activity, in other words - in the most brute-force way possible – by assigning, as much as possible, a unique set of granule cells to each possible mossy fiber input (Marr, 1969; Albus, 1971; Schweighofer, et al, 2001).

The circuitry of the cerebellar cortex has stereotypic structural motif shown in figure 1.1. Excitatory inputs to the cortex come from the sensory and motor cortex of the cerebrum via pons, from vestibular systems and from the spinal chord. These inputs come in the form of mossy fiber axons that make synaptic connections onto granule cells. Granule cells, in turn synapse onto stellate and basket cells, onto Golgi cells, which in turn make inhibitory connections back onto granule cells, and onto Purkinje cells. The other input to the cerebellar cortex – climbing fibers - come from the inferior olive. They make excitatory connections onto the Purkinje cells. Cerebellar cortex' only output – Purkinje cells - output directly to the deep cerebellar nuclei which make connections back to the spinal chord and the cortex via thalamus. The focus of this discussion are the cerebellar glomeruli - synaptic structures that connect mossy fiber axons that carry vestibular, and somatosensory information into the cerebellar cortex and granule cells – excitatory interneurons of the cerebellar cortex which pass on this information to the Golgi cells (which loop back and make inhibitory connections back on the granule cells in the glomeruli) as well as the Purkinje cells – cells that integrate this information with modulatory feedback that comes via climbing fibers.

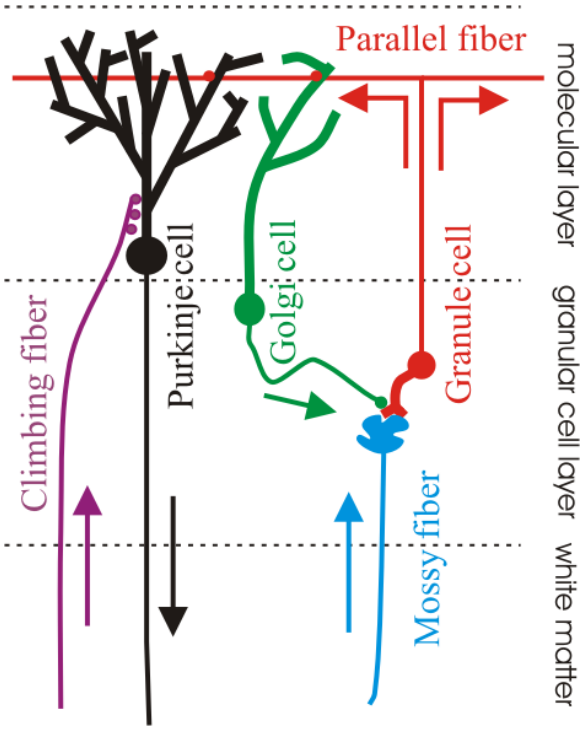

Figure 1.1. Simplified schematic of the circuit of the cerebellar cortex. Different colors indicate different cell types. Arrows indicate the direction of information flow along the axons.
Dendrites are drawn thicker than axons.

1.1.2 Glomerulus Hypothesis.

The reason for our interest in the glomeruli is a hypothesis proposed by David Eagleman and Olivier Coenen that suggests a mechanism by which glomeruli can assist in facilitating adaptation by disambiguating convergent somatosensory information. Such disambiguation is necessary if the inputs to the cerebellum are redundant since removal of such redundancies will facilitate selection of the proper adjustment routines by cerebellar circuits that lie after the glomeruli (Eagleman, et al, 2001).

Consider again stepping on the moving walkway. While some of the somatosensory information channeled to the cerebellum has changed, much has

remained the same. So, the brain must quickly sift through the avalanche of information and select those features that are most relevant for the particular environment and ignore all those that are not relevant. According to the hypothesis, glomeruli would act like filters that sift the incoming data, constantly picking out the most uniquely descriptive message for each environment to send on to the next part of the circuit.

The main principle of the proposed mechanism is based on the observation that glomeruli are tightly ensheathed by a glial cell, where the ensheathment may act as a means of isolating physiological activity inside the glomerulus space from the activity outside. This may allow for a novel type of learning takes place that obeys the following equation

$$\Delta w_i = w_i - a\sum_j s_j w_j \ ,$$

(1.1)

where w_n is the efficacy of the nth MFt to GrC synapse, a is a proportionality constant and s is the activity of the post-synaptic cell. The second term in this equation is usually biologically implausible because it requires that each cell be aware of what how active the rest of the cells are. But, as will be argued below, compartmentalization at the glomerulus provides a way to estimate $\sum_j s_j w_j$ in a biologically plausible way.

1.1.3 Functional isolation is a common feature in cellular function and can occur by means of physical barriers or chemical buffering.

Compartmentalization, defined here as segregation of biophysical activity into spatially separate compartments where the flow of materials between such compartments is actively controlled, is a fundamental feature of the function of all living organisms. An obvious example of compartmentalization is formation of multicellular organisms from single cells. Furthermore, individual cells are also compartmentalized. For example, the internal environment of lysosomes – specialized organelles that are involved in breakdown of cellular components – is kept separate from the rest of cellular cytosol by impermeable membrane, with the

flow of materials between lysosomes and cytosol mediated by specialized proteins. This segregation is important for cells' well being since lysosomes contain acidic hydrolases, which if present inside the cytosol would damage cells. On the other hand, having such specialized compartments allows the cell to increase hydrolases to toxically high concentrations thus improving their recycling efficiency. Imposing a nearly impermeable membrane between two environments is, however, not the only way to localize chemical species. For example, recent simulations that explored calcium flux into a dendritic spine after opening of N-methyl-D-aspartate receptor (NMDAR) pores show that free calcium concentration is relatively high in a small volume near the mouth of the channel, but falls precipitously few dozen nanometers away. This localization is mediated by rapid buffering and removal of free calcium from the cell, creating a calcium "microdomain" where calcium is segregated into a small subvolume. Thus, another way to compartmentalize a particular chemical species is by restricting it to a small subvolume by biochemical means. Such microdomains can also be created in the extracellular space - a giant lake of cerebrospinal fluid that delivers nutrients to cells, maintains electrochemical gradient between inside and outside of cells, and serves as a medium for transmission of signals between cells. There, like in the case of calcium microdomains, they form as a result of structural, such as ensheathment or enclosure and/or chemical restrictions (catalytic enzymes, buffering) on the spread of diffusing molecular species.

1.1.4 Structure of cerebellar glomerulus – structure leads to function?

In this project we explored compartmentalization of extracellular space within a complex synaptic structures called the cerebellar glomeruli. The reason why cerebellar glomeruli were chosen for this study has to do with the idea proposed by Coenen and Eagleman for the function of the glomeruli which links their compartmentalization with a unique information processing function. A stylized image of a cerebellar glomerulus is shown in figure 1.2. Cerebellar glomeruli are complex synaptic structures that participate in transmission of information between the mossy fiber axons and the granule cells in the cerebellar cortex. A typical glomerulus is about 5-10 μm in diameter. At the center of each glomerulus is a

mossy fiber terminal rosette that makes several hundred synaptic contacts onto 20 – 50 thin finger-like granule cell dendrites that wrap around the terminal like tiny claws. Each granule cell makes synaptic contacts on average with 4 different mossy fiber terminals (Jakab and Hamori, 1988, Jakab, 1989; Xu-Friedman and Regehr; 2003; Cathala, et al, 2005). Besides the numerous synaptic contacts, GrC dendrites also form a large number of adhesion junctions (AJ) with one another – which contain functional N-methyl-d-aspartate receptors (NMDARs) (Petralia, et al, 2002; Rossi, et al, 2002). Glomeruli are ensheathed by a thin velate astrocyte (Altman, 1972; Palay and Chan Palay, 1974; Hamori and Somogiy, 1983; Jakab and Hamori, 1988; Jakab, 1989).

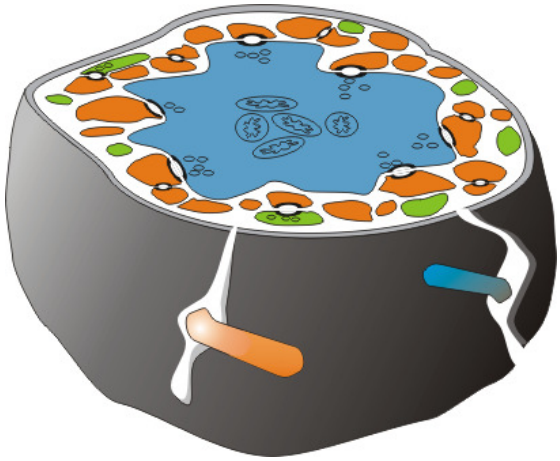

Figure 1.2. A stylized image of a glomerulus. Shown here is a glomerulus with top third cut off. At the center, in blue, is the mossy fiber terminal. In orange are the granule cell dendrites. In green are the Golgi cell axons.

Eagleman and Coenen hypothesized that glomerular architecture may protract activity related depletion of extracellular calcium in the cerebellar glomerulus, whereby the average level of calcium inside the glomerular extracellular space is proportional to the average level of activity of granule cells or to the $\sum w_j s_j$. They were led to that conclusion by two observations. First, the volume occupied by the dendrites contain a significant number of calcium intake elements, such as N-methyl-D-aspartate receptors (NMDARs) on 100 or more different synaptic contacts (Jakab

and Hamori, 1988; Jakab, 1989; Xu-Friedman and Regehr, 2003), and may contain voltage-gated calcium channels (VGCCs) since it was shown that granule cells posses voltage dependent calcium currents (Rossi et al, 1994). Second, glial cell may restrict diffusion of calcium from extracellular space (King et al, 2001; Rusakov et al, 2001). In fact, activity dependent changes in extracellular calcium have been shown in simulations (Smith, 1992; Vassilev et al, 1997; Egelman and Montague, 1998; Egelman and Montague, 1999; Wiest et al, 2000; King et al, 2001; Rusakov, 2001). They were demonstrated with microelectrode recordings (Nicholson, et al, 1978; Benninger, et al, 1980; Zanotto and Heinemann, 1983; Hamon and Heinemann, 1986; Arens et al, 1992; Lucke et al, 1992). And, extracellular calcium depletion was shown experimentally in synaptic structures like the Calyx of Held, where the authors hypothesized that calcium depletion acts to transiently reduce the efficacy of the synapse (Borst and Sakmann, 1999), the calyx-like synapse in the chick ciliary ganglion, where the author suggested that the role of calcium depletion is to act as a limiting factor on the rate of neurotransmitter release (Stanley, 2000) and also at the CA3-CA1 synapse in the hippocampus, where the authors propose that calcium depletion may limit the frequency of response of the post-synaptic cell and may lead to changes in the efficacy of the synapse (Rusakov and Fine, 2003).

What possible role could calcium depletion have in the glomerulus? As mentioned previously – concentration of calcium in the glomerulus would act as a signal that informs all granule cells about the average level of granule cell activity. Furthermore, if granule cell dendrites could monitor the calcium levels in the glomerulus they would be able to glean the value of this average level of activity from the concentration of calcium (Eagleman, et al, 2001).

This circumstance would allow for implementation of the learning rule described in the equation 1.1 allowing individual glomeruli to sparcify the granule cell activity as the strength of the mossy fiber to a given granule cell would decrease if many granule cells are active at the same time and would increase if few granule cells are active at the same time as shown in figure 1.3. Thus the structure of the glomeruli may be linked directly to an information processing function of the granule cell layer in the following manner. Simultaneous activity of many granule cell

dendrites in a glomerulus would lead to a large drop in extracellular calcium thereby causing a negative change in w_n. Thus, over time all the granule cells that fire together will have their synaptic contacts with mossy fiber weaken in a glomerulus. On the other hand granule cells that fire alone will have their synaptic contacts strengthen over time.

1.2 Outline of the dissertation.

The goal of the research in this thesis was to explore the structural influence on signaling in a cerebellar glomerulus using computational methods. MCell – a computational tool specifically optimized for simulations with arbitrary geometric complexity – was used to investigate the manner in which the tightness of and the shape of glial ensheathment of a glomerulus contributes to isolating diffusion of calcium (Ca^{++}) in and out of a glomerulus. In addition we explored possible consequences that a tight glial ensheathment may have on the state of extracellular Ca^{++} concentration inside a glomerulus. Besides looking at Ca^{++} we also used MCell to examine diffusion of glutamate inside the glomerular space, focusing on

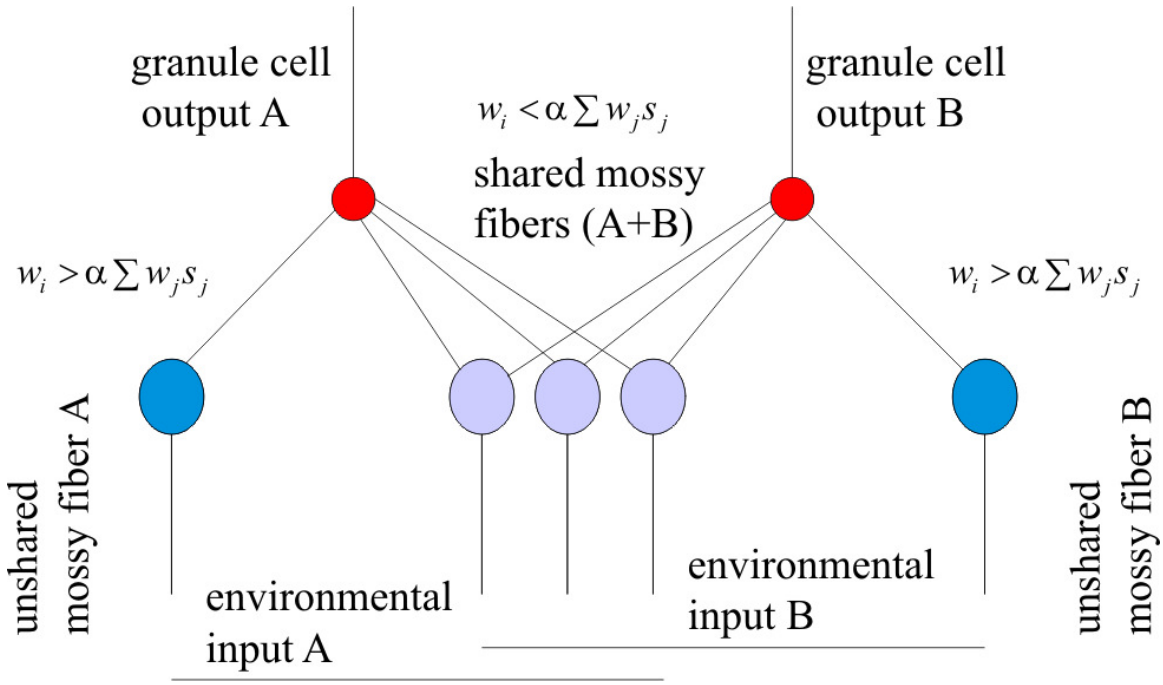

Figure 1.3. Simplified illustration of the application of the learning rule. 2 granule cells (red) receive input from 4 mossy fiber terminals (light and dark blue) each. For each of the granule cells, 3 of the mossy fibers are shared between the granule cells (light) and 1 is unshared. Initially whenever input A or B is presented both granule cell A and granule cell B should be active, thus making inputs A and B undistinguishable. As environmental inputs A and B are presented to the granule cells synaptic contacts between granule cells and "shared" mossy fibers should weaken as both granule cells would be active causing high levels of activity leading to the reduction of the connection strength between those mossy fibers and the granule cells. On the other hand, the synaptic contacts between the "unshared' mossy fiber terminals and the granule cell dendrites should strengthen. Ultimately, application of the algorithm would create a situation where presentation of input A would only activate granule cell A and presentation of input B would only activate granule cell B.

glutamate spillover through the entire glomerular volume and on glutamate leaks between two nearby glomeruli. For some of our investigations we used stylized models of the glomerular geometry. Later on we were able to obtain from National Center for Microscopy and Imaging Research (NCMIR) two tomographic

reconstructions of rat cerebellar glomeruli, which we used to explore the effects of realistic structural variability on diffusion of glutamate and Ca^{++} in a glomerulus.

Not as much is known about cerebellar glomeruli as other brain structure such as the CA1- CA3 synapse in the hippocampus, so many of the parameters used in this study were varied through broad physiologically relevant ranges. This dissertation is an exploratory study that focused on those structural parameters that play the greatest role in signaling inside a glomerulus. It is arranged as a series of stand-alone chapters that follow the development of the Ca^{++} and glutamate models (chapters 2 and 3), and conclude with implementation of some of those models within model geometry based on realistic tomographic reconstructions (chapter 4).

1.2.1 Chapter 2: Modeling depletion of extracellular Ca^{++} in cerebellar glomeruli.

In chapter 2 we investigate whether hypothesis that Ca^{++} fluctuations within a realistic glomerulus is physiologically plausible. To do so we constructed a model of a cerebellar glomerulus and tested the manner in which different parameters responsible for Ca^{++} influx and extrusion affect fluctuations in the extracellular Ca^{++}.

1.2.2 Chapter 3: Modeling of activation and of time course of extrasynaptic NMDAR Ca^{++} currents.

In chapter 3 the original model was extended and modified to include glutamate release and diffusion. Using the model we investigated the efficacy of glutamate spillover through the model volume during different mossy fiber activity regimes. In addition we examined glutamate leakage between neighboring glomeruli.

1.2.3 Chapter 4: Investigation of realistic glomerular geometry – a modeling study.

In chapter 4, a model geometry based on realistic tomographic reconstructions of rat cerebellar glomeruli is introduced and used to measure the effective geometric tortuosity in the two reconstructions and to investigate variability in spillover glutamate access to extrasynaptic sites.

2. Modeling Calcium depletion in cerebellar glomeruli.

2.1 Introduction.

In many cellular processes that involve calcium (Ca^{++}), increase of cytosolic calcium is a result of influx from extracellular space (ECS) – a complex contiguous network of fluid filled with various molecular species – that surrounds each cell. Such influx would necessarily result in a transient drop in the concentration of Ca^{++} outside the cell ($[Ca^{++}]_o$). If the recovery rate of $[Ca^{++}]_o$ was slower than the rate of Ca^{++} removal, then such an arrangement would make $[Ca^{++}]_o$ a shared resource competed for by nearby cells. The hypothesis that extracellular calcium is a shared resource has been supported by several theoretical studies which demonstrate that local extracellular calcium concentration decreases as a result of neuronal activity (Smith, 1992; Eagleman and Montague, 1998; Vassilev, et al, 1999; Eagleman and Montague, 1999; King, et al, 2000; Wiest, et al, 2000; King, et. al., 2001; Rusakov, 2001). This hypothesis is further supported by microelectrode recordings which show activity dependent changes in extracellular calcium in-vivo (Nicholson, 1978) and in vitro (Benninger, et al, 1980; Zanotto and Heinemann, 1983; Hamon and Heinemann, 1986; Arens, et al, 1992; Lucke, et al, 1995). In addition to global changes in Ca^{++} concentration, there is also evidence that supports the idea of activity-dependent calcium depletion at synapses – at the calyx of Held in the rat auditory brainstem (Borst and Sakmann, 1999), at a calyx-type synapse in the chick ciliary ganglion (Stanley, 2000), and in the rat hippocampus (Tang, et al, 1998; Rusakov and Fine, 2003). In this chapter we describe a modeling study of activity-dependent fluctuations in extracellular Ca^{++} concentration at synaptic structures called cerebellar glomeruli.

Cerebellar glomeruli are large complex synaptic structures encased in a tight glial sheath (Palay and Chan-Palay, 1974; Landis, 1986; Jakab and Hamori, 1988; Jakab, 1989). Within the space enclosed by glomerular glia there are several hundred active zones (Xu-Friedman and Regehr, 2003), which can become permeable to Ca^{++} simultaneously at rates > 100 Hz (Garwicz, 1998). In addition, this space contains a large number of n-Methyl-d-Aspartate (NMDA) receptor-containing dendrites, and

which were shown to fire in short bursts at rates ~ 80 Hz (Chadderton, et al, 2004). Furthermore, granule cells contain a variety of high voltage activated Ca^{++} channels. (Maex and DeSchutter, 1998).

In this chapter we investigated the hypothesis that the tight glial ensheathment of the glomerular synaptic structures in the granule cell layer of the cerebellum is responsible for a structural isolation of extracellular space of the glomeruli. Thus the influx and the efflux of extracellular ionic species such as H^+, K^+, Ca^{++} and others into and out of the glomeruli would depend on the tightness of the ensheathment. In our work, we chose to concentrate on Ca^{++} concentration since it is an important second messenger whose changes may affect release probability, synaptic plasticity, and structural stability of the glomeruli.

Our study was performed in a model of cerebellar glomeruli that attempted to capture the details of their morphology and physiology based on past experimental measurements. Where those details were unavailable, a parameter sweep within a biologically realistic range was performed. Our results showed that extremely tight ensheathment of the glomeruli could lead to changes in the extracellular concentration of Ca^{++} inside the glomeruli whereby the resulting concentration is the function of activity in the glomeruli. Creating leaks in that ensheathment however, allowed for rapid Ca^{++} re-equilibration leading to attenuation of the drops in extracellular Ca^{++}. Lastly, we examined the time course of glomerular refilling as we varied structural parameters that affect the rate of Ca^{++} influx. The results showed that glomeruli should refill within ~ 10-100 ms given spacing between cells in the glomerulus observed in the EM reconstructions.

2.2 Methods.

Because of the technical difficulties associated with measuring $[Ca^{++}]_o$ in vivo and because of difficulties associated with simulating activity of a large number of granule cells that have to belong to one glomerulus, we decided that as a first step in our study we would simulate Ca^{++} fluctuations in model glomeruli. Computer simulations were performed in simplified NEURON (Hines, 1989, 1993; Hines and

Carnevale, 1997) model of granule cells and in a detailed stylized MCell model of a cerebellar glomerulus.

2.2.1 Calcium fluctuations model in Neuron:

The NEURON model used for describing the granule cells was based on the Maex and DeSchutter 1998 model of the rat granule cell at 37 ^{o}C. Due to their electrotonic compactness granule cells can be simulated as single compartments (Silver, et. al, 1992; Bardoni and Belluzzi, 1993; D'Angelo, et al, 1993, 1995, 2001). All rate constants were adjusted for the temperature increase from 20 ^{o}C to 37 ^{o}C– a Q10 factor of 3 meant that they were all multiplied by a factor of 5 (De Schutter and Bower, 1994a; Maex and DeSchutter 1998).

The neuron model consisted of 50 granule cells, 50 GoC inputs and 151 MF inputs. Inputs to each of the granule cells consisted of 4 MF firing trains and one GoC firing trains. Of the 4 MF inputs, 3 were chosen without replacement from 150 Poisson-generated 1 sec-long firing trains and the fourth MF firing train was kept constant for all of the 50 granule cells, thus corresponding to the activity of the MF located inside the glomerulus of interest. Each of the GoC firing trains was chosen without replacement from 50 Poisson-generated 1 second long firing trains. The GoC inhibitory input was injected into the granule cells only for the purpose of changing GrC firing rates while maintaining a constant MF firing rate. The finding that GABA released from GoC's can inhibit release from MFt (Mitchell and Silver, 2000) and that Glu released from MFt can inhibit GoC release of GABA (Mitchell and Silver, 2000) were not included in these simulation because we used high MF firing rates and second because we are not interested in simulating realistic GoC firing. Parameters of the model channel kinetics are given in appendix B.

The output of the NEURON models were one-second long time series of open probability for the high voltage activated (HVA) Ca^{++} channels as well as for the NMDAR channels. Those were converted into time series of kinetic rates of a two-state Markof process with a time-varying opening rate and a constant closing rate, and the calcium current was converted into MCell-conductivity term which relates ionic current to ionic concentration. (Figure 2.1 shows an example of the two types of

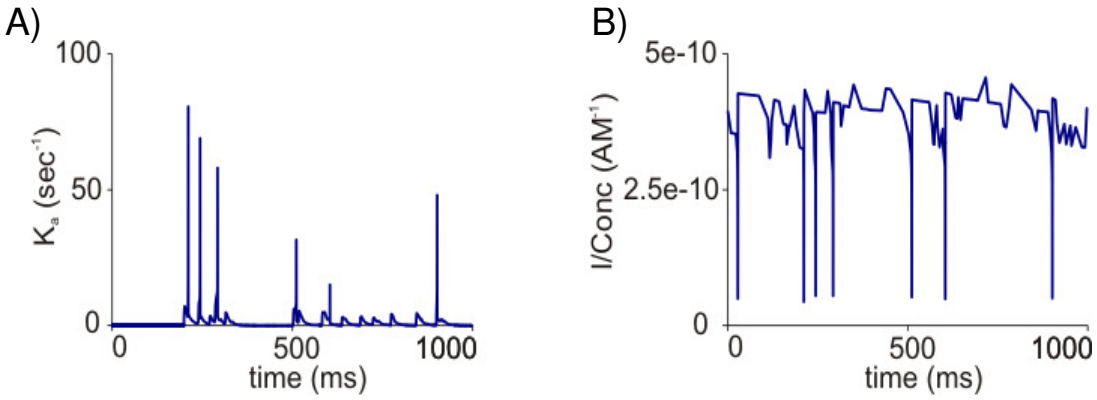

Figure 2.1. Sample time courses of kinetic rates of the NMDAR current of a granule cell and of MCell-conductivity of calcium current through the NMDAR channel.

A) Opening rate (K_a) of the channel as a function of time. Channel opening is assumed to be a 2 step Markof process with a constant closing rate (K_b = 1000 sec^{-1}) and a time varying opening rate - $K_a(t)$, which is derived from the following equation

$$P_{open}(V,t) = R(V,t)/R_{tot} = K_a(t)/(K_a(t) + K_b), \qquad (1)$$

where $P_{open}(V,t)$ is the time course of open probability of the channel as a function of voltage. It was calculated by taking $R(V,t)/R_{tot}$ – ratio of the number of open channels to total channels as a function of voltage and time – obtained from a NEURON simulation.

B) MCell-conductivity is defined as current divided by concentration as a function of time. Since almost all of calcium current is inward, we only use the inward current component of the Goldman Hodgkin Katz (GHK) equation:

$$I_{inward}/[Ca^{++}]_o = -PzF\xi e^{-\xi}/(1-e^{-\xi}) \ , \qquad (2)$$

where

$$\xi = zV(t)F/RT \ , \qquad (3)$$

and z is the charge of calcium ion = 2, F is the Faraday's constant = 96480 Coul/mol, $V(t)$ is the time course of membrane potential derived from NEURON, R is the gas constant = 1.98 cal/(^{o}K*mol) and T is the temperature in degrees Kelvin. P is the permeability of channel to calcium. To determine P, we assumed it to be constant with respect to $[Ca^{++}]_o$, then we derived P by setting the calcium conductance of NMDAR channel at 2mM $[Ca^{++}]_o$ to 4 picosiemens (Cull-Candy et al, 2001). P = 1.7x10^{-13} L/sec per channel patch.

curves that were fed into the MCell simulations. Appendix 2.A explains how macroscopic Ca^{++} current was converted into microscopic transition probability). Mossy fiber terminal electrophysiology was simulated in a similar manner, except the electrophysiological model was simpler, containing only Hodgkin-Huxley Na^{+} and K^{+} currents and a single high voltage activated Ca^{++} current, which was prepared for MCell simulations using Neuron. Golgi cell electrophysiology was not simulated in these studies. Similar methods were used in simulation of voltage-dependent Ca^{++} currents in the dendritic spines (Franks and Sejnowski, 2002).

2.2.2 Calcium fluctuations model in MCell.

All simulations that involved 3D structures were done in MCell – a Monte Carlo simulator of cellular biophysics (Bartol, et al, 1991; Stiles et al, 2001; Stiles and Bartol, 2001). MCell uses rigorously validated and highly optimized Monte Carlo algorithms to simulate the random-walk Brownian motion of discrete diffusing molecules and concomitant uni- and bi-molecular chemical reactions in a complex three-dimensional environment reflecting realistic cellular microstructure. MCell has been used to model vesicular release (Stiles et al., 2001), diffusion in the synaptic cleft (Franks et al., 2002), and investigate the impact of neuronal shape on tortuosity (Tao and Nicholson, 2004).

The 3D structure of the model glomerulus was designed with the intent to capture previously known geometric features of glomeruli. The geometric parameters use to constrain the model were glomerular volume and surface area, the volume and surface area of the mossy fiber terminal, the fraction of glomerular volume occupied by the dendrites, and the extracellular volume fraction. The last parameter was maintained at 11%. The other parameters were based on serial electron microscopic investigations of rat glomeruli described in Jakab and Hamori, 1988 and Jakab, 1989. In figure 2.2 (A) we show a stylistic drawing of a cerebellar glomerulus. In the drawing the top $1/3^{rd}$ of the glomerulus has been cut off and only the tops of the dendrites and the axons are visible. In the image, the basic principle of the glomerular structure – i.e. – a mossy fiber terminal at the center (blue) surrounded by a swirl of dendrites and axons (orange) with the entire structure being ensheathed by a

glial cell (gray). Figure 2.2 B shows the structural pattern of the model with the colors associated with structures in figure 2.2 B matching the color-identity relationship in figure 2.2 A. Thus, the large blue box in the center

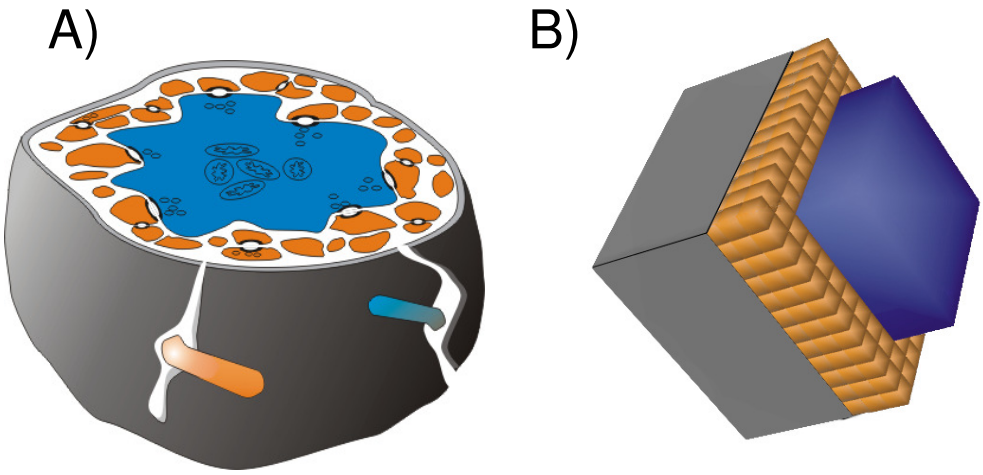

Figure 2.2. Comparison of stylized glomerulus and model geometry.

A) Image of a cerebellar glomerulus based on EM reconstructions. Blue mossy fiber terminal is surrounded by orange granule cell dendrites and Golgi cell axons. Granule cell dendrites receive synaptic connections from both the mossy fiber terminal and from the Golgi cell axons. (Golgi cell activity was not simulated). The entire structure is surrounded by a gray glial cell.

B) Image of the model of cerebellar glomerulus. Blue box that represents the mossy fiber terminal core is surrounded by a series of orange boxes that represent the axo-dendritic millieu. The entire object is surrounded by a glial sheath.

represents the mossy fiber terminal core. The grid of small orange boxes corresponds to the axo-dendritic milieu. And the glial sheath is represented by the gray box. The dimensions of the large central cube are 3.34 μm along each coordinate axis; of the smaller cubes: 0.4 μm along each coordinate axis; of the glial sheath: 5.06 μm along each coordinate axis. The space between all surfaces is 20 nm wide. In the image 2.2 B, glial sheath was partly peeled and axo-dendritic cubes were removed to reveal objects underneath. In actual simulations, axo-dendritic boxes fully surrounded the

mossy fiber terminal core and glial sheath was fully wrapped around the axo-dendritic cubes.

2.2.3 Calcium fluctuations model - physiological model.

The standard parameters of our simulations for dendrites were: voltage gated calcium channel (VGCC) density = 2/μm with the peak current of 8 pS (Magee and Johnston, 1995); NMDAR per synapse = 20 with peak Ca^{++} current of 4pS (Franks, et al, 2002); extrusion time constant = 300 ms (Markram, et al 1995); for mossy fiber terminal (MFt): VGCC number per synapse = 20 with peak Ca^{++} current of 8 pS; Helmchen, et al, 1997, extrusion time constant = 60 ms (Helmchen, et al, 1997; Sinha, et al, 1997; Koester and Sakmann, 2000).

Ca^{++} consumption and extrusion functionality was introduced into the model by seeding the surfaces of the boxes with the receptors and channels whose parameters were described above. As mentioned in the previous section, time courses of the Ca^{++} consuming probabilities were fed into MCell based on NEURON simulations of granule cell activities. Calcium extrusion was modeled as a 2-state Markof process that generated extrusion with constant rate. NMDA receptor-containing synaptic contacts were regenerated in the following way: 150 sites of apposition between the dendritic surfaces and the MFt surfaces were chosen at random. A square of 0.2 μm x 0.2 μm was selected on the dendritic cube co-centric with the face of that cube. Then an identical 0.2μm x 0.2μm surface was selected on the apposing MFt surface so that a line perpendicular to the two squares going through the center of one square would intersect the other square at a point <0.01 μm from the center of the latter square. These squares represented the PSD and the active zones respectively and they were populated in the following manner: the presynaptic square was populated with pre-synaptic VGCC's and the postsynaptic square was populated with NMDAR channels. The remaining dendritic surfaces were populated with dendritic VGCC's and with dendritic calcium extrusion mechanisms and the remaining MFt surfaces were populated with MF calcium extrusion mechanisms.

Unless otherwise stated, glial ensheathment was complete, i.e., the entire glial sheath surface acted as a reflexive boundary and no calcium ions could enter or leave

the model glomerulus. The last step in creation of the model was to invade the spaces between meshes with calcium ions. Calcium diffusion coefficient was adjusted for the tortuosity of the model. After the adjustment it was set to $3*10^{-6}cm^2/sec$. Ca^{++} diffusion was modeled as a 3-D random walk. We used a time-step of 1 μs.

2.2.4 Ca^{++} refilling model.

The structural model for the refilling simulations mostly reused the same structure as the model for Ca^{++} fluctuations. The only changes were made at the periphery where instead of modeling glial sheath as a simple cube, we created a more complex shape that included rectangular extrusions that represented glia extending and wrapping around dendritic or axonal shafts that enter into the glomerulus. The actual dendritic shafts were represented on the inside with rectangular tubes, whose width was adjusted to simulate the degree of tightness of glial ensheathment. Full details of the model setup are given in figure 2.3 and Table 2.1.

The 6 surfaces on the tips of the extrusion were modeled as sources/sinks of Ca^{++} in such a way as if the glomerulus is being washed by a solution with constant $[Ca^{++}]$. This was done by seeding these surfaces by effectors that generated Ca^{++} at a constant rate. Ca^{++} was removed by setting the patches to a state that would remove every Ca^{++} particle that came in contact with the surface. Thus at steady state the number of Ca^{++} ions just inside the volume would be such that the rate of calcium generation would match the rate of calcium removal.

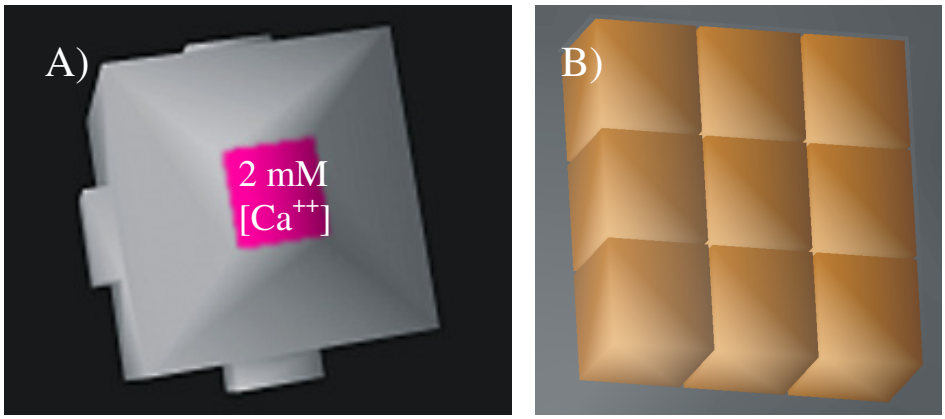

Figure 2.3. Geometric setup for the Ca^{++} refilling model.
A) Glial sheath has 6 (~1.5 mm x 1.5 mm x Z mm) extrusions. At the tip of each extrusion was a 2 mM source of Ca^{++}. (Z is given below in the table 2.1).
B) Inside each of the glial extrusions we placed a set of 6 boxes that represented dendritic stems. The gap between them was varied to recreate possible different gap sizes between cells.

Table 2.1. Parameters used in the simulations of Ca^{++} refilling of a glomerulus.
* surface area of "holes" / % of total surface area of the original box occupied by "holes".

height of glial sheath = Z	surface area of holes*
2 µm	6.14 μm^2 = 4 %
1 µm	3.07 μm^2 = 2 %
0.5 µm	1.54 μm^2 = 1 %
0.25 µm	0.77 μm^2 = 0.5%
0.02 µm	0.38 μm^2 = 0.25%

2.3 Results.

2.3.1 [Ca^{++}] fluctuations with complete glial ensheathment with standard parameters.

With 100% glial ensheathment, $[Ca^{++}]_o$ consistently decreased to a new steady-state level. Figure 2.4 (A) compares $[Ca^{++}]_o$ fluctuations in 2 sample simulations of glomeruli where the average granule cell activity level was either 7 Hz or 24 Hz. In the 24 Hz simulation $[Ca^{++}]_o$ appears to reach a lower steady state. This is consistent with the fact that the extrusion of Ca^{++} in the simulations was slow enough to allow different Ca^{++} consumption rates to lead to different steady state concentrations of extracellular Ca^{++}. In both simulations Ca^{++} time course has a peculiar profile, characterized by large sudden drops followed by slower recovery. These drops indicate mossy fiber Ca^{++} influx events. These events are not surprising considering they occur as a result of near simultaneous activation of all of the HVA Ca^{++} currents on the mossy fiber terminal.

Will the drops in $[Ca^{++}]_o$ behave similarly for a variety of firing patterns? Figure 2.4 B shows that the average drop for 10 different sets of firing trains with the same granule cell mean rate of 24 Hz will consistently be larger than the average drop for 10 different sets of firing trains with the mean granule cell firing rate of 7 Hz. The "average" time course of $[Ca^{++}]_o$ for both 24 Hz simulations and 7 Hz simulations was fitted with an exponential of the form

$$[Ca^{++}]_o = (2mM - C_{st}) * e^{-t/T} + C_{st}, \qquad (2.4)$$

where t is time, T is the time constant of the drop and C_{st} is the new steady state level in figure 2.4 C. The length of time required to do each simulation (several months) made it difficult to vary parameters with many different trains of granule cell activity. As shown in figure 2.4D, single trial time courses of $[Ca^{++}]_o$ could also be fit with equation 2.4.

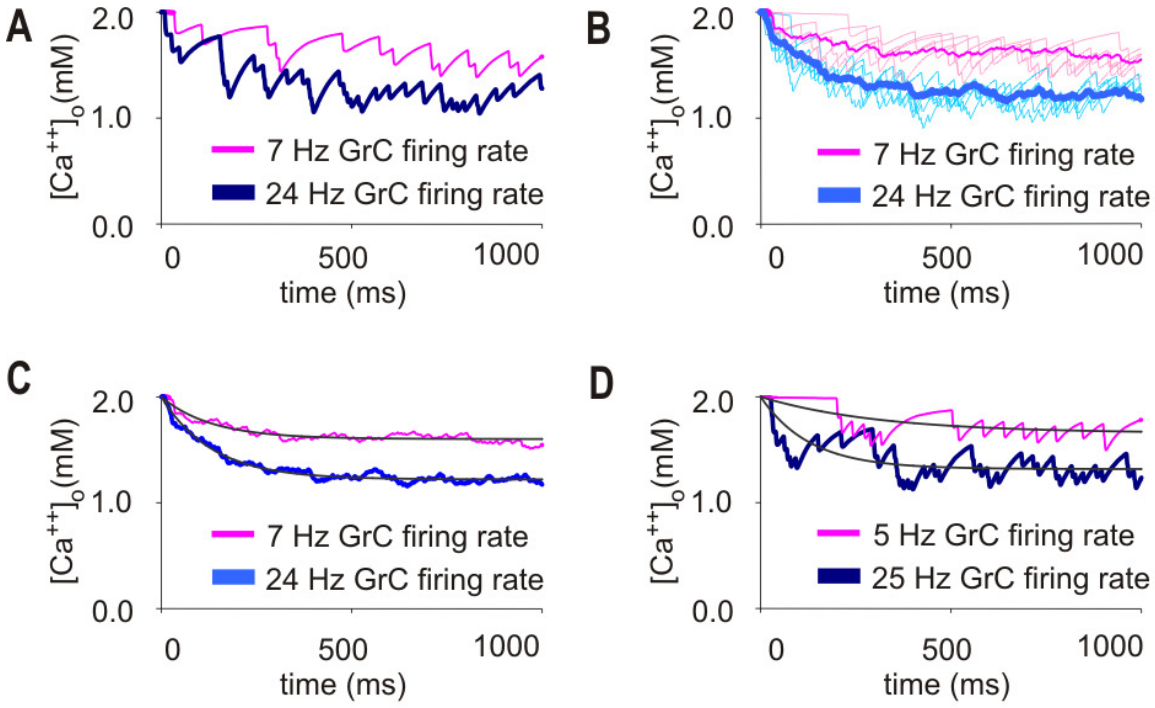

Figure 2.4. Extracellular calcium concentration falls to a new steady state level.
A) Comparison between two simulations shows that higher activity leads to greater decrease in extracellular calcium.
B) Both conditions were repeated 10 times with different input spike trains at the same rates of activity. Higher activity consistently leads to lower extracellular calcium.
C) Average traces from part B were calculated for both activity patterns and fitted with the following equation 2.4.
D) Single traces from another set of firing trains are given and we show that they can be fitted with a similar equation as in part C. For 25 Hz C_{st} = 1.32 mM and for 5 Hz C_{st} = 1.64 mM.

2.3.2 Varying parameters of Ca^{++} extrusion and consumption.

We wanted to establish the range of Ca^{++} fluctuations as a function of varying extrusion and consumption parameters since, as mentioned previously, the original parameters were only estimated based on measurements made in other cell types and brain regions. We ran 2 sets of stimulus trains with mean rates of 25 Hz and 2

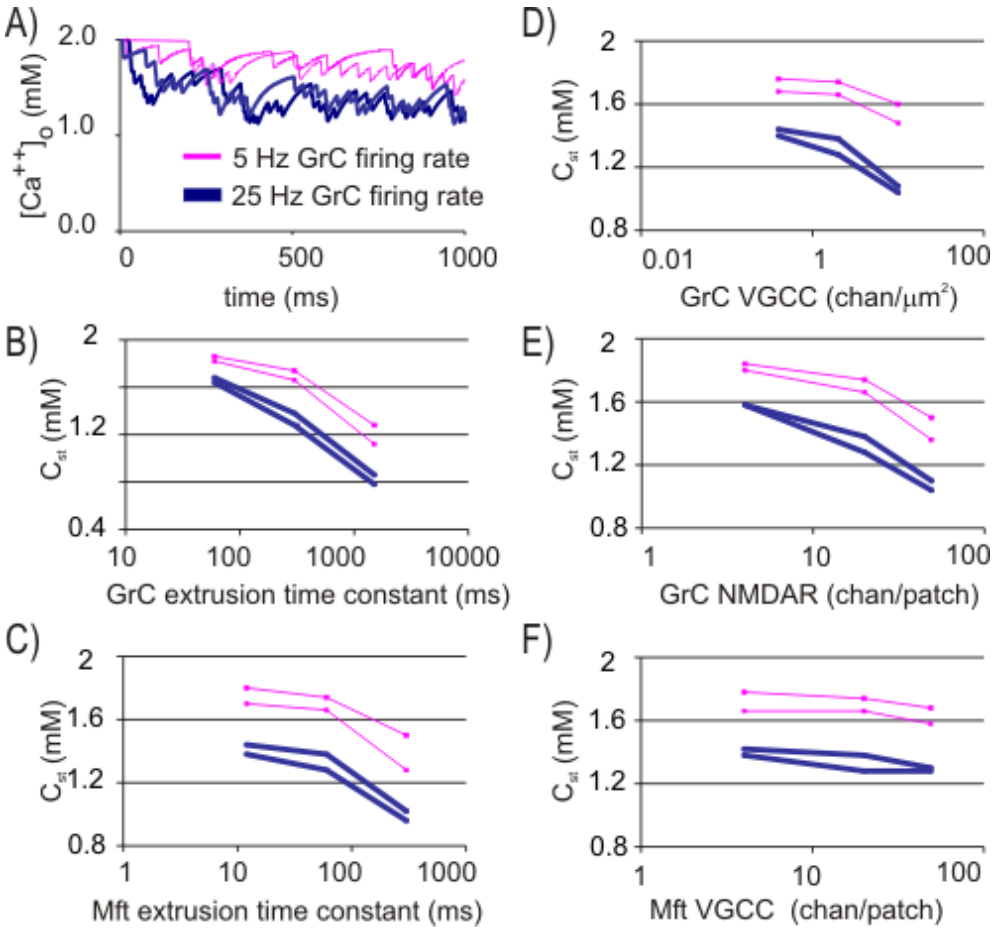

Figure 2.5. Changing calcium intake and extrusion parameters changes C_{st}.
A) Two pairs of firing train sets that generate 5 Hz or 25 Hz average activity are given with standard parameters.
In B-F) One parameter is changed as described below while the rest are held constant the same. Just like in A, thin magenta lines correspond to the 5 Hz simulations and think dark blue lines correspond to the 25 Hz simulations.
B) Extrusion rate in the granule cell dendrites was increased or decreased by a factor of 5.
C) Extrusion rate in the MFt was increased or decreased by a factor of 5.
D) Density of VGCCs on the granule cell was increased or decreased by a factor of 5.
E) Number of NMDARs on the post-synaptic patches was decreased by a factor of 5 and increased by a factor of 4.5*.
F) Number of VGCCs on the MFt presynaptic patches was decreased by a factor of 5 and increased by a factor of 4.5*.
* Maximum density of channels allowed by MCell (10000 chan/μm^2) reached.

sets of stimulus trains with the mean rate of 5 Hz through all of the changes in the Ca^{++} consumption and extrusion variations. The results of these simulations are shown in figure 2.5. In figure 2.5 (A), we again show that the higher activity rates lead to greater drops in $[Ca^{++}]_o$. In figures 2.5 (B-G), we show results for simulations where we held all of the parameters but one constant. The results are presented as new steady state $[Ca^{++}]$ as the function of the varied parameter. Figure 2.5 (B) shows that the decreasing the rate of Ca^{++} extrusion in the granule cells leads to an increase in the drop of the $[Ca^{++}]_o$. The same was the case with the increase in the extrusion in the mossy fiber terminal shown in figure 2.5 (C). In addition, increase in the consumption of Ca^{++} by granule cells resulted in the lower steady state $[Ca^{++}]_o$. Interestingly, increasing consumption of Ca^{++} by mossy fiber terminal did not result in a greater decrease of Ca^{++}. This was due to the high extrusion rate of Ca^{++} from the mossy fiber terminal.

2.3.3 Incomplete glial ensheathment

In the previous simulations we assumed that the glial sheath completely encased the glomerulus. It is likely, however, that the glial ensheathment is not complete for a number of reasons. First, in many experiments receptor agonists or antagonists are applied in solution and are able to find their way into the glomerulus. Second, the glomerulus is made up of dendrites and axons that are attached to objects which are mostly located outside of the glomerulus, so at the site where these objects penetrate through the glial sheath layer the glial cell may maintain some sort of a gap between itself and the axon and the dendrite.

For leaks in the glial sheath we estimated that roughly 1% of the total surface of the exterior of the glomeruli will be devoid of glia. This is based on the assumption that if 50 nearly cylindrical dendrites with an average radius of 0.25 μm retain a 20 nm gap with the glial sheath as they enter it. Given the above assumption the total gap will be ~1.5 μm^2 since the total surface area of the completely ensheathing glia in our simulations was ~ 153.6 μm^2.

We created holes in the glial sheath and assumed that the concentration outside remained at 2 mM. The glial sheath setup is the one given in figure 2.3 where

the settings were height = 0.02 µm and the surface area ratio was 1%. Doing so and running

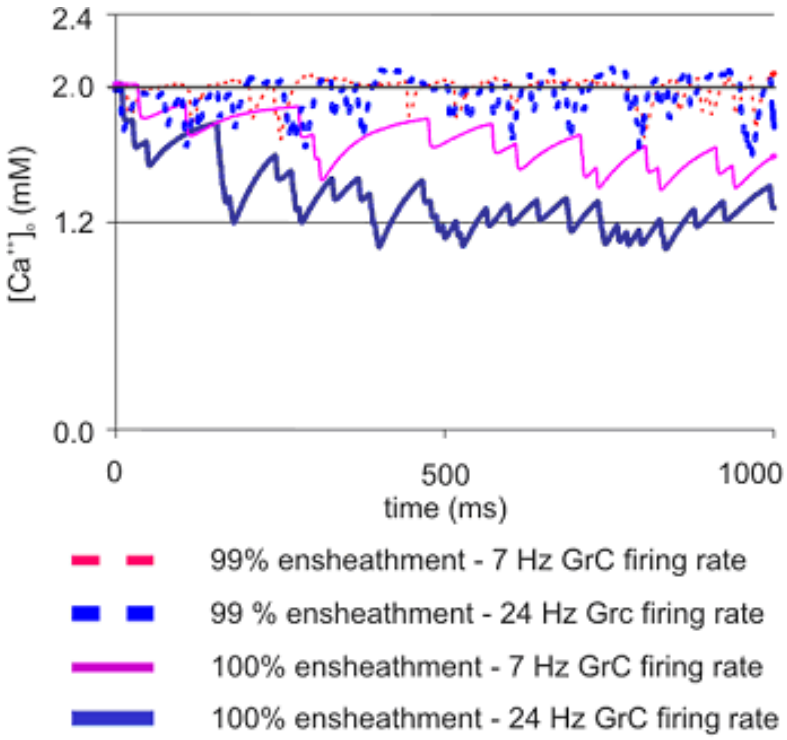

Figure 2.6. Fluctuations in extracellular calcium in the case of 99% ensheathment vs. 100% ensheathment. In the case of incomplete ensheathment, extracellular calcium no longer reaches a new steady state. 100% ensheathment corresponds to the case where the entire glial sheath surface acts like a reflective boundary. 99% ensheathment corresponds to the case where 1% of the glial sheath surface is perforated with holes.

the simulation with original calcium consumption and extrusion parameters resulted in no observable drop to a new steady state concentration as shown in Figure 2.6. Even though $[Ca^{++}]_o$ fell for short periods of time, it recovered back to 2 mM within 10's of ms and, at times, it overshot the 2mM concentration. Results of these simulations imply that though in realistic circumstances concentration of Ca^{++} inside of the glomeruli will be sensitive to the $[Ca^{++}]$ outside of the glomeruli.

2.3.4 Glomerular refilling.

Since our measurements indicated that tightness of the glial ensheathment is an important parameter that can have significant influence on the nature of activity-dependent Ca^{++} fluctuations in a cerebellar glomerulus, we decided to measure how changes in the quality of ensheathment affect Ca^{++} flux into a glomerulus.

In order to model realistic leaks into a glomerulus, we would have needed to simulate a volume many times larger than the proper glomerulus. To reduce compute times we opted for a limited investigation of Ca^{++} flow into a glomerulus. In effect, we replicated an experiment where a glomerulus is excised from the brain and placed into a solution, which is constantly held at 2mM Ca^{++}.

We investigated how fast Ca^{++} from the outside of the glomerulus can leak inside of the glomerulus if we changed the manner in which glial sheath wraps around the dendrites. It has been shown previously (King, et al, 2001) that increasing the size of holes leads to an increase in the re-equilibration rate. We extended those ideas by comparing the results of increasing holes in the glial sheath while at the same time changing the extent to which glia wrap around the dendrites as described in figure 2.3.

Our results shown in figure 2.6 indicate that at the extreme tight glial ensheathment can lead to very long refilling times, however based on observations of EM tomographic constructions of various rat glomeruli (generously provided by NCMIR), we conclude that the most likely refilling times would be in the range of 30-100 ms.

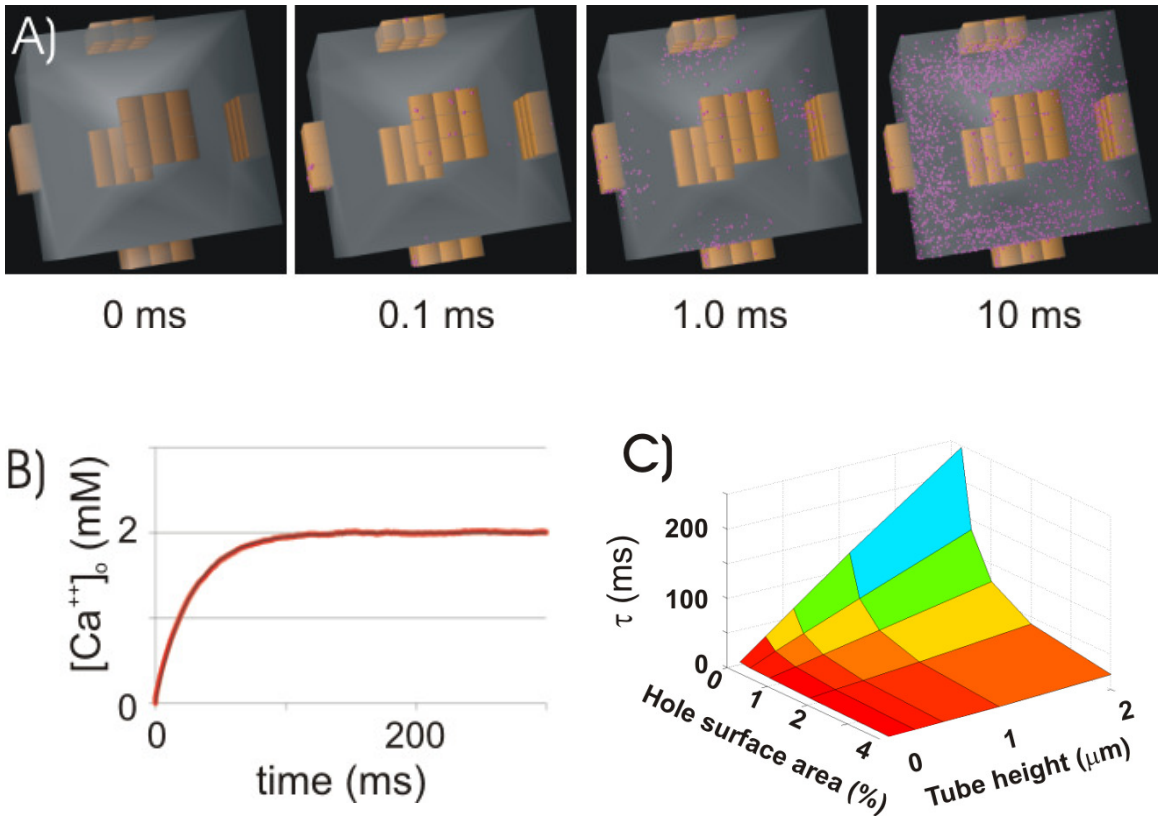

Figure 2.7. Ca^{++} refilling of model glomerulus.

A) Sample time course of calcium influx into the model glomerulus. Calcium (purple spheres) originates at the peripheral surfaces of the extrusions and then flows into the center. For clarity, the grid of axo-dendritic cubes and the central mossy fiber core were not shown in the image. But at 10 ms, enough Ca^{++} is present to outline the shapes of those structures.

B) Sample plot of the time course of Ca^{++} refilling of the model glomerulus. All such time courses were fitted with an exponential.

C) The time constant of the exponential was plotted as a function of height of cubes and size of holes in the glial sheath.

2.4 Summary

2.4.1 Cerebellar glomeruli.

In this chapter we examined the effects of activity in a synaptic structure called cerebellar glomeruli - complex structures composed of as many as 50 claw-shaped granule cell dendritic terminals that make synaptic contacts with an excitatory mossy fiber axon terminal rosette (Palay and Chan-Palay, 1974; Jakab and Hamori, 1988; Jakab, 1989). The glomerulus is tightly ensheathed by a velate astrocyte (Landis, et al, 1986).

Our results showed that Ca^{++} fluctuations in the glomeruli were sensitive to the level of activity of the granule cells and to the extrusion rates of Ca^{++} if the glomeruli were tightly ensheathed. Specifically $[Ca^{++}]$ went down and remained at a new lower steady state level for the duration of the activity of granule cells. Such behavior could potentially allow extracellular Ca^{++} to serve as a global messenger of the overall activity in the glomerulus. (Eagleman, et al, 2001) Creating leaks in the glial sheath with constant 2 mM Ca^{++} outside the sheath, however, abolished such drops to new steady state levels, indicating that under realistic circumstances information about the activity of elements outside the glomerulus would leak into the glomerulus. For example, if a nearby glomerulus were active then the reduced rate of Ca^{++} influx would falsely indicate higher activity levels.

In this chapter we also examined how varying the parameters of ensheathment would influence the rate of Ca^{++} re-equilibration and effectively influence the rate of contamination of information carried by the extracellular Ca^{++} inside a single glomerulus.

We varied extrusion and consumption of Ca^{++} and observed that increasing consumption leads to greater drops in the level of Ca^{++} and that increasing extrusion leads to smaller drops in the level of Ca^{++}.

The glial sheath may incompletely enclose the glomerulus, we repeated the original simulations within a geometry that allowed for replenishment of Ca^{++} from volume outside of the glomerulus. This resulted in elimination of a persistent drop in $[Ca^{++}]$ to lower levels.

We explored this result further by investigating how changes in the quality of ensheathment would affect the rate of Ca^{++} flow into our model glomerulus. Our results showed that the rate of Ca^{++} re-equilibration can change by over 2 orders of magnitude depending of the degree of glial ensheathment. It is possible that by virtue of outgrowths and by swelling and shrinking the glial cell could control the rate of re-equilibration of Ca^{++} inside the glomeruli.

2.4.2 Future improvements to the model.

As more data is gathered about the physiology of granule cell dendrites and mossy fiber terminal, we will be able to add further complexity to the model. Knowing the types and amounts and the locations of Ca^{++} channels present inside the glomeruli would assist in addressing relative contributions of different cell types to the drops in the extracellular Ca^{++}. Currently available information about the state of Ca^{++} conductance inside the glomerulus is fairly sparse. What is known is that mossy fiber terminals possess Ca^{++} channels that can be blocked by Ni^{++} (Maffei, et al, 2002). Cultured granule cells contain a multitude of Ca^{++} channel varieties: L-, N-, P-, Q-, T-, R- (Forti et al, 1994; Pearson et al, 1995; Randall and Tsien, 1995, 1997; Tottene et al, 1996; Schramm et al, 1999) and L- with "anomalous gating" (Forti and Pietrobon, 1993). It is also known that granule cells contain HVA currents as measured at the soma (Rossi, et al, 1994). It is also likely, based on immunohistochemical studies of P/Q type calcium channels in the cerebellum, that they are absent from the granule cell dendrites (Kulik, et al, 2004). In addition, granule cells contain NMDAR receptors (reviewed in D'Angelo, et al, 2005, Gall, et al, 2005). Furthermore, recent findings (Rojas, et al, 2007), linked elevation of extracellular glutamate with activation of reverse Na^+/Ca^{++} exchange in cerebellar glial cells in dissociated culture. This lead to Ca^{++} influx into the glial cells, as Na^+ co-transport with glutamate led to activation of reverse Na^+/Ca^{++} exchange. This is also important as prolonged elevation in glutamate led to Ca^{++} induced Ca^{++} release from intracellular stores, leading to an increase in Ca^{++} concentration and thus making the glial cell a potential source of Ca^{++}.

Identifying the elements that are present inside the glomeruli along with determining their quantities and spatial distributions would yield several important constraints on the model. For example, identifying variability in Ca^{++} channels in the granule cell dendrites would indicate the effective resolution of the system responsible for determining extracting information from the mean $[Ca^{++}]_o$.

Appendix A. Simulation of currents in MCell.

Here we present the new type of operator in MCell that allows simulations of ion currents by calculating Monte Carlo probability for transitioning of a Ca^{++} ion through the channel pore.

Let C be the concentration of Ca^{++}. The average diffusion step length along any one of the 3 coordinate axes in 3D diffusion is given by L_d, where

$$L_d = \sqrt{4D(\Delta t / \pi)} \qquad (2.A.1)$$

where D is the diffusion coefficient of Ca^{++}, Δt is the time step, $\pi = 3.141529\ldots$. On average, one half of the number of Ca^{++} ions inside the volume $L_d * A$, where A is the area of the effector, will hit the effector in a single time step dt and as a result have the opportunity to pass through the effector's "channel pore".

Thus the average number of moles of Ca^{++} ions that will hit the channel pore in one time step is N, where

$$N = \frac{1}{2} L_d A C \qquad (2.A.2)$$

and the ion flux in a single time step through the pore J will be

$$J = \frac{p L_d A C}{2\Delta t} \qquad (2.A.3)$$

where p is the probability that if an ion hits it is carried to the other side of the membrane.

By substituting equation 2, it follows that

$$p = \frac{J\Delta t}{N} \qquad (2.A.4)$$

Macroscopically, we can relate flux to measured ionic current at a globally constant ionic concentration by

$$J_m = \frac{I}{Fz} \tag{2.A.5}$$

Where J_m is the macroscopic flux, F is the faradays constant and z is the charge on the ionic species (+2 for Ca^{++}).

Since $J_m \sim J$,

$$p = \frac{I}{2CAL_d Fz} \tag{2.A.6}$$

The only two unknowns in this equation are I and C. Currently, MCell makes the simplifying assumption that channel permeability is independent of concentration, in other words, there is a linear relationship between I and C. Therefore, knowing I for any concentration C at a constant voltage V allows one to predict current I' at any concentration C':

$$I' = \frac{IC'}{C} \tag{2.A.7}$$

Thus letting $I/C = K$, equation in (2.A.6) becomes …

$$p = \frac{K}{2AL_d Fz} \tag{2.A.8}$$

Thus p is independent of any particular concentration.

Appendix B. Parameters of the HH channels.

The basic equation governing the evolution of conductance of the channels is

$$g(t,V) = \bar{g} m^p h \tag{2.B.9}$$

where $g(t,V)$ is the conductance at time t given voltage V, $\bar{g}$ is the peak conductance, and m and h are the activation and inactivation state variables respectively with p indicating cooperativity in the activation of the channel.

Evolution of the two variables in time is described by a basic Markof 2-state process as shown below.

$$\frac{dm}{dt} = a_m(1-m) - b_m m \quad (2.B.10)$$

$$\frac{dh}{dt} = a_h(1-h) - b_h h \quad (2.B.11)$$

where a_x and b_x are the on and off rates for each state variable.

Relationship of each variable with voltage (V) is given below for each current type.

A) Parameters of HH Na current:

$p = 3$; $\bar{g} = 548$ pS/μm^2

$a_m = 7.5*\exp(0.081*(V+29))$, $b_m = 7.5*\exp(-0.066*(V+29))$

$a_h = 0.6*\exp(-0.089*(V+40))$; $b_h = 0.6*\exp(0.089*(V+40))$

with V given in mV.

B) Parameters of HH K current:

$p = 4$; $\bar{g} = 89.1$ pS/μm^2

$a_m = 0.85*\exp(0.073*(V+28))$; $b_m = 0.85*\exp(-0.018*(V+28))$

$a_h = 35*10^{-4}+3*10^{-4}*\exp(-0.08*(V+36))$, $a_h > 38*10^{-4}$

$b_h = 5.5*10^{-3}/(1+\exp(-0.0807*(V+34))$

C) Parameters of K_a current:

$p = 3$; $\bar{g} = 11.47$ pS/μm2;

$\tau_m = 0.167 + 0.41*\exp(-1/42.8*(V+33.5))$; $m^{\infty} = 1/(1+\exp(-1/19.8*(V+36.7)))$

$a_m = m^{\infty} / \tau_m$; $b_m = (1- a_m * \tau_m)/ \tau_m$;

$\tau_h = 10.8 + 0.03*(V-10) + 1/(57.9*\exp(0.127*(V-10)) +$

$0.000134*\exp(-0.059*(V-10)))$

$h^{\infty} = 1/(1+\exp(1/8.4*(V+68.8)))$

$a_h = h^{\infty} / \tau_h$; $b_h = (1- a_h * \tau_h)/ \tau_h$;

D) Parameters of H current:

$p = 1$; $h = 1$;

$\bar{g} = 0.3$ pS/μm^2

$a_m = 4*10^{-3}*\exp(-0.0909*(V+65))$; $b_m = 4*10^{-3}*\exp(0.0909*(V+65))$

E) Parameters for K-dependent Ca^{++} current

$p = 1$; $h = 1$; $\bar{g} = 180$ pS/μm^2

$a_m = 12.5/(1+1.5e\text{-}3*\exp(-0.085*(V-10))/[Ca^{++}]_i)$

$b_m = 7.5/(1+[Ca^{++}]_i/(150*10^{-6}*\exp(-0.077*(V-10))))$

where $[Ca^{++}]_i$ is intracellular Ca^{++} concentration.

Intracellular Calcium dynamics for K-dependent Ca^{++} current

$$\frac{d[Ca^{++}]_i}{dt} = \frac{I_{Ca^{++}}}{4FAr} - \frac{[Ca^{++}]_i - [Ca^{++}]_{rest}}{\tau}$$

$[Ca^{++}]_{rest} = 75.5$ nM; $\tau = 10$ ms, $A = 314$ μm^2; r = 0.042 μm; F = 96480 C/mol; $I_{Ca^{++}}$ is the inward Ca^{++} current.

F) Parameters of inward Ca^{++} current:

p = 2; $\bar{g} = 9.2$ pS/μm^2

$a_m = 8.0/(1+\exp(-0.072*(V-15)))$; $b_m = 0.1*(V-1.1)/(\exp(0.2*(V-1.1))-1)$

$a_h = 0.025*\exp(-0.05*(V+50))$; $b_h = -0.025*\exp(-0.05*(V+50))+0.025$

$a_h > 0.025$; $b_h > 0$

3. Simulating glutamate spillover in cerebellar glomeruli.

3.1 Introduction.

The granular layer of the cerebellum may be responsible for reducing redundancies in the representation of the multidimensional sensory and motor information that enters the cerebellum (Eagleman, et al, 2001). This can effectively solve the credit assignment problem allowing Purkinje cells to associate every granule cell input pattern with a unique mossy fiber pattern and to learn new relationships between mossy fiber input and climbing fiber signal more rapidly. Key to this hypothesis is the function of cerebellar glomeruli – complex synaptic structures tightly ensheathed by glial cells where signals carried by mossy fibers are transmitted to granule cell dendrites. According to the hypothesis, glial ensheathment limits the rate of Ca^{++} diffusion between inside and outside the glomerulus, thereby allowing extracellular [Ca^{++}] to act as a global signal that communicates the mean rate of dendritic activity within the glomerulus to each of the dendrites. This information could be used by mossy fiber to granule cell to adjust the efficacy of the synaptic connection between itself and the mossy fiber based on the activity of all the granule cells. The following learning rule that can sparcify granule cell activity and reduce redundancies in the signal carried by mossy fibers is a possible way to take advantage of the global activity information,

$$\Delta w_i = w_i - a\sum_j w_j s_j \tag{3.1}$$

where w_n is the efficacy of the nth mossy fiber to granule cell synapse, a is a proportionality constant and s is the activity of the post-synaptic cells (Eagleman, et, al, 2001).

In chapter 2 we investigated that investigated the physiological feasibility of the above hypothesis. The results demonstrated that while [Ca^{++}] fluctuations can be proportional to the rate of overall activity in the glomerulus, the extent of fluctuations is highly sensitive to the tightness of the glial ensheathment.

This chapter will deal with possible ways in which this limitation can be overcome. Specifically we will investigate the possibility of localizing Ca^{++} signal in time and in space as a way of "outrunning" relatively slower Ca^{++} refilling from the

outside of the glomerulus. We hypothesize that this localization can happen by virtue of inducing Ca^{++} currents at the spillover-activated NMDARs at dendro-dendritic adhesion junctions. Consequently, we will test efficacy of spillover at activation NMDARs and we will examine how well drops of $[Ca^{++}]$ can be localized at the adhesion junctions.

3.1.1 Spillover mediated activation of extrasynaptic NMDARs.

Cerebellar glomeruli are roughly spherical (5-10 μm diameter) structures that contain a single mossy fiber axon terminal surrounded by a swarm of 20-50 claw-like granule cell dendrites and one or more inhibitory Golgi cell axons. Glomeruli are ensheathed by a glial sheath (Palay and Chan-Palay, 1974; Landis, et al, 1986; Jakab and Hamori, 1988; Jakab, 1989). The dendritic digits of granule cells within the glomerulus form numerous dednro-dendritic adhesion junctions some distance away from the mossy fiber terminals (Palay and Chan-Palay, 1974, Rose, et al, 1995, Bahjaoui-Bouhaddhi, et al, 1997).

One mossy fiber terminal (MFt) can make 200-400 glutamatergic synaptic contacts with GrC dendrites (Jakab and Hamori, 1988; Xu-Friedman and Regehr, 2003). Two studies have demonstrated that significant quantities of glutamate released by the MFt spills out of the synaptic clefts into surrounding extracellular space. (Mitchell and Silver, 2000; DiGregorio, et al, 2002). This spillover glutamate can reach the dendro-dendritic adhesion junctions (AJs) that contain functional N-methyl-D-aspartate receptors (NMDAR) (Petralia et al, 2002). Because glomeruli are enclosed in a glial sheath, it is possible that NMDARs on the adhesion junctions that are near to the glial cells receive consistently lower amounts of glutamate. Ca^{++} currents through the NMDARs on the adhesion junctions may lead to physiological changes that affect the efficacy of the mossy fiber-granule cell synapse. Furthermore, it is possible that the current through one of the sides of the AJ leads to physiological changes on the other side by virtue of a retrograde signal.

A goal of this chapter is to examine how well glutamate can activate NMDARs at different distances to the glial sheath. Since discrimination between spillover-mediated activation of NMDARs on separate AJs in one glomerulus is

difficult to study experimentally given currently available technology, but is crucial to validation of the hypothesis, these investigations were done in a model of the cerebellar glomerulus based on published morphological data. Our results showed that such activation may be possible to achieve in the high frequency regime of mossy fiber activity.

3.1.2 Localized Ca^{++} fluctuations at the AJs.

One possibility for the retrograde signal mentioned in the previous section could be depletion of extracellular Ca^{++} inside the cleft of the AJ. In the second part of this chapter we examine localized Ca^{++} fluctuations caused by currents through NMDAR channel pores. Currently no experiments are available to directly measure calcium depletion at individual AJs inside a whole glomerulus, since the small volumes of the clefts ($1x10^{-4}$ μm^3) are below the optical resolution of laser scanning microscopy (Rusakov and Fine, 2003). For that reason extracellular Ca^{++} depletion events at the AJ were modeled in a biologically realistic morphology of the AJ cleft based on previously determined structural parameters (Palay and Chan-Palay, 1974). We varied several parameters that would be expected to influence calcium depletion in the AJ cleft to determine how those parameters influence the degree to which a single Ca^{++} depletion event can be resolved in time and space. Our results show that the depletion events are resolvable by at least ~100 nm in space and by at least ~ 1 ms in time.

3.1.3 Leakage of glutamate between neighboring glomeruli.

Simulation studies of glutamate spillover allowed us to address the question of how well glutamate may leak between glomeruli. Electron microscopic studies of the granule layer revealed that glomeruli are found in clusters; and that within such a cluster two glomeruli may be separated by no more than a thin sheath of a single glial cell (Palay and Chan-Palay, 1974). Such juxtaposition of glomeruli can bring the surfaces of the mossy fiber terminals within 5 μm of each other and more importantly, it can bring NMDAR-containing AJs less than 3 μm from dozens of release sites that belong to the neighboring glomerulus. It is generally believed that velate astrocytes

that ensheathe individual glomeruli act to limit leakage of glutamate out of one glomerulus and into another one. However, it has not yet been established how well glial cells are capable of limiting this leak, especially given all the findings that mossy fibers possess several hundred available release sites, can release at frequencies well above 100 Hz (Garwicz, et al., 1998), are able to maintain high release probabilities 30%-70% during long (> 5 action potentials) firing trains (Sargent, et al., 2005; Saviane and Silver, 2006), and that presence of AJ in the glomeruli of adult animals potentially moves NMDARs closer to the sites of glutamate leakage. (Cathala, et al, 2000; Petralia, et al, 2002). Given the above arguments, we performed a series of simulations of glutamate leaks in models of glomeruli with stylized glomerular and glial morphologies. These simulations revealed that under certain conditions of glial ensheathment leakage of glutamate from one glomerulus could prime NMDARs in a neighboring glomerulus.

3.2 Methods.

All of the simulations in this chapter were done with MCell. As mentioned in the previous chapter, MCell is a Monte Carlo simulator of cellular biophysics (Bartol, et al, 1991; Stiles et al, 2001; Stiles and Bartol, 2001). MCell uses rigorously validated and highly optimized Monte Carlo algorithms to simulate the random-walk Brownian motion of discrete diffusing molecules and concomitant uni- and bi-molecular chemical reactions in a complex three-dimensional environment reflecting realistic cellular microstructure. MCell has been used to model vesicular release (Stiles et al., 2001), diffusion in the synaptic cleft (Franks et al., 2002), and investigate the impact of neuronal shape on tortuosity (Tao and Nicholson, 2004).

3.2.1 Model setup for glutamate spillover within one glomerulus:

The morphological model was the same as the one used in the original Ca^{++} fluctuation simulations described in chapter 2. The geometric parameters use to constrain the model were glomerular volume and surface area, the volume and surface area of the mossy fiber terminal, the fraction of glomerular volume occupied by the dendrites, and the extracellular volume fraction. The last parameter was

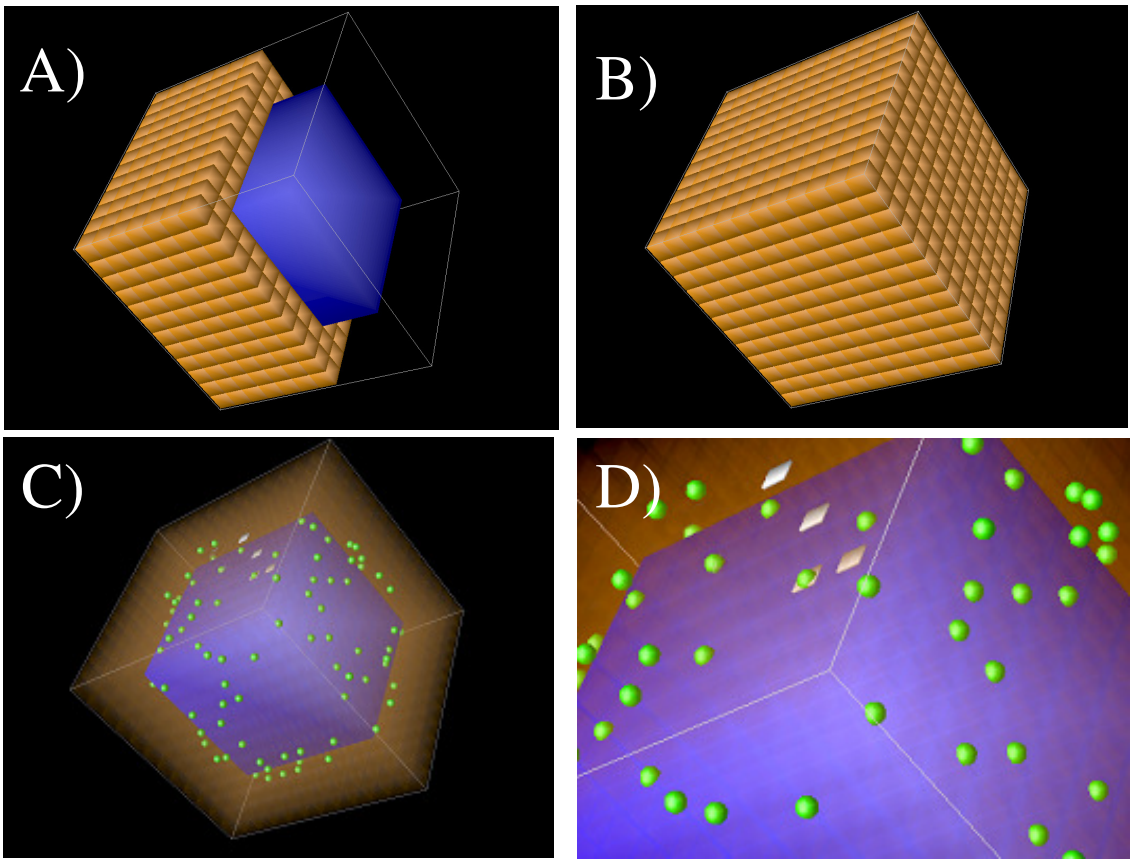

Figure 3.1 Model setup for glutamate spillover in the cerebellar glomeruli.
Orange boxes represent the axo-dendritic milieu and the blue box in the center represent the mossy fiber terminal. The length of the side of the orange boxes is 0.4 µm. The length of the side of the blue box is 3.34 µm. Gray line segements that intersect in the middle of the image and that can be seen to othe left of the 4 measurement boxes are the edges of the glial box.

A) Image of the model geometry with some of the axo-dendritic millieu boxes removed to show the central mossy fiber axon terminal.
B) Outside view of the model geometry without the glial sheath.
C) Axo-dendritic millieu has been rendered transparent to show the sites of the glutamate release (green spheres) and sites of glutamate measurement (4 gray boxes). Gray line segments in the periphery of the model correspond to the edges of the glial box.
D) A zoomed in view of the model glomerulus shows the 4 glutamate measurement sites.

maintained at 11%. The other parameters were based on serial electron microscopic investigations of rat glomeruli described in Jakab and Hamori, 1988 and Jakab, 1989. Figure 3.1 (A) shows the structural arrangement of the model – a grid of small boxes surrounding a large box in the middle, with the large middle box corresponding to the mossy fiber terminal core and the grid of smaller boxes corresponding to the axo-dendritic milieu. Instead of representing GrC dendrites as contiguous structures we opted for a simpler and more abstract representation of the neuropil (c.f. Franks et al, 2002). The dimensions of the large
central cube are 3.34 μm along each coordinate axis; of the smaller cubes: 0.4 μm along each coordinate axis; of the glial sheath: 5.06 μm along each coordinate axis. The space between all surfaces was 20 nm wide. These parameters were based on measurements done in 3D EM studies of glomeruli by Jakab and Hamori, 1988 and Jakab, 1989. The entire structure was surrounded by a large box - which represents the glial sheath - that prevents glutamate diffusion past 20 nm beyond the boundaries of the most peripheral of boxes. Glutamate was released from 150 sites (Xu-Friedman and Regehr, 2003) some of which are shown in figure 3.1 (C). Either 3000, 4000, or 5000 glutamate molecules were released from each site in a simulation (Franks, et al, 2003; Nielsen, et al, 2004). Glutamate diffusion coefficient was varied based on estimates of glutamate diffusion coefficient in glomeruli by (Nielsen, et al, 2004). Figure 3.1 (D) shows a close-up of the boxes used to count glutamate in the simulations. They were strategically placed at different distances between the mossy fiber and the glial sheath. Glial sheath was covered with glutamate transporters (GluT), whose kinetic scheme is given in figure 3.2, and whose density was set to $5000/\mu m^2$ (Furuta, et al, 1997; Lehre and Danboldt, 1998). Glutamate was released 5 times at 100 Hz (Garwicz, et al, 1998; Sargent, et al, 2005). Each simulation generated a series of glutamate concentration profiles in each of the boxes which were plugged into a numerical simulation of NMDAR receptor activation based on Lester and Jahr, 1992 whose kinetic scheme is shown in figure 3.3. A sample 3D view of glutamate release and spread in the model at 8 points in time is given in figure 3.4.

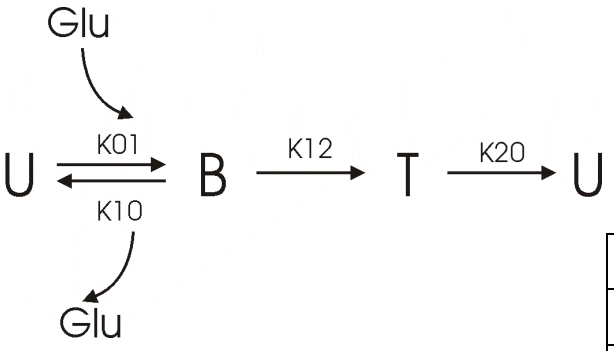

K01	K10	K12	K20
$M^{-1}s^{-1}$	s^{-1}	s^{-1}	s^{-1}
$1.8*10^7$	180	180	25.7

Figure 3.2 Glutamate transporter kinetic scheme used in preliminary simulations. Rate constants for the kinetic scheme based on Geiger et al 1999.

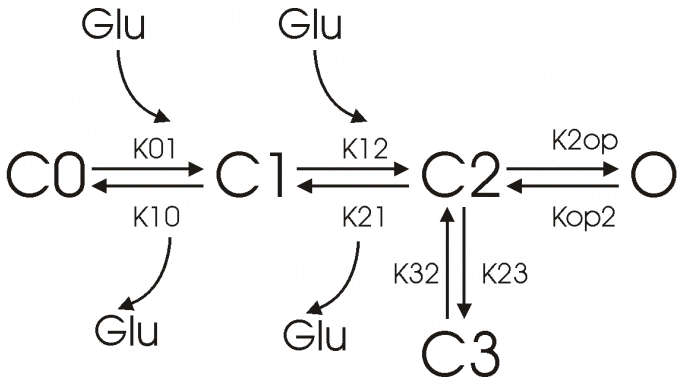

K01	K10	K12	K21	K2op	Kop2	K32	K23	K10
$M^{-1}s^{-1}$	s^{-1}	$M^{-1}s^{-1}$	s^{-1}	s^{-1}	s^{-1}	s^{-1}	s^{-1}	s^{-1}
$1*10^7$	4.7	$5*10^6$	25.7	46.5	91.6	1.8	8.4	4.7

Figure 3.3 Cerebellar NMDAR kinetic scheme**.** Rate constants for the kinetic scheme, based on Lester and Jahr, 1992.

3.2.3 Model setup for localized Ca^{++} depletion.

Localized Ca^{++} depletion model was based on the same geometry as the one used in the original Ca^{++} fluctuation simulations as shown in Figures 3.5 A and 3.5 B. Since the aim was to model activity at and around an individual AJ, a significantly smaller volume was necessary in the model. We extracted from the original model a 5x5x2 set of dendritic milieu cubes (Figure 3.5 B). The interface between the top surfaces of the bottom boxes and bottom surfaces of the top boxes represented the adhesion junction (AJ). Ca^{++} was measured in the gaps between the upper layer and the lower layer of boxes – figure 3.5 C. Surfaces permeable to Ca^{++} currents were limited to a 200 nm x 200 nm areas in the center of each square so as to match the size of the adhesion junctions (Figure 3.5 D). Currents were modeled as a 0.5 ms step increase in the Ca^{++} permeability of the patch from 0 pA to 1.5 pA. This is equivalent to opening of 5 channels with 4 pS conductance (Franks, et al, 2002) with the mean driving force of 100 mV.

3.2.4 Model setup for glutamate leakage between glomeruli.

The morphological model for glutamate leakage was based on the original model. For these specific simulations however, we removed the right wall of the original glial sheath, duplicated the large central box (mossy fiber terminal core) and the surrounding grid of boxes (axo-dendritic milieu) and shifted the copies to the right by 5.48 μm which equals to the length of the whole model plus 0.42 μm. This created a 0.44 μm gap between the two glomeruli. Finally, we extended the glial sheath into such that it encloses the entire volume. The 0.44 μm gap between the two glomeruli was filled in one of 3 following ways. 1) The two glomeruli are be separated by a 0.4 μm thick wall that closes off all the paths between the two glomeruli except for the 20 nm gap around its periphery. All of the surfaces of this wall represent glial sheath and thus contain GluT. This ensheathment called here "nearly complete" is shown in figure 3.6 (A). 2) The two glomeruli are separated by a grid of 12x12 boxes, which represent numerous leaks in the glial sheath. All of the surfaces of the boxes contain GluT. This ensheathment will be referred to as "partially complete." 3) The arrangement of the boxes remains the same as in 2), but in this case, they carry no GluT. This condition will be referred to as "no

ensheathment;" however this only refers to the interface between the two model glomeruli as the remaining sides of the glial sheath under all conditions were covered by the GluT. Figure 3.6 (C) shows the unnecessary simulation parameter – a wall that completely closes off the two glomeruli. Those simulations did not require the new model. Figure 3.5 (D) shows the image of the model. Again, blue boxes represent the mossy fiber core, orange boxes are the axo-dendritic milieu; green spheres are glutamate release sites. Presence of many gray boxes in the middle indicates that the model was either in state 2 or 3. Four red rectangles show the positions of the 4 glutamate measurement sites.

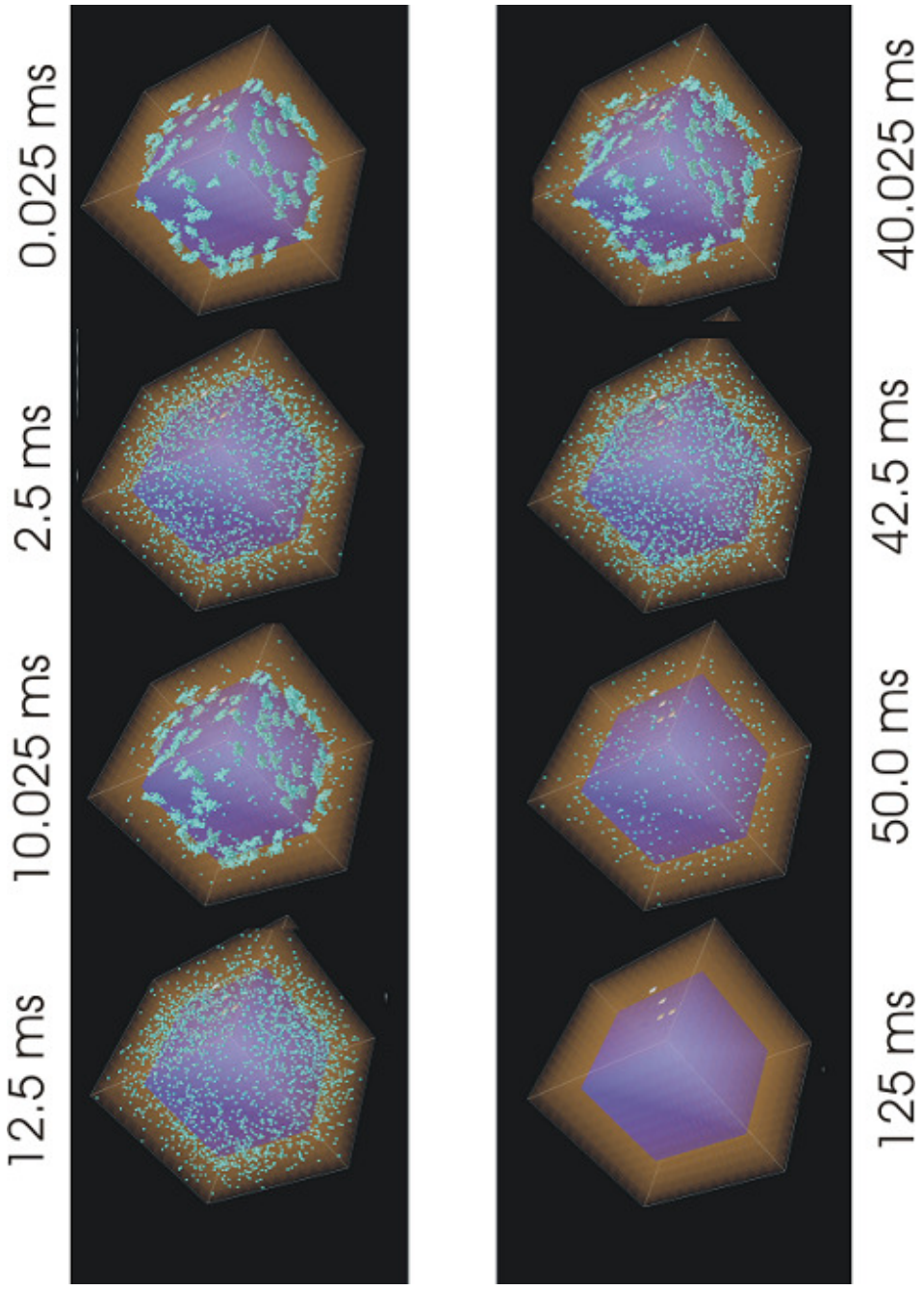

Figure 3.4. Sample time course of glutamate concentration in a single simulation. Blue spheres represent the glutamate molecules.

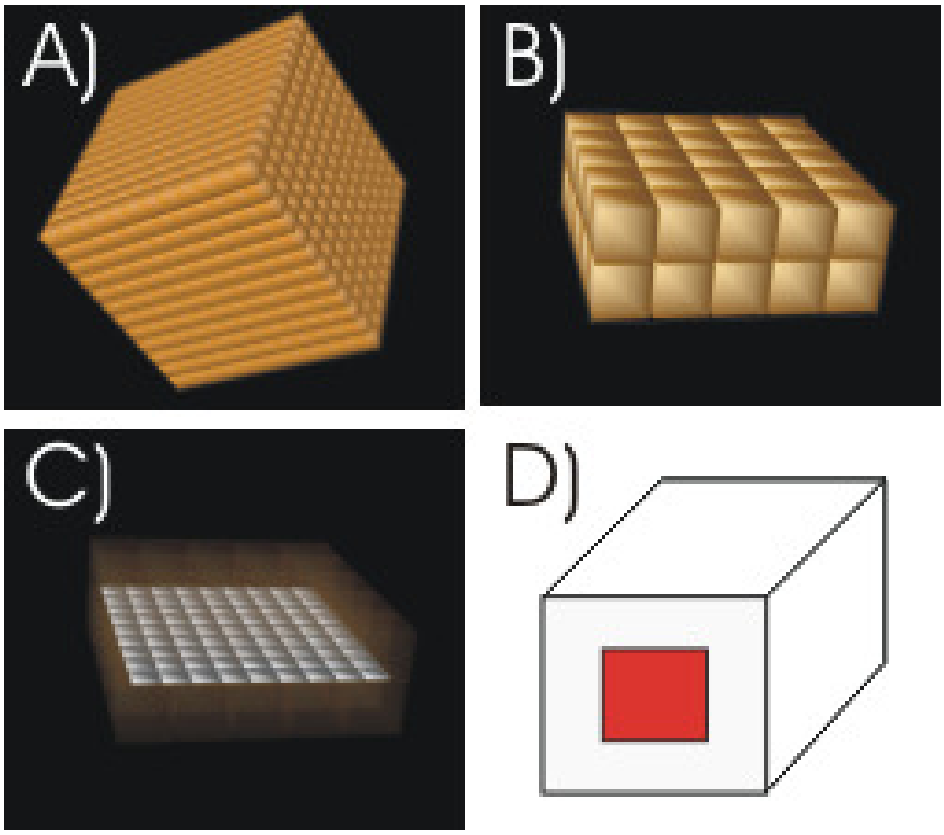

Figure 3.5. Localized Ca^{++} fluctuations model setup.
A) Original geometry – a cube-shaped grid of small cubes. The whole structure is ~5.02 μm on the side.
B) 5 cube x 5 cube x 2 cube region used in the simulations.
C) The orange cubes that represent pieces of the axo-dendritic milieu of the glomeruli are rendered transparent. In the gap between the two layers we placed Ca^{++} measureing boxes shown in gray. The number of Ca^{++} ions inside the volume circumscribed by those cubes was recorded for every time step.
D) Location and shape of the Ca^{++} consuming surface on a dendritic cubes. The dimensions of each face of the dendritic cubes were 400 nm x 400 nm. The dimensions of each Ca^{++} consuming surface was 200 nm x 200 nm.

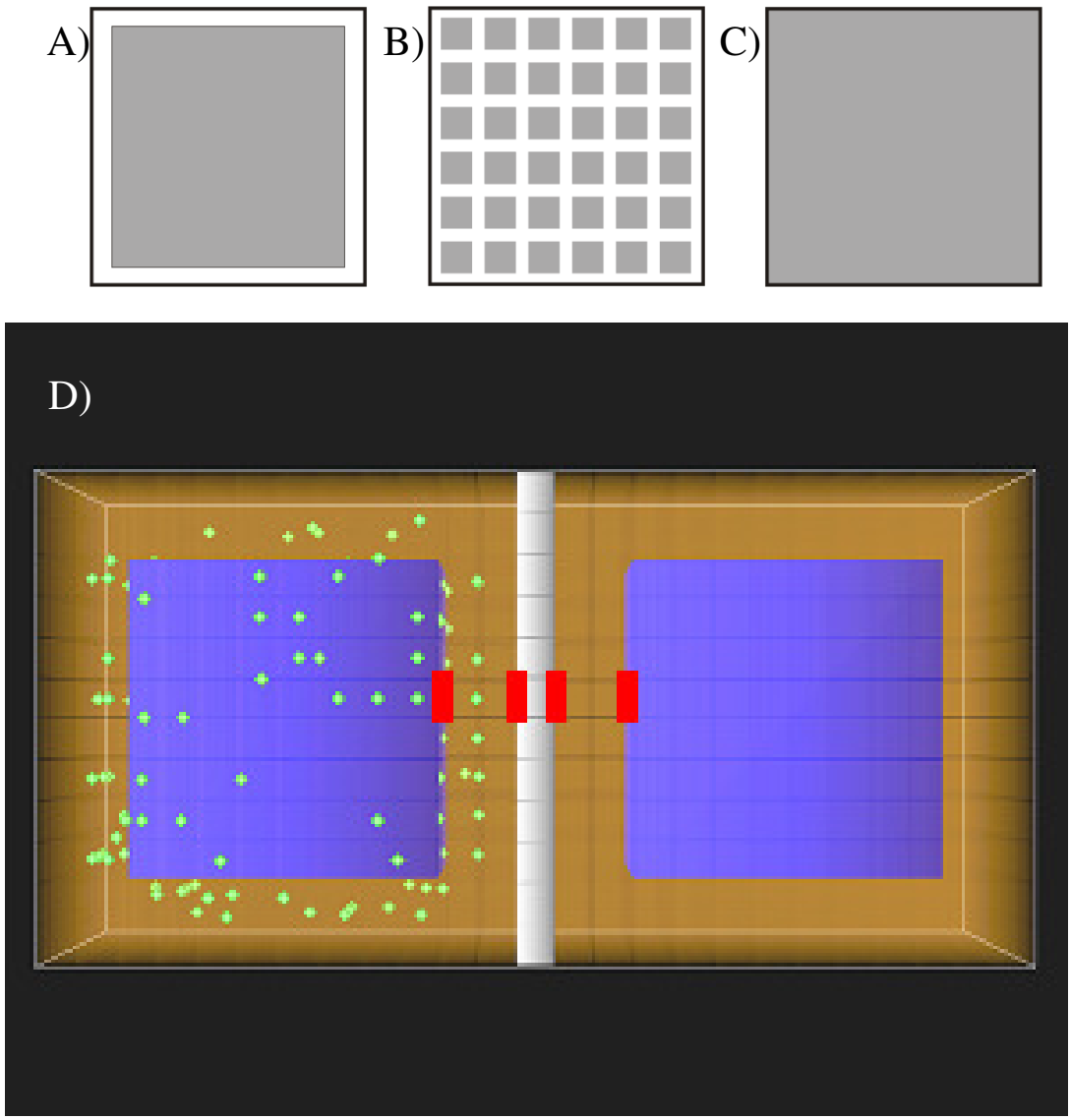

Figure 3.6. Model setup for glutamate leaks between 2 glomeruli.
A) One of the arrangements of the interface between the two glomeruli – "nearly complete ensheathment" where the two glomeruli are separated by a wall with a 20 nm gap at the periphery. (The gap is not drawn to scale).
B) The other arrangement for the interface between the two glomeruli used for simulations with "partial ensheathment" or "no ensheathment" where the two glomeruli are separated by a grid of boxes.
C) An unnecessary setup – "complete ensheathment" - equivalent to modeling a single glomerulus.
D) Image of the entire model.

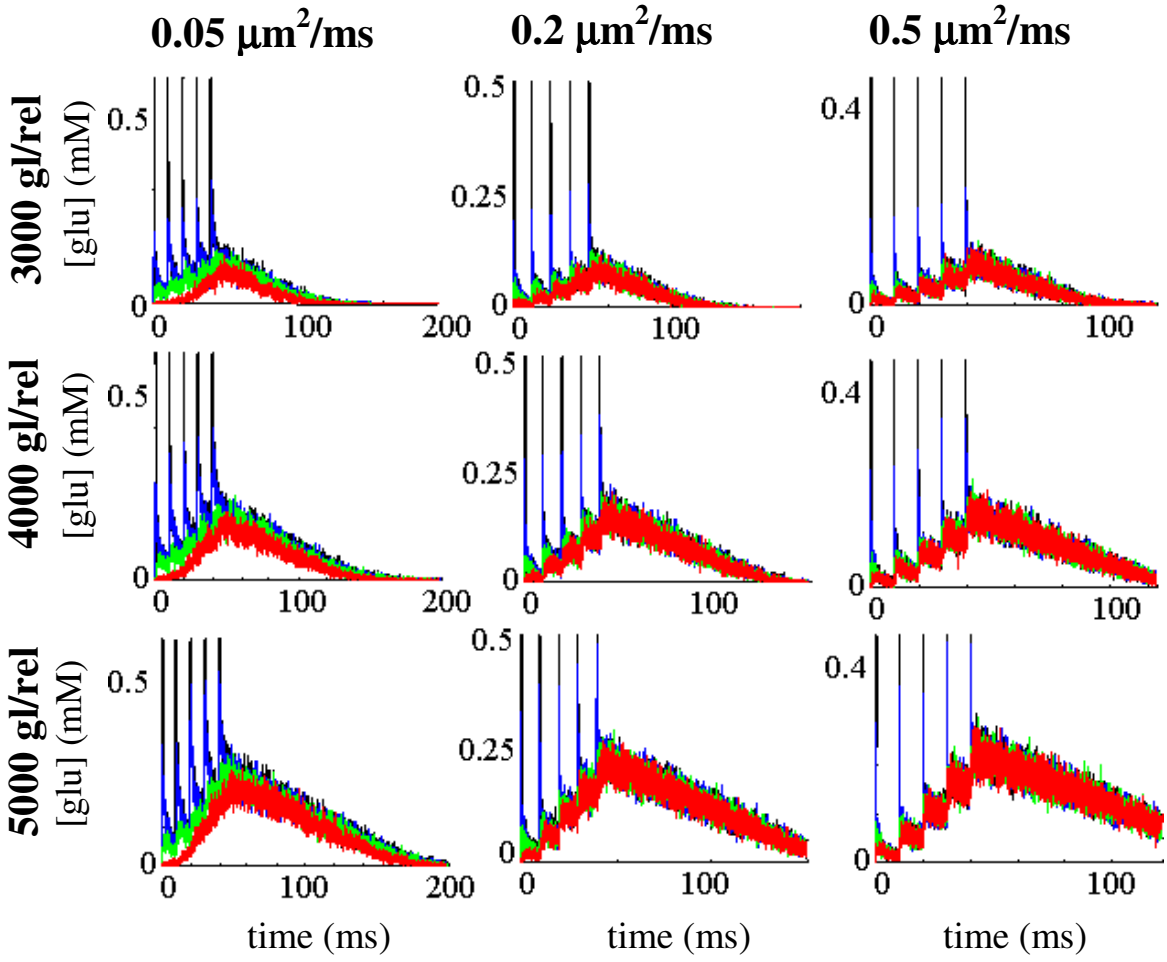

Figure 3.7. Time courses of glutamate concentration as it spills over in the model glomerulus.

The four colors correspond to the four sites of glutamate measurement Black curve corresponds to the site which is located next to the mossy fiber terminal and a release event occurs inside it. Blue curve corresponds to the site next to mossy fiber terminal. Green curve corresponds to the site that is located in the space between the upper and lower layers of axo-dendritic milieu boxes and the red site is located between the outer layer of the axo-dendritic milieu and the glial sheath.
Each column corresponds to a different glutamate diffusion coefficient as shown in bold above each column. Each row corresponds to a different amount of glutamate released per release event as shown to the left of each row.

3.3 Results

3.3.1 Glutamate spillover within a single glomerulus.

Our aim was to determine whether spillover glutamate could effectively activate extrasynaptic NMDARs regardless of their position in a glomerulus. Therefore the following simulations were made in an attempt to recreate glutamate release from a mossy fiber that is active at high firing rates. In fact mossy fibers have been shown to fire at > 100 Hz (Garwicz, et al, 1998). We used 100 Hz release rate with 5 release events consistent with physiological evidence.

Four sites chosen to in such a way as to sample sites inside the glomerulus located at different positions relative to the glutamate release sites and the glia were chosen. The first site and the second site lay in the gap between the mossy fiber terminal and the first layer of axo-dendritic milieu. The difference between the two is that the first site was located at a release site and therefore glutamate time course there was used as a reference time course. The second site did not experience direct release of glutamate. The third site was positioned in the gap between the two layers of the axo-dendritic milieu. The fourth site was placed in the gap between the glia and the second layer of the axo-dendritic milieu. Figure 3.1 (D) shows a close-up of the model glomerulus with the 4 sites.

Figure 3.7 shows time courses of glutamate as a function of the number of glutamate released and of glutamate diffusion coefficient. As expected, the greater amount of glutamate per release led to higher concentrations of glutamate at all sites under all conditions. Under all conditions, glutamate concentration has a “triangular” profile, as glutamate transporters were unable to catch up with the increasing amounts of glutamate in the glomerulus. At the sites near the mossy fiber, the rising phase of the “triangle” is punctuated by spikes in concentration that occur at the times of release. In figure 3.8 we show the average glutamate concentration at all sites for 200 ms after the first release event. What is clear from this image is that even though glutamate may experience high peak concentrations, sites unable to receive direct glutamate release still enjoy comparable quantities of glutamate over time. Of course, since NMDAR

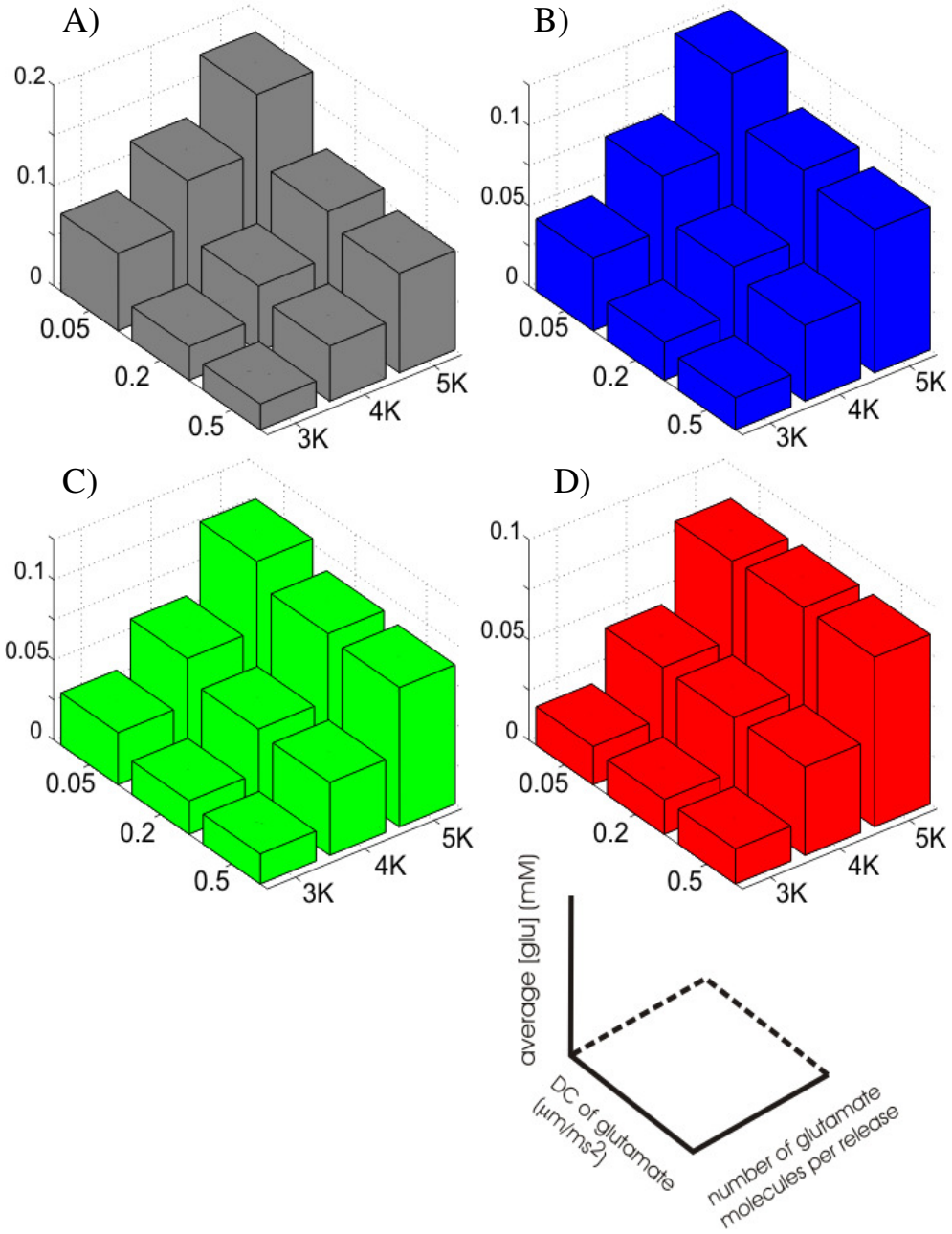

Figure 3.8. Average [glu] present at different sites under all simulated conditions.

A) Average [glu] at reference site.
B) Average [glu] at site near mossy fiber terminal.
C) Average [glu] at the site between the layer of axo-dendritic milieu.
D) Average [glu] at the site near the glial sheath.

kinetics are not a linear function of glutamate concentration, we then determined the activation of the NMDARs by the spillover glutamate at the different locations.

Time courses of NMDAR activation are shown in figure 3.9. It has nearly identical format to figure 3.7, but now the time courses of glutamate concentration were replaced with time courses of NMDAR in the doubly bound open state. Under all conditions all of the NMDARs were able to reach near peak (within 3% of activation of the site that received direct release). Depending on the position however, the courses of NMDAR activation peaked at different times. Figure 3.10 shows the times to peak of NMDAR doubly bound open state at some of the simulated conditions. Figure 3.10 (A) shows times to peak for all conditions where the number of glutamate released per release event was 4000. Peak NMDAR activation appears to converge as the diffusion coefficient of glutamate increases. This is not surprising as the sites closer to the release sites benefit from the prolonged dwell, caused by slower glutamate diffusion, which leads to a higher probability of binding to the receptor. On the other hand, the more distant sites benefit from faster diffusion coefficient, as glutamate is able to get to them sooner. Figure 3.10 (B) shows the times to peak NMDAR doubly bound open state for all conditions where the diffusion coefficient was held at 0.2 $\mu m/ms^2$. There, the trend for all sites is consistent, as increasing the number of glutamate molecules caused an earlier time to peak.

The original aim of these simulations was to show that NMDARs could be activated by spillover glutamate regardless of their location. The results painted a more complicated picture where the timing of NMDAR activation is sensitive to number of molecules released and to the diffusion coefficient.

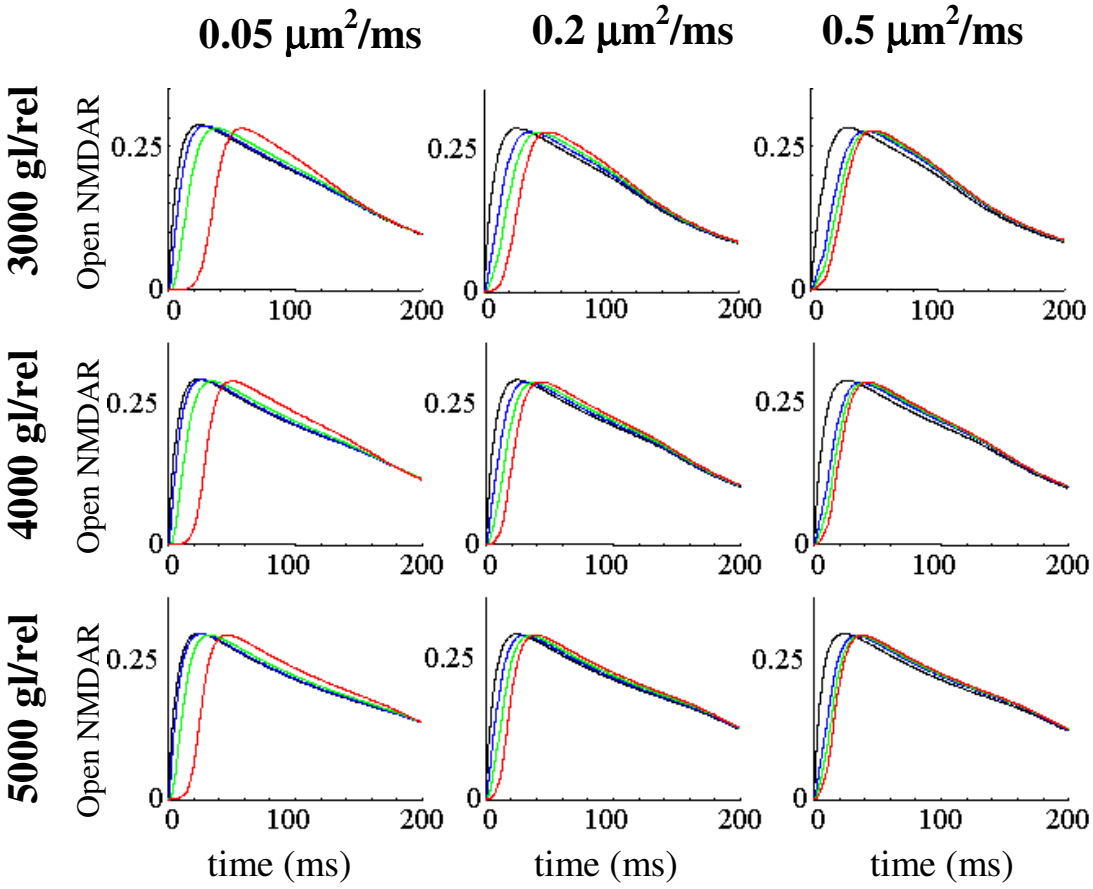

Figure 3.9. Time courses of NMDAR activation.

The four colors correspond to the four sites of glutamate measurement. Black curve corresponds to the site which is located next to the mossy fiber terminal and a release event occurs inside it. Blue curve corresponds to the site next to mossy fiber terminal. Green site is located in the space between the upper and lower layers of axo-dendritic milieu boxes and the red site is located between the outer layer of the axo-dendritic milieu and the glial sheath.
Each column corresponds to a different glutamate diffusion coefficient as shown in bold above each column. Each row corresponds to a different amount of glutamate released per release event as shown to the left of each row. Glutamate concentration was converted into NMDAR open state fraction.

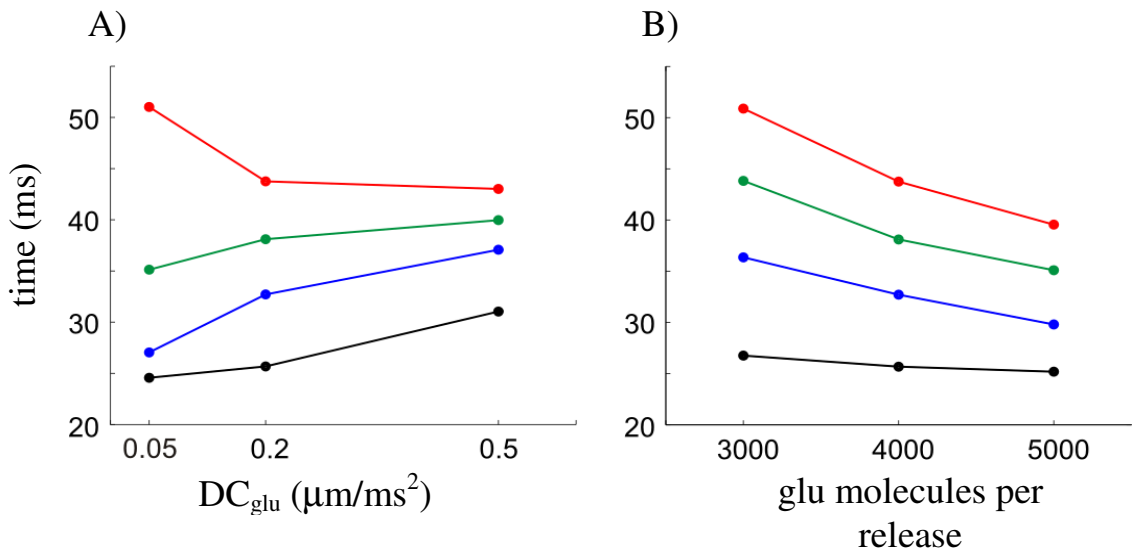

Figure 3.10. Convergence of times to peak of NMDAR open state.

A) Times to peak for all the simulations where 4000 molecules of glutamate were released per release event.
Sites close to the mossy fiber terminal suffer from increase in diffusion coefficient as glutamate does not linger long enough to bind as many receptors. As one goes away from the mossy fiber terminal, however, the picture reverses, where the faster diffusion coefficient actually benefits the more distant sites as glutamate can reach those sites sooner.
B) Times to peak of all the simulations where the diffusion coefficient of glutamate was set at 0.2 µm/ms^2.
Sites close to the mossy fiber do not benefit from the increase in the number of molecules released as much as the sites farther away.
Filled circles indicate actual data. Red curve corresponds to the site nearest to the glial sheath. Green curve corresponds to the site in between the two layers of axo-dendritic milieu. Blue curve corresponds to the site near the mossy fiber terminal. Black curve is the reference curve that receives direct glutamate release.

3.3.2 Localized Ca^{++} depletion at adhesion junctions.

Now that we have established that spillover glutamate can effectively reach AJs and successfully activate NMDAR receptors there, we will investigate the profile of Ca^{++} depletion in both time and space produced by a pulse of Ca^{++} current at the AJ.

Figure 3.11 shows the results of simulating localized Ca^{++} depletion at and around a single adhesion junction. $[Ca^{++}]$ measured in some of the boxes are shown. Figure 3.11 (A) shows that a single depletion event is separable in space as the box that is located directly underneath the Ca^{++} permeable patch experiences a significantly greater drop in concentration of Ca^{++} than any of the patches next to it. Figure 3.11 (B) examines separability of several simultaneous depletion events in a "worst case scenario" where a single patch is surrounded by 4 depletion events. Again, the events are separable as the depletion in the patch directly underneath Ca^{++} permeable patch is significantly greater than the depletion in the middle. Lastly, in figure 3.11 (C) we examined separability of Ca^{++} depletion events in space. To do this, we simulated 5 Ca^{++} influx events separated by 1 ms. The results show that separate events are separable within 1 ms. Since the fastest granule cells have been shown to fire action potentials is ~ 80 Hz (Chadderton, et al, 2004), 1 ms resolution is better than the 12 ms resolution needed to resolve events occurring at 80Hz.

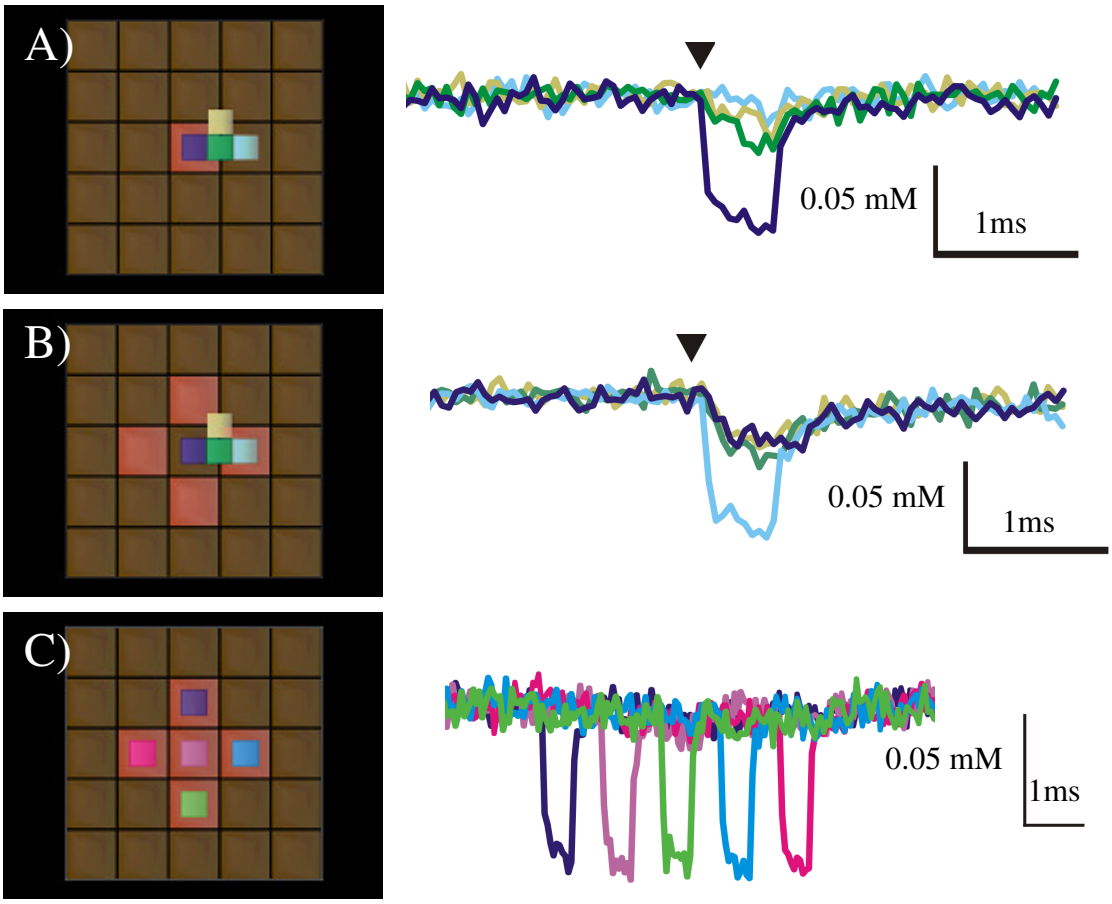

Figure 3.11. Localized Ca^{++} fluctuations at adhesion junctions
In all images, red square corresponds to the dendritic box that experienced a Ca^{++} consumpton event. Smaller colored or gray boxes show the locations of the sites where [Ca^{++}] was measured. In A and B colors of the chart correspond to the colors on the image to the left of the chart.
A) Dark purple curve corresponds to the site directly underneath the Ca^{++} consumption event. Only one event occurs and the drop observed in the volume immediately below is significantly greater than anywhere else around it. N = 12, SE < 0.008 mM
B) 4 simultaneous identical events occur around the dark purple site. [Ca^{++}] drop at that site is significantly smaller then than in the case of the event occurring in the immediate proximity as shown in A). Furthermore, the blue square that directly receives one of the events experiences the greatest drop. N = 12, SE < 0.008 mM
C) Where A) and B) show that the localized depletion events are well separated in space. Here we show that depletion events are also well separated in time, as a sequence of 5 events staggered by 1 ms fail to affect each other. N = 12, SE < 0.008 mM.

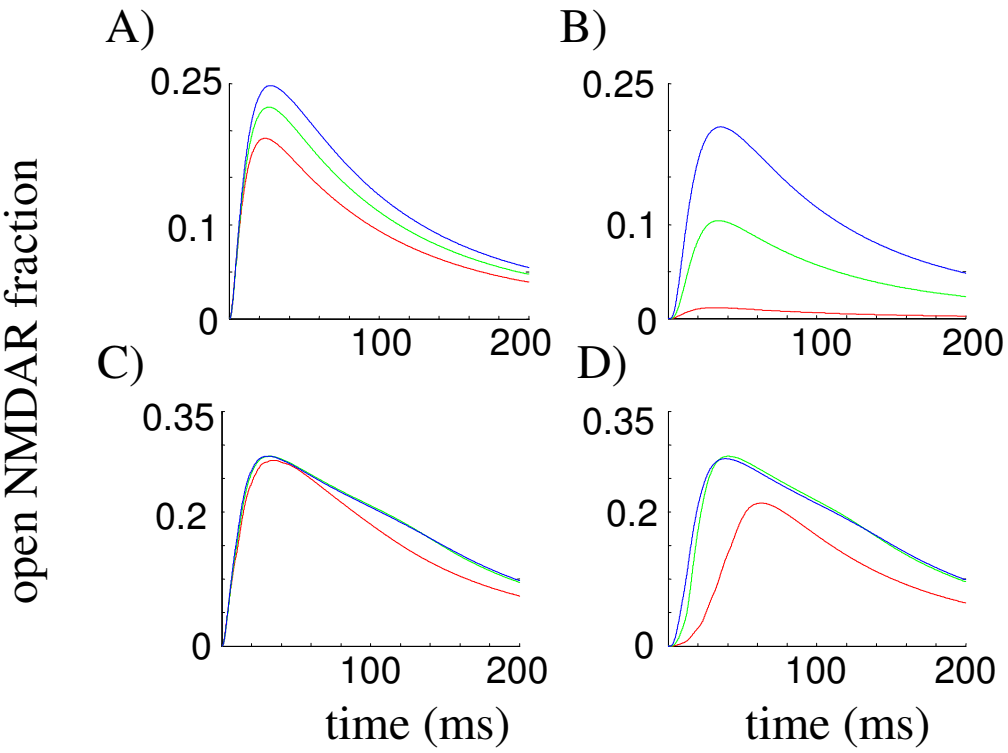

Figure 3.12. NMDAR activation in the presence of leaks in one side of a glomerulus.

Blue curve corresponds to the NMDAR activation in the condition with "no ensheathment" (figure 3.6 B with no GluT). Red curve corresponds to NMDAR activation with "partial ensheathment" (figure 3.6 B with GluT). Green curves correspond to "nearly complete ensheathment" (figure 3.6 A with GluT).

A) Activation of NMDARs in the space near the mossy fiber after 1 release event.
B) Activation of NMDARs in the space near the glial sheath after 1 release event.
C) Activation of NMDARs in the space near mossy fiber during 5 release events at 100Hz.

3.3.2 Leakage of glutamate between neighboring glomeruli.

Allowing glutamate to leak between two glomeruli permitted us to examine the effect of changes in the glial ensheathment on the time course of NMDAR activation inside the active glomerulus. In figure 3.12 we compare NMDAR activation at either a site near the mossy fiber terminal or a site near the glial sheath, after either a single release of glutamate or after 5 release events with 100 Hz release rate. In this case 4000 glutamate molecules were released per release site and per release event and the glutamate diffusion coefficient was set at 0.5 μm^2/ms. The results show that during single events the nature of glial ensheathment has a far more significant effect at the degree to which glutamate is able to spill over to sites near the glial sheath.

Finally we looked at how activity in one glomerulus would influence activation of NMDARs at adhesion junctions of another glomerulus. Five release events at 100 Hz were generated in one of the glomeruli. Glutamate diffusion coefficient was set to 0.5 μm^2/ms and GluT density was set to 5000/ μm^2. The results shown in figure 3.13 demonstrated that under "nearly complete" ensheathment glutamate leakage into the neighbor glomerulus was significantly reduced and effectively no NMDARs were opened. However, about 11 % of the receptors near the mossy fiber terminal and ~ 4% of the receptors near the glial sheath were able to bind a single glutamate molecule, which transitioned the receptors into a singly bound state that persisted well past the lifetime of glutamate. Under the condition of "partial ensheathment" glutamate leakage was sufficient to activate ~ 5% of NMDARs in the neighbor glomerulus. In addition nearly 50% of all receptors became singly bound and thus potentially "primed" for a release event in their own glomerulus. With "no ensheathment" we observed maximal activation of NMDARs in the neighbor glomerulus.

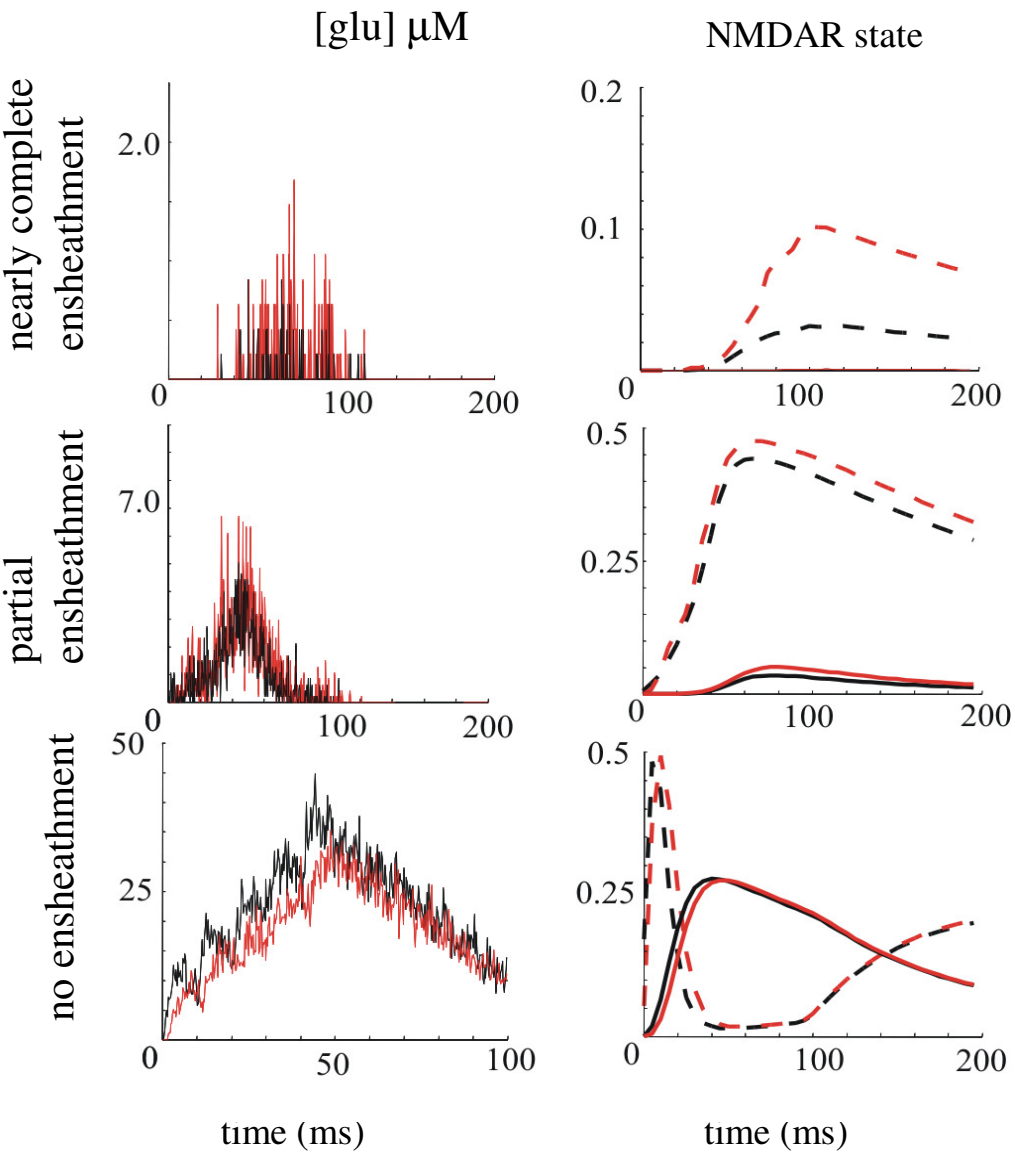

Figure 3.13. Effects of activity in one glomerulus on a neighbor glomerulus.
Red curves correspond to the site near the mossy fiber terminal in the neighbor glomerulus. Black curves correspond to the site near the glial sheath. In the NMDAR activation column dotted curves correspond to time course of NMDAR in singly bound state (figure 3.3 – state C1), while solid curves correspond to NMDAR in open state (figure 3.3 – open state).

3.4 Summary.

In this chapter we examined spillover of glutamate inside a model cerebellar glomerulus, whose geometry was based on quantitative EM studies. Our results suggest that mossy fiber under standard physiological conditions can fill entire glomerulus with enough glutamate to nearly maximally activate NMDARs located anywhere inside a glomerulus.

We speculated that since those NMDAR were found at sites of apposition between two granule cell dendrites, activation of those receptors may lead to a physiological change in the granule cell dendrite glomerulus with potential implications for mossy fiber to granule cell signaling. We further speculated that this reorganization may in and of itself be a way of transmitting signals between granule cell dendrites that share an adhesion junction. Thus a granule cell that makes such adhesion junctions with as many dendrites as possible has greater access to the state of other granule cells in the glomerulus. A particularly parsimonious and quick way to introduce a physiological change that has the capacity to act as a message across the adhesion junction would be to generate localized Ca^{++} depletion events in the cleft through the action of NMDARs. We chose to concentrate on Ca^{++} as it is a very important second messenger and previous studies have already shown that transient changes in $[Ca^{++}]_o$ can result in changes in cell physiology. (Katz and Miledi 1970; Mintz et al. 1995;Tang, et al, 1998).

We investigated further the hypothesis that NMDAR Ca^{++} currents may lead to depletions of extracellular Ca^{++} that can act as a signal between the two granule cells. Specifically we investigated how well those depletion events can be localized in space and time, as one of the important features of this depletion event would be its separability from other nearby depletion events. Our results showed that localized depletion events were separable in both space and time.

Lastly, we investigated the effect of the structure of glial sheath on spillover activation of NMDARs in the glomerulus and also on leakage of glutamate between two neighboring glomeruli. Our results showed that glutamate spillover is influenced by the shape of the glia and that under certain ensheathment conditions glutamate was able to leak into a neighboring glomerulus and prime the NMDARs there.

4. Insights from tomographic reconstructions of cerebellar glomeruli.

4.1 Introduction.

In the previous two chapters we examined how geometry of cerebellar glomeruli may influence their function. In chapter 2, we focused on global activity-dependent fluctuations in $[Ca^{++}]$ and showed that $[Ca^{++}]_o$ may experience prolonged changes whose duration is particularly sensitive to the tightness of glial ensheathment. Such fluctuations may affect release probability or plasticity at the mossy fiber to granule cell synapses or the Golgi cell axon to granule cell synapses. In chapter 3, we showed that glial ensheathment can play a role in determining the degree to which NMDAR's are activated on AJ's in the glomerulus and also the degree to which glutamate may leak from one glomerulus onto a neighboring glomerulus, thus linking glomerular structure to neurotransmission at the mossy fiber to granule cell synapse. In this chapter we will further enhance our models by including a more realistic geometries of cerebellar glomeruli.

A simplified approach to representing the influence of the complex extracellular structure and the contents of extracellular space on diffusing particles is to introduce a term into diffusion equations called tortuosity (λ) where,

$$\lambda = \sqrt{\frac{D}{D^*}}; \qquad (4.1)$$

here D is the diffusion coefficient in water and D^* is the diffusion coefficient in tissue, where λ can be either a scalar in the case of isotropic diffusion or a tensor in the case of anisotropic diffusion. The factors that give rise to tortuosity being greater than 1 can be split into two general categories: geometric and non-geometric. Geometric tortuosity relates the degree to which the manner in which cells occupy space obstructs the paths of the diffusing molecules thereby reducing the value of the effective diffusion coefficient in tissue. Non-geometric tortuosity represents the remaining contribution to the retardation of diffusing molecules caused by viscosity of the cerebrospinal fluid, buffering by the cell surfaces, steric hindrance by proteoglycans in the extracellular matrix (reviewed in Nicholson and Sykova, 1998; Sykova, 2004, Sykova, 2005).

Such a simplified representation is effective when an assumption can be made that the distance between the sites of relevance is long enough such that the absolute coordinates of the starting and ending locations do not influence the resulting λ (when λ is a scalar) or only the direction of the path matters (when λ is a tensor). This approach is insufficient however, for representing inhomogeneities in the tissue when the distance traveled by the molecules is on the order of the size of those inhomogeneities. Hence a simplified approach that is effective for diffusion distances greater than 100 μm where the local effects of extracellular morphology on the diffusion of molecules effectively "average out" would not work for a single cerebellar glomerulus where diffusion relevant to our questions only happens on the scale of 0.5- 2 microns. In fact, this reason motivated us to create explicit geometries for all our simulations.

The explicit geometries used in the two previous chapters were, however, highly stylized. Such stylized geometries do not represent the realistic structure of glomeruli. Furthermore, unlike parameters like diffusion coefficient or channel density, etc., relationship between any two differing instantiations of stylized geometries does not necessarily have an intuitive correspondence with a difference between two real geometries, therefore making a parameter sweep through geometries far less instructive than a corresponding sweep through other parameters. And as mentioned previously using particularly simplified representation of geometry will not be effective since as the diffusion distances pertinent to glomerular function are too short to allow for homogenization of geometric effects on the diffusing particles. Therefore, an important step in further refining our model would be to examine how a more realistic representation of the glomerular geometry influences our results.

In order to construct a model based on realistic glomerular structure we received assistance from NCMIR (National Center for Microscopy and Imaging Research). They generated two electron microscopic (EM) tomograms of portions of cerebellar glomeruli from rats. We used that data to generate two sets of 3D surface meshes where each surface mesh represents the best estimate of the surface of each cell inside the glomeruli. We then analyzed the diffusional properties of the surface

meshes by estimating the variability in classical geometric "tortuosity" with the two "glomeruli." In addition, we revisited some of the simulations we performed in previous chapters. Specifically, we measured how glial ensheathment affects re-equilibration of Ca^{++} in one of the new geometries. We also examined spillover of glutamate onto adhesion junctions after a single release event.

4.1.1 Effective tortuosity of glomeruli.

First we measured effective geometric tortuosity in the reconstructed glomeruli. While such measurements are meaningless when applied to a single pairing between a release site and a measurement site, we are still able to determine the average geometric tortuosity within the reconstructed volumes. We used two different methods for determining this "average" geometric tortuosity. First, we estimated the geometric tortuosity based on time courses of glutamate spillover between mossy fiber terminal-granule cell dendrite synaptic contacts. This value reports the average retardation along the diffusion paths relevant to glutamate spillover and does not necessarily report the true value of overall geometric tortuosity. Although we observed variability in spillover profiles between single pairs of release sites, we found good correspondence between the "averaged" effective tortuosity for the 2 reconstructed glomeruli. For the second method, we attempted to get an estimate of the geometric tortuosity in the regions that include the volume both near the glial sheath and farther away so as to get a representation of the geometric tortuosity value in the axon-dendritic milieu. To do this we replicated the technique used in Tao and Nicholson, 2004 where they estimated effective tortuosity by measuring evolution of diffusing ligands inside concentric cubic volumes. This method also produced a good correspondence between the effective diffusion coefficients of the two reconstructed volumes; however the tortuosity value based on the first method was consistently lower than that based on the second method.

4.1.2 Ca^{++} fluctuations.

In the last section of chapter 2 we discussed a model for comparing the effectiveness of differently structured glial sheaths at reducing the rate of Ca^{++} re-

equilibration in the glomerulus. Having a reconstruction of a glial sheath based on realistic geometry, we proceeded to test the effectiveness of the reconstructed glial sheath at slowing down movement of Ca^{++} into and out of the model glomerulus. We repeated the simulations we did in the last part of chapter 2 where we measured the time constant for Ca^{++} refilling within a glomerulus that has been "dipped" into a solution with a constant $[Ca^{++}]_o$. The time constant was ~ 16 ms - the lower bound of our original estimate.

4.1.3 Glutamate spillover.

Finally, we examined spillover of glutamate onto adhesion junctions in the reconstructed morphology. The measurements, in the region that we were able to access, showed that after a single release event peak glutamate concentration at a given AJ was not influenced by glial glutamate transporters and was influenced insignificantly by the effective glutamate diffusion coefficient, but was influenced significantly by its position relative to release sites on the mossy fiber terminal.

4.2 Methods.

4.2.1 Tissue preparation and electron microscopy (done at NCMIR by Ying Jones).

Fixation of brain: Two rats: 21 days old and 25 days old were perfused with a solution of 2% of paraformaldehyde/2.5% of glutaraldehyde in 0.15 M cacodylate buffer. Brains was taken out and post-fixed in same fixative for 2 hrs at 4°C. For cerebellum tissue, 100μm thick vibratome sections are obtained and kept in the fixative solution until high pressure freezing (HPF).

HPF: Brain sections were cut with 1.8 mm tissue puncher. This step ensures that the proper size of brain tissue will fit into the shallow side of a 100 μm-deep well in the type A HPF brass planchette (Ted Pella, Inc., Redding, CA). Trimmed brain tissue was loaded into the planchettes and the well was filled with 1-hexadecene. The planchette was then covered with the flat side of brass type B planchette, quickly loaded into a freezing holder and frozen with the Bal-Tec HPF 010. After freezing, the planchette sandwiches were separated under liquid nitrogen and the specimen/type A hats were place into a cryo-vial filled with freshly made 0.1% tannic

acid (EM grade, from Polysciences Inc., Warrington, Pennsylvania) in acetone (EM grade from Fullam Inc., Latham, New York).

Freeze-substitution procedure: The first step in the FS protocol was an incubation at –90°C for 72 hrs using the Leica EM AFS device. The substitution media was a solution of 0.1% tannic acid in acetone for 24 hr. Samples were then washed three times in cold acetone over a 2 hour period. Then, the solution was changed to 2% osmium tetroxide in acetone for 48 hrs at –90 °C. After substitution, the temperature was slowly raised to 20 °C over a period of 41 hrs with steps as shown in Table 1. The total time for this procedure is 113 hrs. Subsequently, the specimens were rinsed at room temperature for 10 minutes in pure acetone. Two additional pure acetone rinses were then performed at room temperature. Tissues were removed from the planchettes after the last wash step.

Infiltration and embedding: Infiltration was conducted over 3 days followed by embedding in Durcupan ACM resin (Electron Microscopy Science Inc., Hatfield, PA). Samples were infiltrated in 30% Durcupan in acetone for 4 hours and 50% Durcupan overnight. The next day, the specimens were placed into 70% Durcupan for 4 hours, 90% over 2 hours and were placed in 100% Durcupan for overnight incubation. After two incubations in fresh 100% Durcupan, the sample in 100% Durcupan was then oven polymerized in preparation for electron microscopy.

Thin section electron microscopy: Thin (80-100 nm) sections and thick (0.5-2 μm) sections were cut using a diamond knife (Diatome) and an Ultracut E ultramicrotome (Leica Microsystems, Bannockburn, IL) and mounted on uncoated copper grids. Thin sections were imaged at 80 keV using a JEOL 1200 electron microscope (JEOL, Peabody, MA) and thick sections were imaged at 400 KeV using a JEOL 4000EX intermediate voltage electron microscope.

Electron tomography data acquisition: Gold beads were applied to the top and bottom of section prior to image acquisition. For tilt series recorded at 10,000x magnification or higher, both 20 nm gold beads were used. Stereo pairs were collected prior to tomographic data collection to check that the tissue did not have any

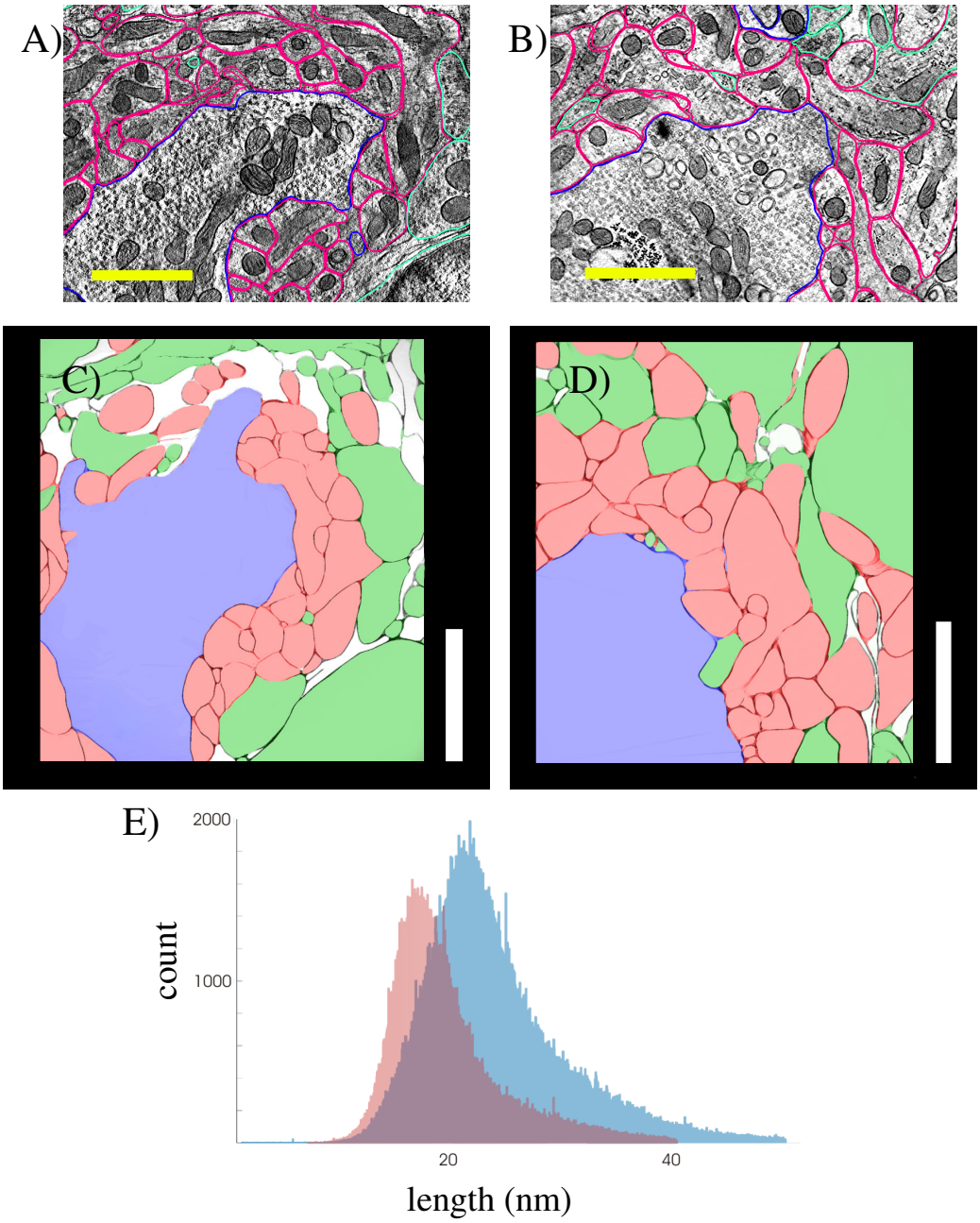

Figure 4.1. Tracing and mesh generation.
A) and B) contours of the first and second tomogram, respectively (bar = 1 µm).
C) and D) meshes of the first and second tomogram, respectively (bar = 2 µm).
E) nearest point-to-point distance histograms for first tomogram (red) and second tomogram (blue). (Dark blue shows the overlap between two histograms.

freezing damage. Images were collected using a 400 keV JEOL 4000EX electron microscope at 2° increments from –60 to +60° for both single and double tilt tomographic reconstruction following standard protocols (Mastronarde, 1997).

4.2.1 Tracing and mesh generation.

The two tomographic reconstructions were traced using IMOD (Kremer, et al, 1996). Mossy fiber terminal was identified by its size and presence of massive amounts of vesicles and synaptic contacts with granule cell dendrites. Granule cell dendrites were identified as objects that lacked vesicles, had synaptic contacts and shared adhesion junctions. Golgi cell axons were identified by presence of vesicles and peripheral location. Glial cells were identified by peripheral location, relative thinness, tendency to wrap around other structures, and "watery" appearance. All objects were contoured individually and the contours were converted into 3D surface meshes using "Contour tiler" software package (Bajaj, et al, 1996). Figures 4.1 (A) and 4.1 (B) show sample slices of the tomographic reconstructions of the first and second glomeruli, respectively, with some of the contours traced out. Colors correspond to tissue types with blue being the mossy fiber terminal, light red – granule cell dendrites, white – glial cells, and green – golgi cell axons and others. Figures 4.1 (C) and 4.1 (D) show the surface meshes with the color pattern the same as in A and B. Figure 4.1 (E) shows the distribution of nearest point-point distances on neighboring objects within each tomogram. The average for tomogram 1 was 18.6 nm with standard deviation = 5.7 nm. The average for tomogram 2 was 23.4 with standard deviation = 7.7 nm.

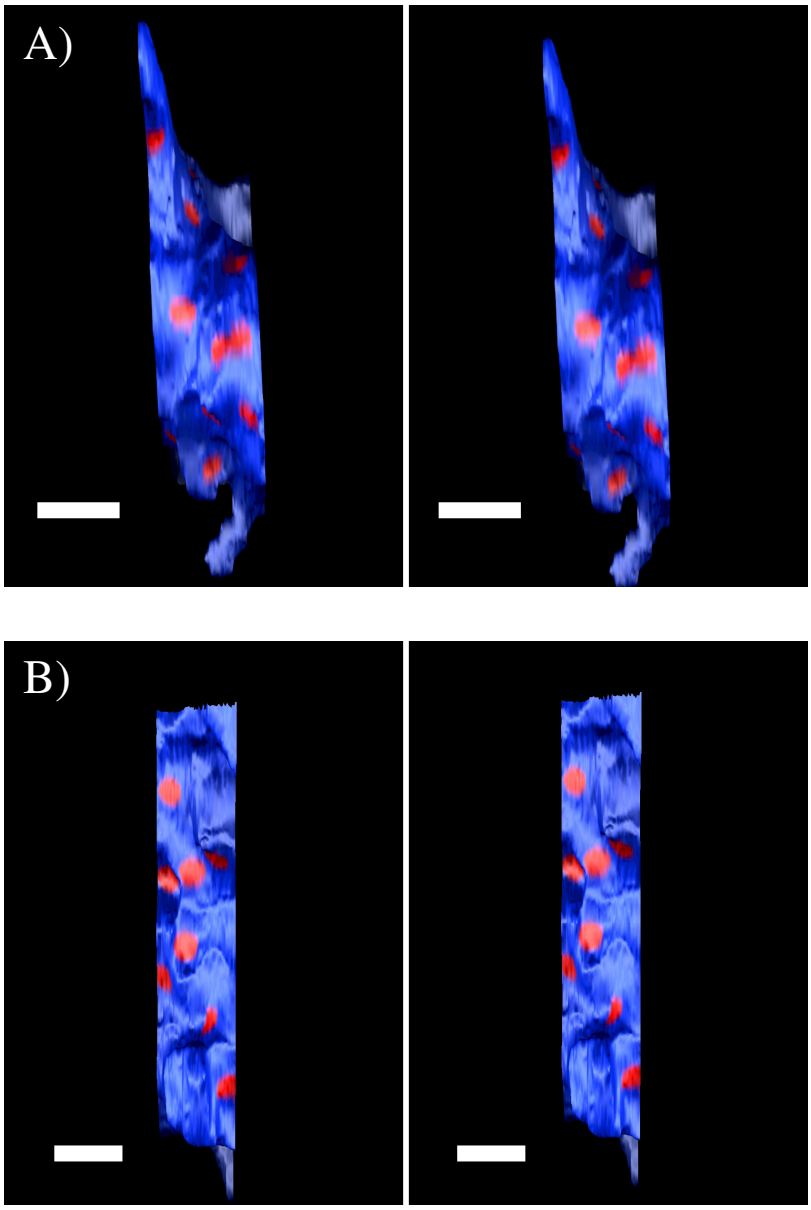

Figure 4.2. Stereo images of the distribution of synaptic contacts between the mossy fiber and granule cell dendrites.
In blue are the reconstructed mossy fiber terminal surfaces. Red spots indicated locations of the synaptic contacts. Stereo images are for cross-eyed viewing. Bar = 1 μm.

A) Mossy fiber terminal section and the release sites of the tomogram 1.
B) Mossy fiber terminal section and the release sites of the tomogram 2.

4.2.2 MCell simulations.

All simulations were done in MCell – a Monte Carlo simulator of cellular biophysics (Bartol, et al, 1991; Stiles et al, 2001; Stiles and Bartol, 2001). MCell uses rigorously validated and highly optimized Monte Carlo algorithms to simulate the random-walk Brownian motion of discrete diffusing molecules and concomitant uni- and bi-molecular chemical reactions in a complex three-dimensional environment reflecting realistic cellular microstructure. MCell has been used to model vesicular release (Stiles et al., 2001), diffusion in the synaptic cleft (Clements, 1996; Franks et al., 2002), and investigate the impact of neuronal shape on tortuosity (Tao and Nicholson, 2004).

4.2.3 Model setup for measurement of geometric tortuosity based on spillover paths.

The reconstructed polygonal meshes were used as geometries in the model. To generate appropriate boundary conditions, a mirror image for each set of meshes was created above and below the original data set. The 3 sets were fused with watertight seals. Only synaptic contacts in the middle copy were used for releases and for measurements.

500,000 diffusing ligands were released at each of those synaptic contacts and their time course of the ligand concentration was measured at every synaptic contact. Since each set of 500,000 ligands was uniquely tagged, each measured time course corresponded to a unique pairing between one release site and one measurement site. Figure 4.2 shows the distribution of the synaptic contacts at the mossy fiber terminals of glomerulus 1 - (A) and glomerulus 2 - (B). In glomerulus 1, synaptic contact density was ~ 2.0 sites / μm^2, with nearest site-to-site distance of 0.53 ± 0.23 μm. 95% of all synaptic contact sites lay within 1 μm of each other. In glomerulus 2, synaptic contact site density was ~ 2.2 sites / μm^2, with nearest site-to-site distance of 0.58+-0.14 μm. 100% of all sites lay within 1 μm of each other.We estimated the effective diffusion coefficient D^* for each pairing by fitting the set of all times to peak to the time to peak equation,

$$t_{peak-3D} = \frac{r^2}{6D^*}, \qquad (4.2)$$

where $t_{peak-3D}$ is the time to peak for 3D diffusion; r is the distance between the release site and the measurement site and D^* is the effective diffusion coefficient. Fitting was done in Matlab 6.5 (MathWorks, Natick, MA).

4.2.4 Model setup for measurement of tortuosity in concentric cubes.

We used the method of Tao and Nicholson, 2004 to analyze the relationship between geometric tortuosity and volume fraction. In our simulations three sites were chosen in the glomerulus 1 and glomerulus 2. They are indicated by white, red, and blue spheres in figure 4.3 A and B. 500,000 diffusing ligands were released per site and their evolution in time was counted within 9 concentric cubes. Figure 4.3 A shows stereo images of the evolution of the diffusing ligands within those 9 cubes at time = 0, 1.0 ms and 5.0 ms. The length of the sides of the 9 concentric cubes ranged from 0.2 μm to 1.8 μm with 0.2 μm step.

Evolution of the number of diffusing ligands within each of the cubes was fitted with:

$$N(t) = N_o[erf(\frac{a}{2\sqrt{D^*t}})]^3, \qquad (4.3)$$

where $N(t)$ is the number of diffusing ligands inside a cube whose side = $2a$; No is the number of released ligands; t is time; D^* is the effective diffusion coefficient. Fitting was done in Matlab 6.5 (MathWorks, Nantick, MA).

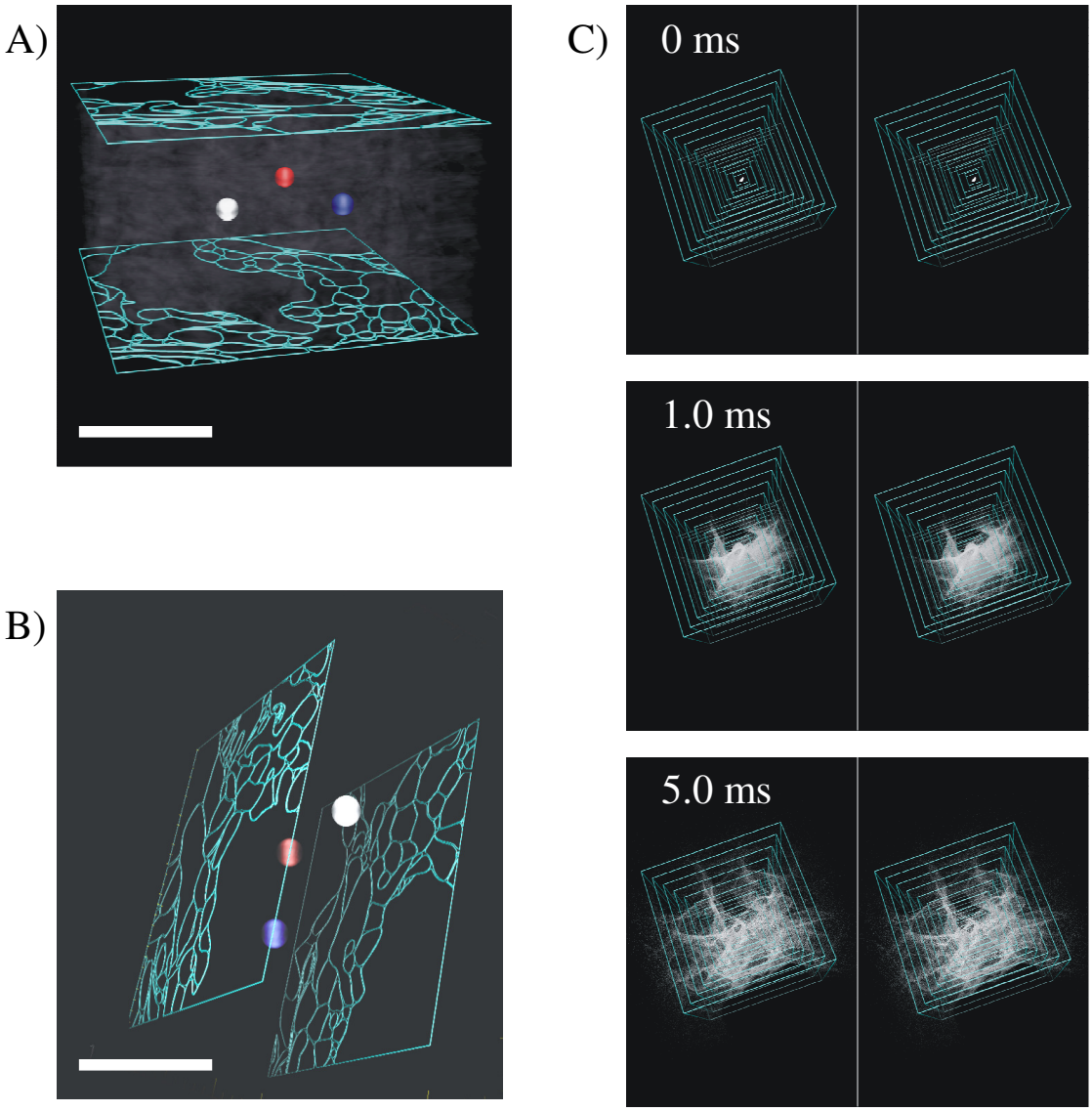

Figure 4.3. Setup and sample simulation of the determination of geometric tortuosity with concentric cubes.

A) White, red and blue spheres indicate positions of release sites in glomerulus 1, white box ~ 2 µm.
B) White, red, and, blue spheres indicate positions of release sites in glomerulus 2, white box ~ 2 µm A) and B) in cyan are outlines of the uppermost and lowermost surfaces of the reconstructions.
C) Stereo images of evolution of diffusing ligand released at white site in

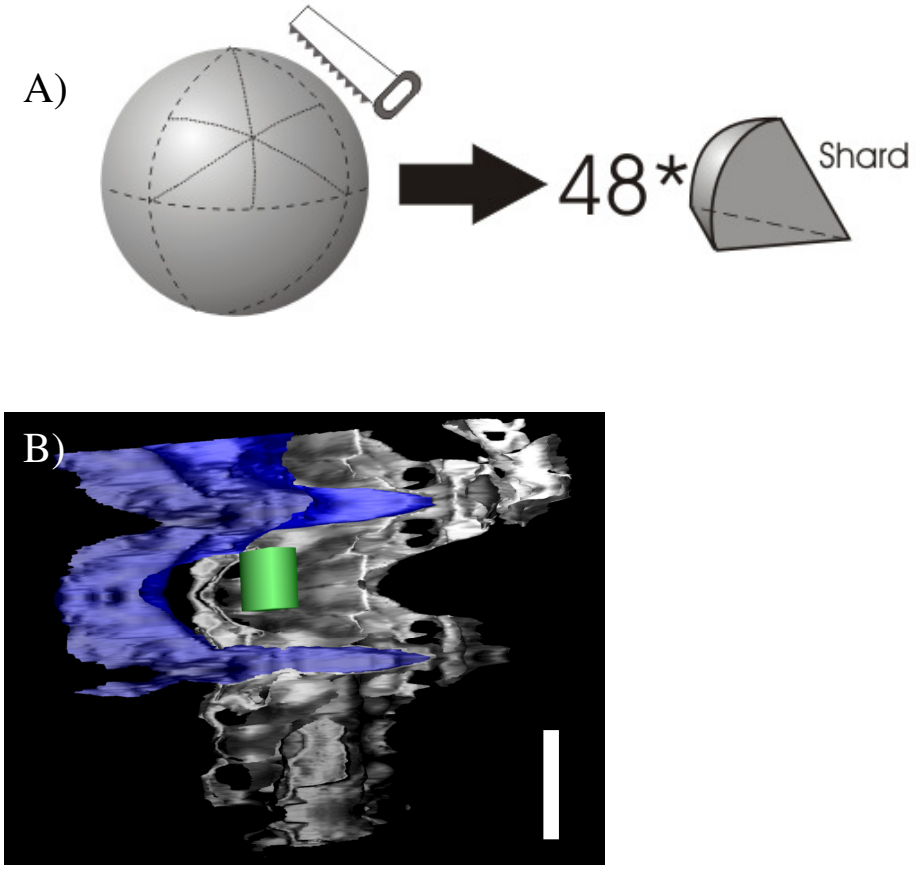

Figure 4.4. Model setup of Ca^{++} refilling simulations.
A) Sphere can be subdivided into 48 pieces, where if the 3 flat sides of the object are set to reflexive boundary conditions, would represent identical activity in all 48 parts of the sphere
B) A "shard" shaped piece was cut out of the data set. Only the glial sheath (gray) and the mossy fiber outer mesh (blue) are shown. Green – box in which Ca^{++} ions are counted. Bar = 1 μm.

4.2.5 Model setup for measurement Ca^{++} refilling of an empty glomerulus.

The principle behind this simulation is the same as the one behind simulation in chapter 2 that measured Ca^{++} refilling rate. The difference was that the current simulation estimated rates of Ca^{++} refilling in a more realistic geometry. Since we lacked access to an entire glomerulus, the first step was to create boundary conditions that would create spherical symmetry. In other words, we needed to find a way to cut

up a sphere into identical (may be chiral) pieces. One way to do this is to subdivide a sphere into 48 "shards" as shown in figure 4.4 A. The "shard" was inserted into the data set, which had to be replicated 7 times to fit the entire "shard", and the surfaces inside the shard were extracted. When simulations were run inside that volume, and the sides were set to reflexive boundary condition, it was equivalent to running a simulation in a pseudo-spherical object made up of those 48 pieces. Figure 4.8 (B) shows the glia and the mossy fiber terminal. The green box inside is where Ca^{++} ions were counted.

4.2.6 Model setup for glutamate spillover.

In this model setup we again needed to take advantage of the spherical symmetry. But, in this case, the most convenient location was chosen through an assumed middle of the glomerulus, and since the slice was much thinner than the presumed radius of the glomerulus, we simply cut out a slice with rectangular ends as shown in figure 4.5 A. Figure 4.5 (B) shows a stereo view of the simulated volume. Only mossy fiber and glia are shown. This is done to make the adhesion junction sites visible – green cubes). For simulations, glutamate diffusion coefficient was set to the following values: $1x10^{-6}$ cm^2/sec, $2.5x10^{-6}$ cm^2/sec, $5x10^{-6}$ cm^2/sec, $1\mathbf{x}10^{-5}$ cm^2/sec. Density of transporters on the glial sheath was varied: 0/μm^2, 1000/μm^2, 5000/μm^2, 10000/μm^2. The GluT kinetic scheme was the same as used in the previous chapter's figure 3.2. Due to damage to the peripheral regions of the tomogram 2, only tomogram 1 was used for this simulation.

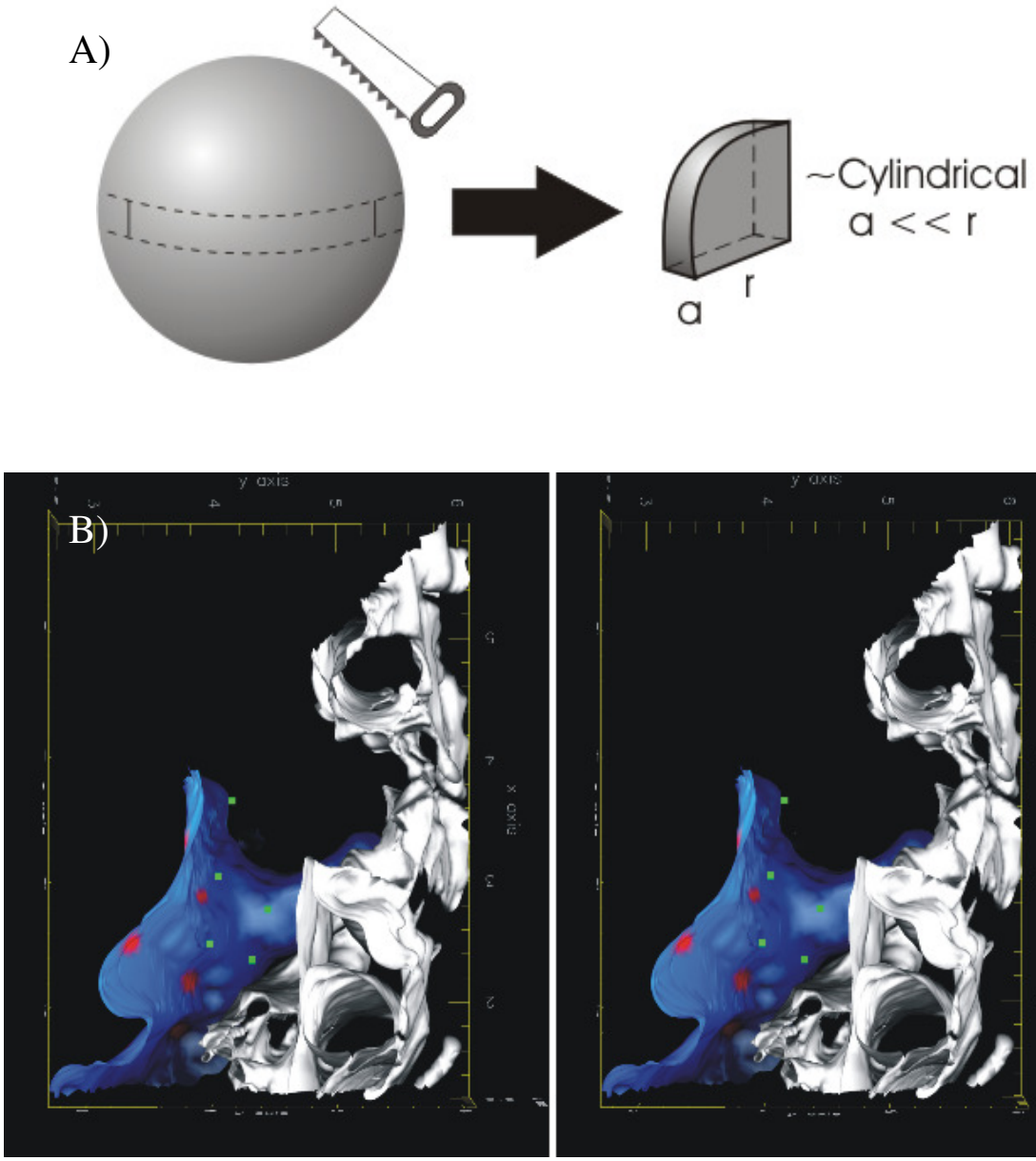

Figure 4.5. Glutamate spillover model setup.
A) If a slice is cut out of the sphere near the center, then the slice is nearly cylindrical. Therefore we can assume reflexive boundary conditions at the top and the bottom.
B) Stereo image view of the model. A "wheel" was cut out of the model and then chopped into eigths. Glial sheath is in white, mossy fiber terminal is in blue. Red spots indicate sites of glutamate release. Green cubes indicate sites of adhesion junctions.
Stereo image is set up for cross-eyed viewing.

4.3 Results.

4.3.1 Comparison of glial shape in different regions near the glomerulus.

Of particular interest was the observation of the glomerular structure of glomerulus 1. In it, glial morphology was far better preserved than in glomerulus 2 and we were fortunate to obtain a region of a glomerulus where on one side the glomerulus was abutted by highly complex neuropil while on the other side glomerulus was abutted by the granule cell soma. As shown in figure 4.6, the glial cell at the interface between the glomerulus and the neuropil was far more structurally complex and occupied more volume than the glial sheath between the granule cell soma and the glomerulus.

4.3.2 Measurement of tortuosity along the spillover paths.

We first examined at how structure of the reconstructions shapes the paths between synaptic contacts as a way of measuring geometric tortuosity of the glomerular structure along those paths. Figure 4.7 (A) shows the results of all the simulations and the estimated value of tortuosity obtained from them. The estimated values were 1.27 for tomogram 1 and 1.28 for tomogram 2.

4.3.3 Measurement of tortuosity inside concentric cubes.

Figure 4.8 shows the time courses of ligand diffusion in the concentric cubes simulations. Below are the numerical averages of the 9 estimates for each of the 6 simulations: glomerulus 1, “white” site: mean λ =1.35, std = 0.046, “red” site: mean λ = 1.41, std = 0.012; “blue” site: mean λ = 1.27, std = 0.034; glomerulus 2, “white” site: mean λ = 1.32, std = 0.033, “red” site: mean λ = 1.28, std = 0.0057, “blue” site: mean λ = 1.35, std = 0.026.

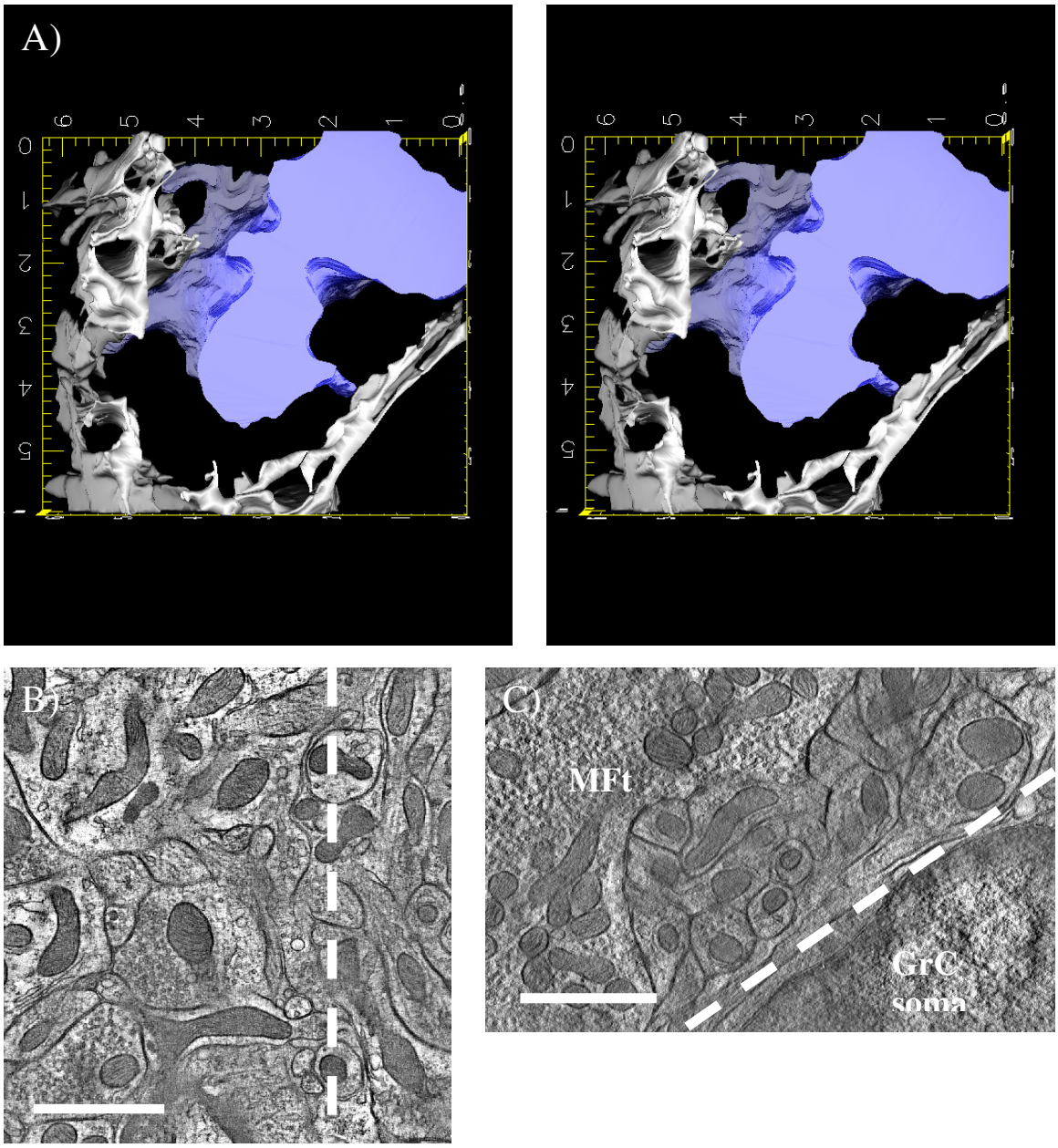

Figure 4.6. Glial shape is more complex on the side where glomerulus interfaces with more complicated neuropil.
A) Mossy fiber shown in blue and glia in white, other objects were removed for clarity. Stereo image is for cross-eyed viewing. Scale is given in microns.
B) Section of the EM tomogram showing the mix of different axons and dendrites to the left of the glial sheath. Dashed line goes ~ through the center of the glial sheath.
C) This image corresponds to the lower right region of A). As can be seen from the image, the object behind the glial cell is a granule cell body. Dashed line runs ~ through the middle of the glial sheath. B and C) bar = 1 μm.

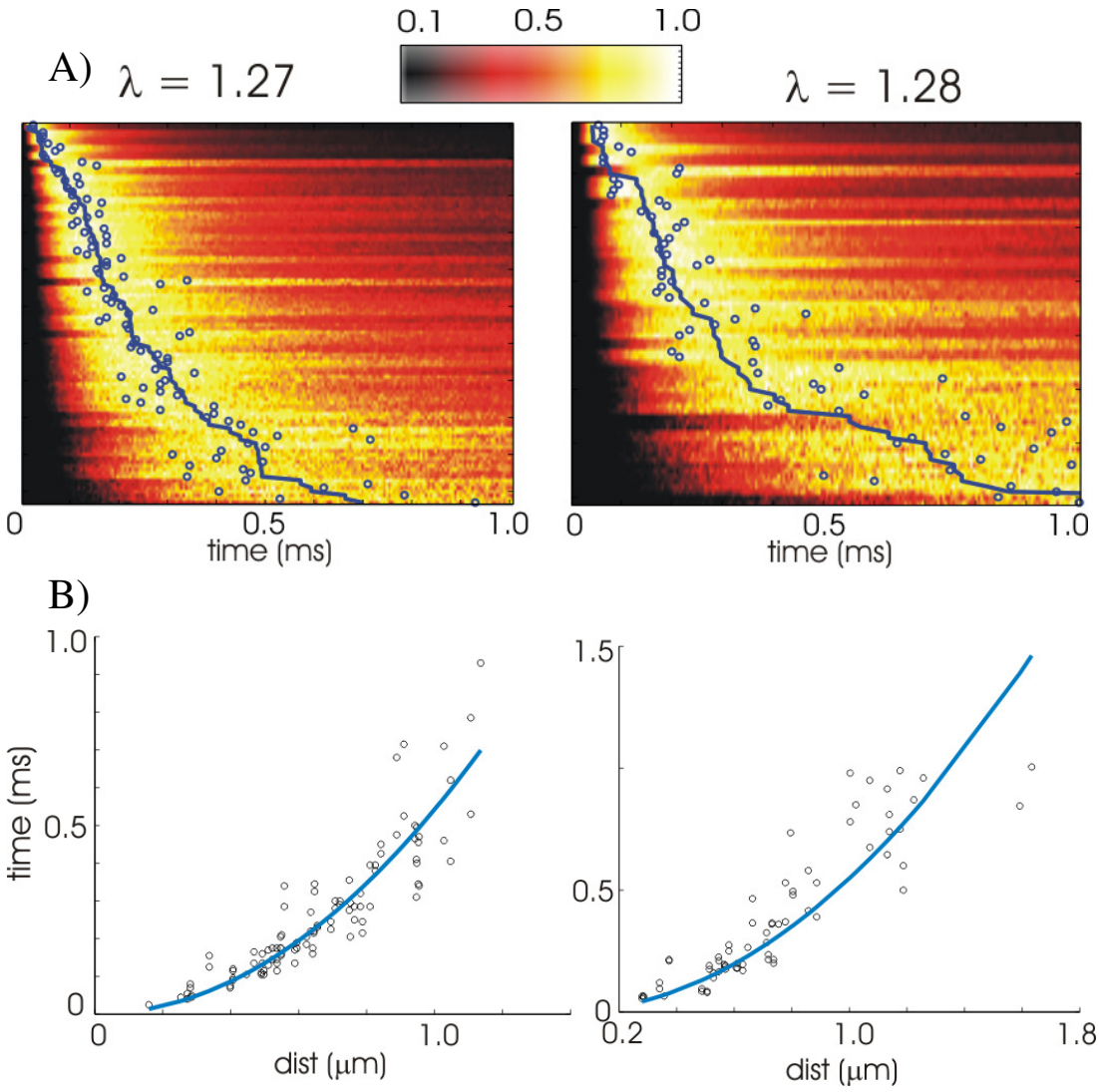

Figure 4.7. Tortuosity of spillover paths in the two reconstructions.

A) Time courses of spillover at glomerulus 1 (left) and glomerulus 2 (right). All the time courses were normalized to the peak concentration. Concentration profiles were ordered along the y-axis from nearest to farthest. Blue circles correspond to the actual times to peak in each simulation. Dark blue lines correspond to the theoretical time to peak values. As described previously, we were able to estimate the effective diffusion coefficient from the times to peak. The new diffusion coefficient yielded $\lambda = 1.27$ for the tomogram 1 and $\lambda = 1.28$ for tomogram 2.
B) The two curves show the relationship between site-to-site distance and the times to peak. The same information is given in A, however now the distance scale is uniform and hence the blue fitted curves are smooth. Gray circles correspond to the actual times to peak.

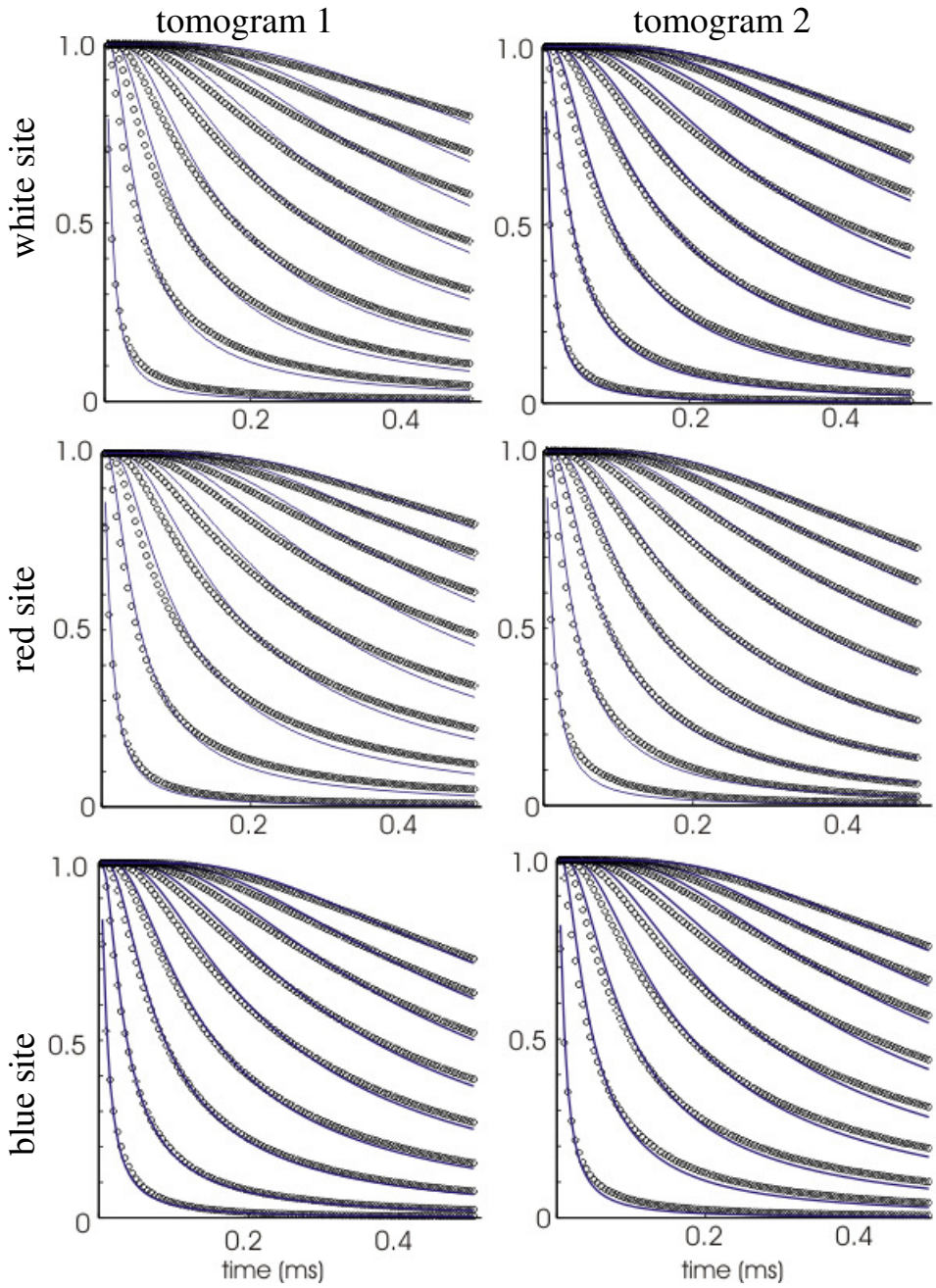

Figure 4.8. Estimated evolution of diffusing ligands in concentric cubes.
The columns are the tomograms, the rows are the release sites.
Circles correspond to actual measurements. Lines are given by the estimate as given in equation 4.3. In each plot, from left to right the curves correspond to the faction of total number of ligands released. Thus the leftmost curve (one that falls fastest) corresponds to the smallest box.

4.3.5 Measurement of Ca^{++} re-equilibration.

Figure 4.9 shows the time course of Ca^{++} during refilling of the model glomerulus. In order to simulate 2 mM outside [Ca^{++}] we created a surface 20 nm outside the glial cell a surface 20 nm outside the glial sheath. This surface was designed to generate Ca^{++} ions at a constant rate and to remove Ca^{++} ions that came in contact with the surface .Ca^{++} re-equilibration inside the glomerulus had the time constant of ~16 ms at the diffusion coefficient of $3x10^{-6}$ cm^2/sec.

4.3.6 Glutamate spillover.

Locations of the adhesion junction sites discussed in figure 4.11 are shown numbered in figure 4.10. Figure 4.11 shows the time courses of spillover glutamate at 5 adhesion junctions. Of the five sites examined glial position had small effect on the peak glutamate concentration. Instead it was the positioning of the adhesion junctions relative to the release sites that had the most significant effect on the peak glutamate concentration. Green curves show the time courses of differential contribution of glutamate from different sets of sites. This measure indicates that at release probability below 100%, some sites can potentially contribute significantly higher glutamate than others. Since the distance between the release sites and the periphery (the limit) of our model is only ~ 1-2 μm, it was impossible to measure longer term phenomena, as the boundary conditions would have been inconsistent with realistic geometry.

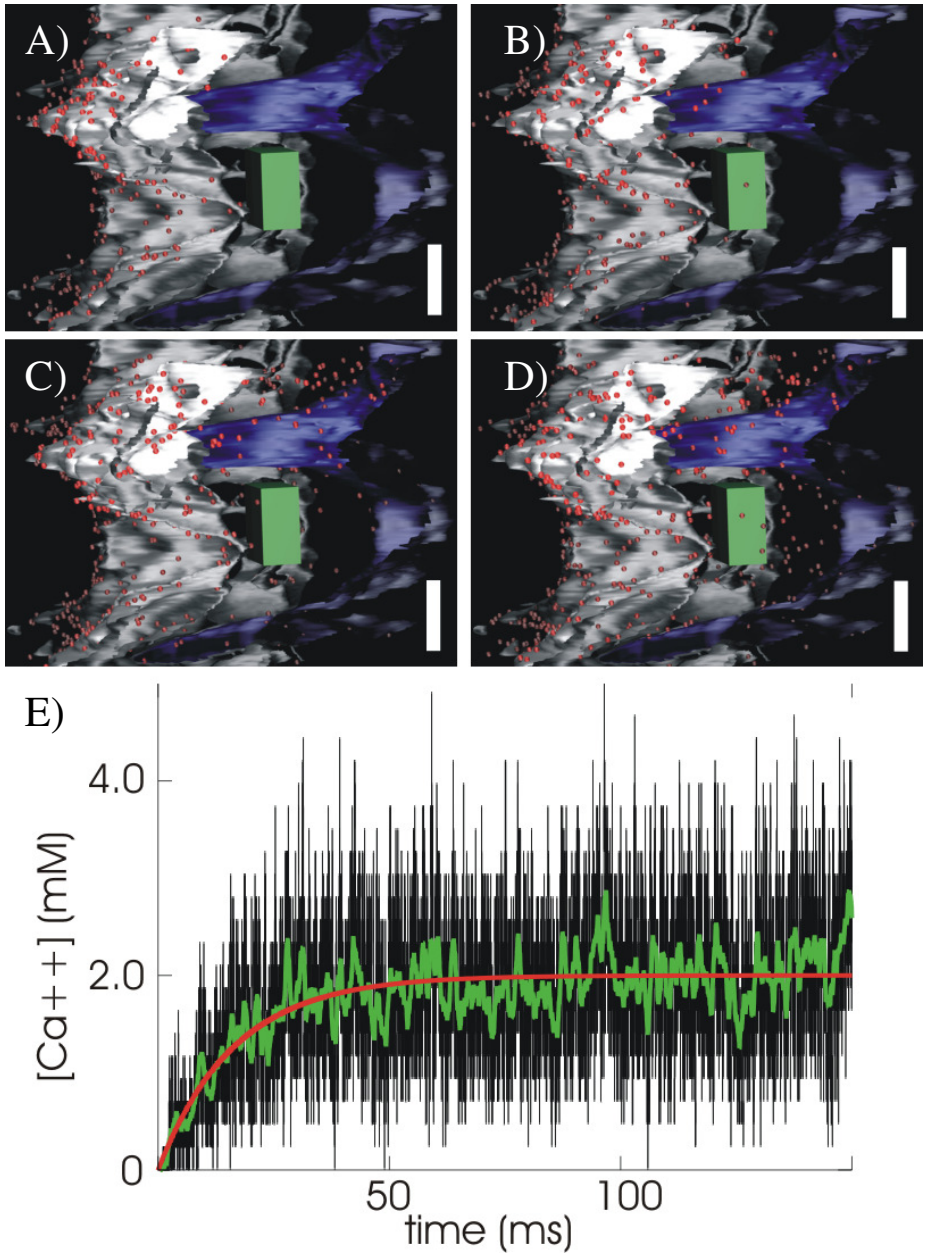

Figure 4.9. Time course of Ca^{++} re-equilibration.
A) through D) At time 0, glomerulus is emptied out of all Ca^{++}, then at time 0 2 mM infinite pool of Ca^{++} is created just outside the glial sheath (to the left, in the images). Subsequently, Ca^{++} (red spheres) diffuse inside the glomerular volume, where they are counted inside the green box. Bar = 1 mm. A) The state of the simulation 0.1 ms after time 0, B) 1 ms after time 0, C) 10 ms, D) 20 ms.
E) Actual time course (black) course is fitted with an exponential (red). In green is the running average of the actual time course with 1 ms window.

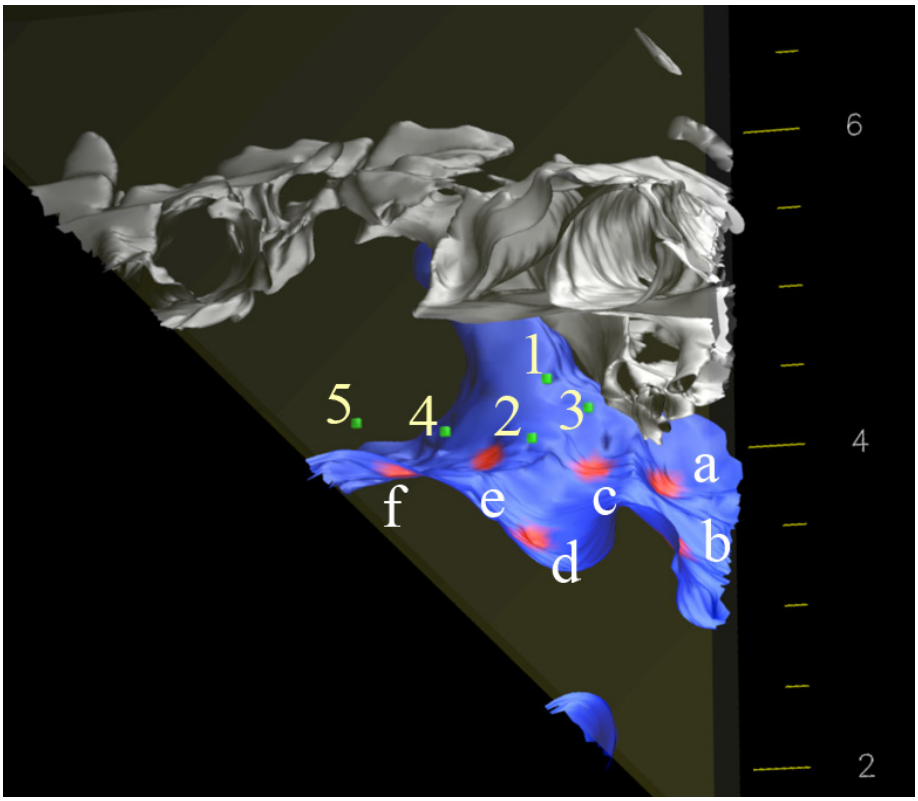

Figure 4.10. Arrangement of adhesion junctions and release sites.
The following five figures show the time course of glutamate concentration at 1 of the 5 adhesion junctions numbered here from 1 to 5. The release sites relevant to the simulations are indicated with letters a-f. Correspondence between color and object type remains the same in this image as in the previous image: glial sheath is colored gray, mossy fiber terminal is blue, release sites are marked with red and adhesion junction sites are marked by green boxes where glutamate was measured.

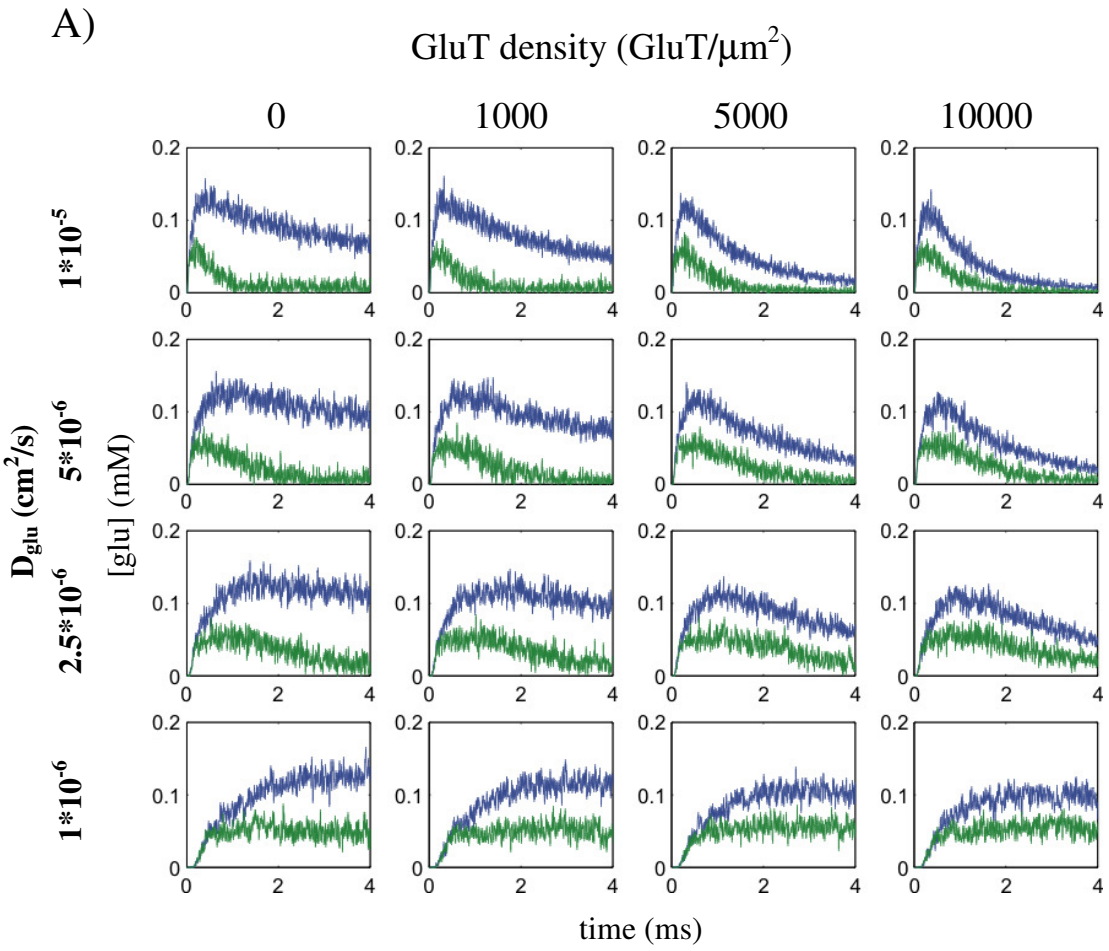

Figure 4.11. Time courses of glutamate at AJ site #1.
The following terminology will be used for describing the graphs. Glutamate time course which results from releases at sites a, b, and c within a single simulation will be written as SR(a + b + c). If a single plot shows a sum of glutamate time courses that came from different simulations, where in the first simulation release occurred at a, in the second simulation release occurred at b, and in the third at c, then the term that describes such a curve will be SR(a)+SR(b)+…+SR(c), where SR stands for single release.
In the plots above blue curve corresponds to SR(a+b+c+d+e+f), with letters corresponding to the release sites identified in figure 4.8, green curve corresponds to absolute value of SR(a+b+c)-SR(d+e+f).
Each row shows glutamate concentration time course at the diffusion coefficient given to its left. Each column shows glutamate time course at the glutamate transporter density given above.

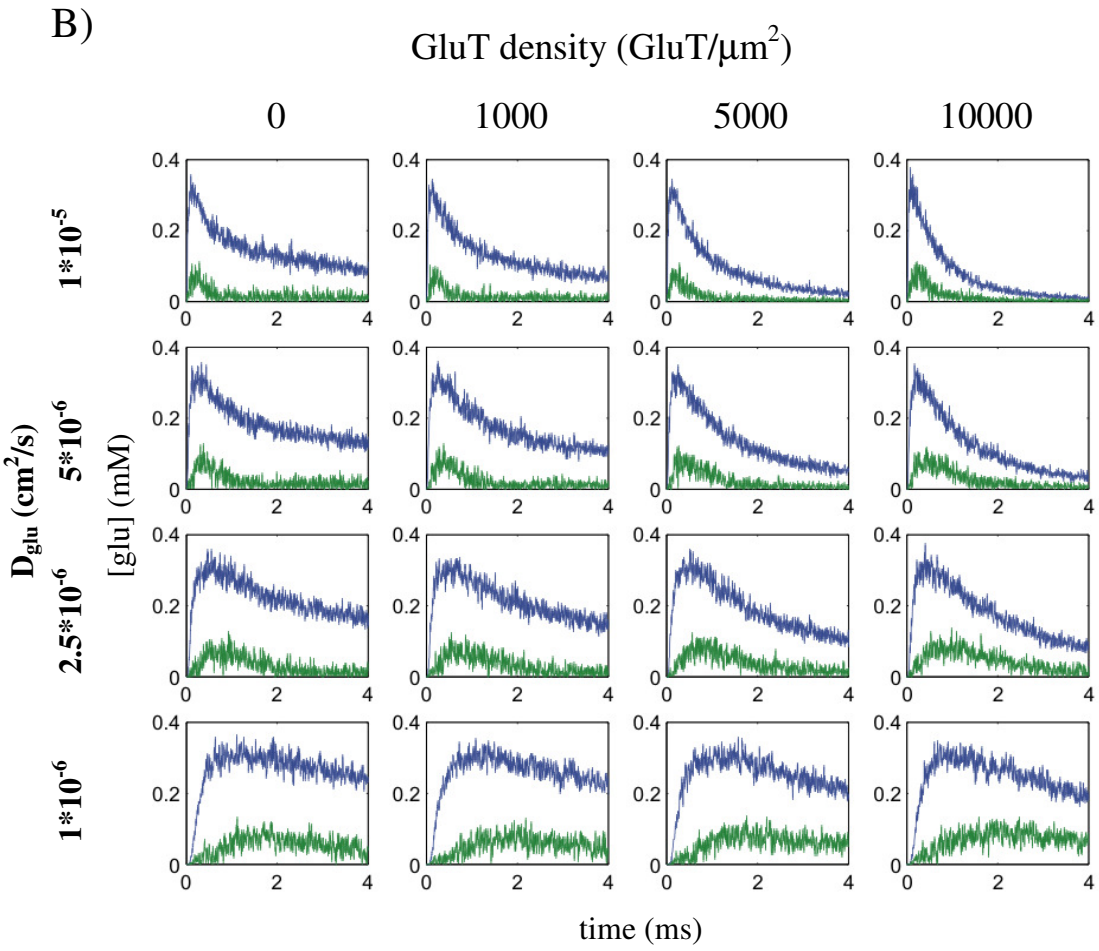

Figure 4.11. Time courses of glutamate at AJ site #2.
The following terminology will be used for describing the graphs. Glutamate time course which results from releases at sites a, b, and c within a single simulation will be written as SR(a + b + c). If a single plot shows a sum of glutamate time courses that came from different simulations, where in the first simulation release occurred at a, in the second simulation release occurred at b, and in the third at c, then the term that describes such a curve will be SR(a)+SR(b)+…+SR(c), where SR stands for single release.
In the plots above blue curve corresponds to SR(a+b+c+d+e+f), with letters corresponding to the release sites identified in figure 4.8, green curve corresponds to absolute value of SR(a+b+c)-SR(d+e+f).
Each row shows glutamate concentration time course at the diffusion coefficient given to its left. Each column shows glutamate time course at the glutamate transporter density given above.

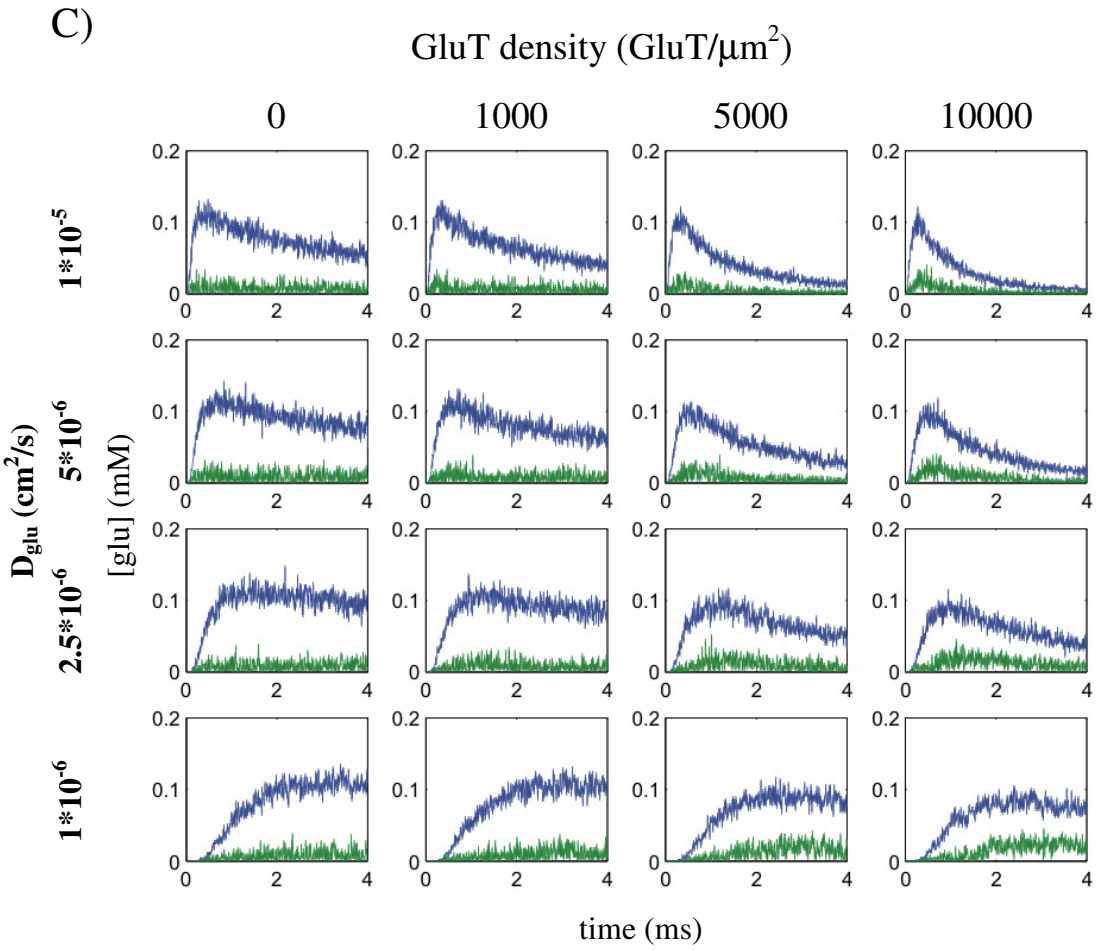

Figure 4.11. Time courses of glutamate at AJ site #3.
The following terminology will be used for describing the graphs. Glutamate time course which results from releases at sites a, b, and c within a single simulation will be written as SR(a + b + c). If a single plot shows a sum of glutamate time courses that came from different simulations, where in the first simulation release occurred at a, in the second simulation release occurred at b, and in the third at c, then the term that describes such a curve will be SR(a)+SR(b)+…+SR(c), where SR stands for single release.
In the plots above blue curve corresponds to SR(a+b+c+d+e+f), with letters corresponding to the release sites identified in figure 4.8, green curve corresponds to absolute value of SR(a+b+c)-SR(d+e+f).
Each row shows glutamate concentration time course at the diffusion coefficient given to its left. Each column shows glutamate time course at the glutamate transporter density given above.

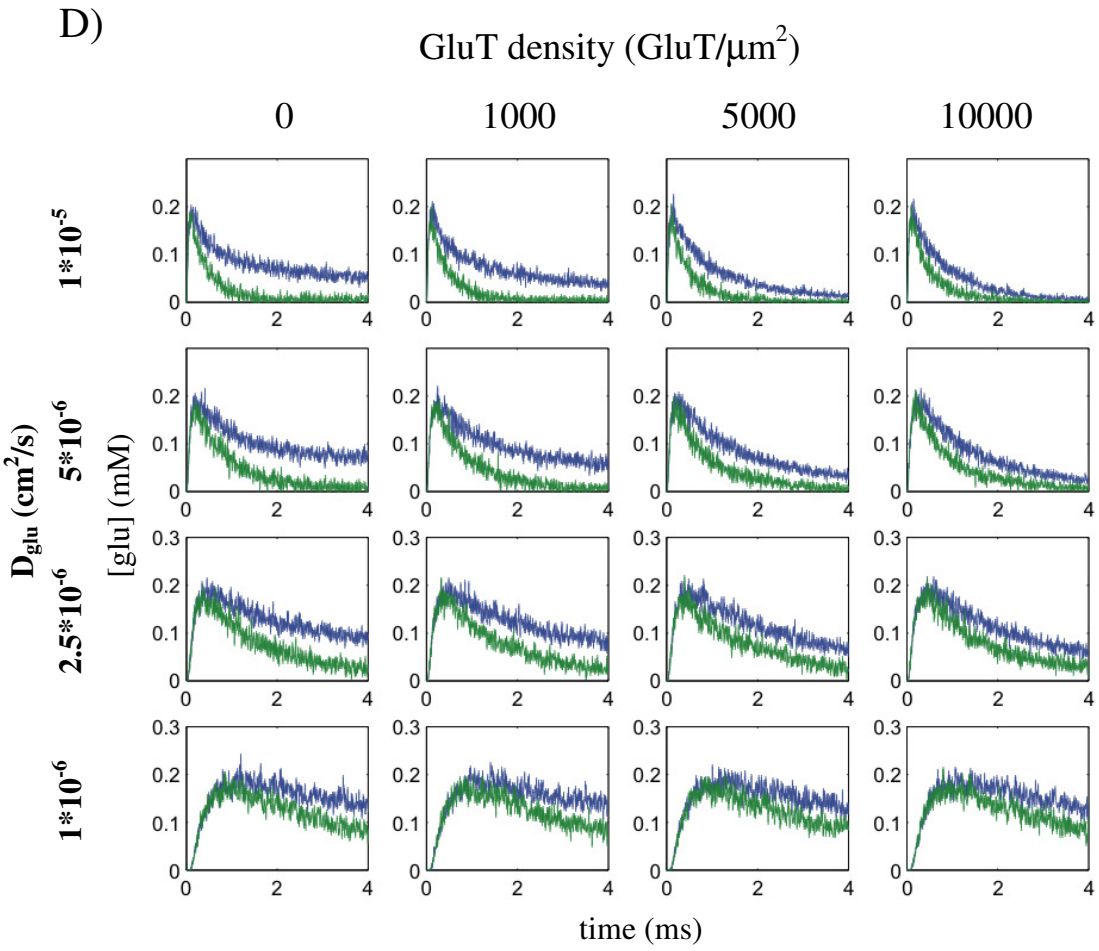

Figure 4.11. Time courses of glutamate at AJ site #4.
The following terminology will be used for describing the graphs. Glutamate time course which results from releases at sites a, b, and c within a single simulation will be written as SR(a + b + c). If a single plot shows a sum of glutamate time courses that came from different simulations, where in the first simulation release occurred at a, in the second simulation release occurred at b, and in the third at c, then the term that describes such a curve will be SR(a)+SR(b)+…+SR(c), where SR stands for single release.
In the plots above blue curve corresponds to SR(a+b+c+d+e+f), with letters corresponding to the release sites identified in figure 4.8, green curve corresponds to absolute value of SR(a+b+c)-SR(d+e+f).
Each row shows glutamate concentration time course at the diffusion coefficient given to its left. Each column shows glutamate time course at the glutamate transporter density given above.

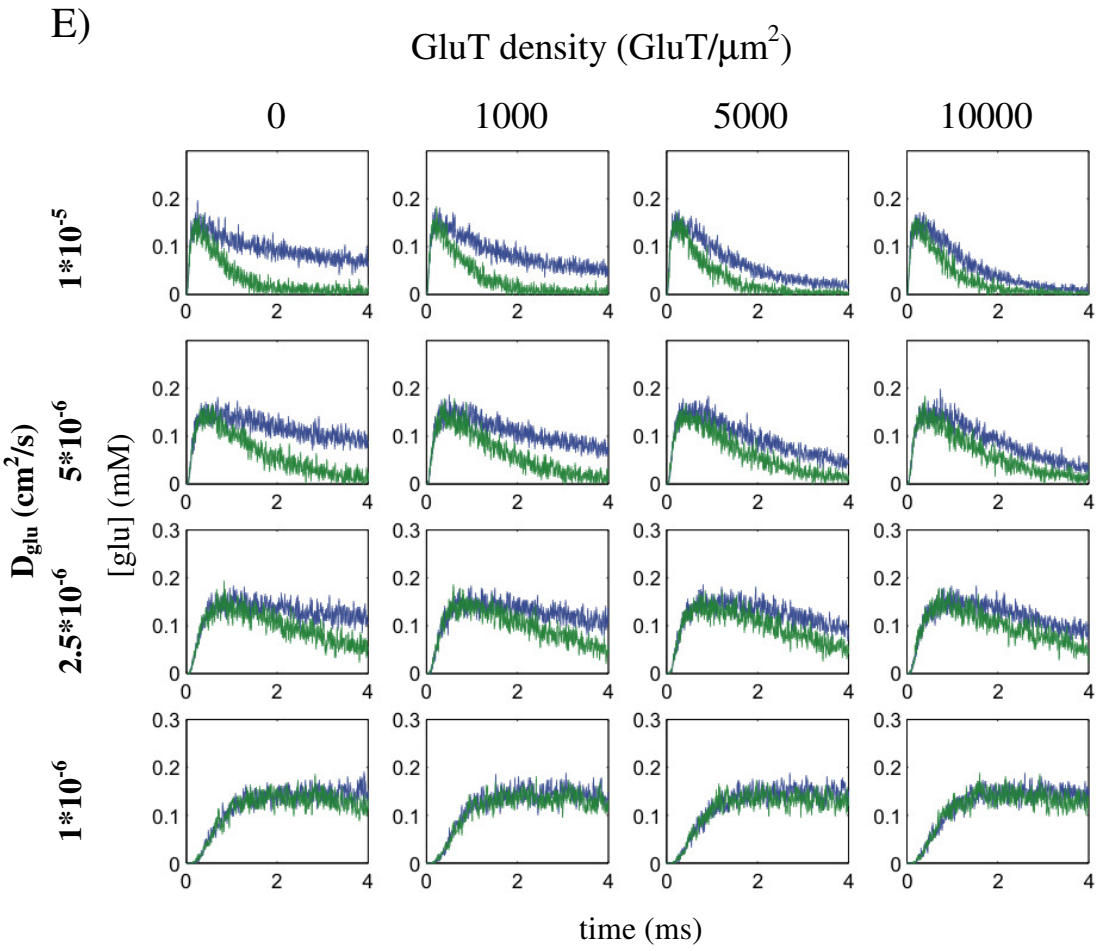

Figure 4.11. Time courses of glutamate at AJ site #5.
The following terminology will be used for describing the graphs. Glutamate time course which results from releases at sites a, b, and c within a single simulation will be written as SR(a + b + c). If a single plot shows a sum of glutamate time courses that came from different simulations, where in the first simulation release occurred at a, in the second simulation release occurred at b, and in the third at c, then the term that describes such a curve will be SR(a)+SR(b)+…+SR(c), where SR stands for single release.
In the plots above blue curve corresponds to SR(a+b+c+d+e+f), with letters corresponding to the release sites identified in figure 4.8, green curve corresponds to absolute value of SR(a+b+c)-SR(d+e+f).
Each row shows glutamate concentration time course at the diffusion coefficient given to its left. Each column shows glutamate time course at the glutamate transporter density given above.

4.4 Summary.

We reconstructed two electron microscopic tomograms of rat cerebellar glomeruli. And the resulting two sets of 3D polygonal meshes were used in MCell simulations. First we estimated the effective geometric tortuosity using 2 different methods. The geometric tortuosity was between 1.27-1.34.

In addition we used one of the newly reconstructed tomograms to estimate the rate of Ca^{++} influx into the glomerulus. Refilling had ~ 16 ms time constant which was comparable with the lower bound estimates obtained in the more stylized geometry in chapter 2. This is however but one sampling of glial geometry that appears to be quite distinctive even within a single glomerulus as we show in figure 4.6. More studies need to be done to establish a range of these values among glomeruli. In addition, these values will likely change as a result of long term changes such as aging or disease, or short term changes such as activity-induced glial swelling (Sykova, 2005).

The most surprising result was the relatively poor fits between the time course predicted by the equation and the actual time courses. The most reasonable explanation for the poor fits is the fact that in Tao and Nicholson paper, the concentric boxes occupied significantly greater volumes, and in fact, the volumes in these simulations were so small that the diffusion did not have the opportunity to become homogenized.

Lastly we examined spillover onto the adhesion junctions in one of the glomeruli.

The results showed that the peak glutamate concentration depends on the location of the release sites relative to the measurement site.

4.5 Future directions for the reconstructions.

In this section we will introduce some ideas about future enhancements to the model as well as a preliminary exploratory study that examined the contribution of the glial sheath to the geometric tortuosity of the diffusion paths across it. First we

will describe the study that attempted to measure the effect of glial sheath on the diffusion coefficient.

4.5.1 Measurement of Ca^{++} flow.

In these simulations, our aim was to compare the rate of diffusion between pairs of site located on the same side of the glial sheath with the rate of diffusion between sites located on opposite sides of the glial sheath. If glial structure retards flow of Ca^{++}, then effective diffusion coefficient between the two sites should be lower than the effective diffusion coefficient between the sites inside or outside the glial sheath. 5 sites were chosen just inside and 5 sites were chosen just outside the glial sheath as shown in figure 4.12 (A). Ca^{++} was released and measured at each site. Since all Ca^{++} molecules coming from each release site were uniquely tagged, each measured time course corresponded to a unique pairing between the release and the measurement site. Time to peak information was insufficient to properly fit the resulting Ca^{++} profiles. Instead we used the entire 3D diffusion equation,

$$C(r,t) = \frac{N_o}{(4\pi D^* t)^{3/2}} \exp\left(\frac{-r^2}{4D^* t}\right), \qquad (4.4)$$

where *C(r,t)* is the concentration of Ca^{++} at some distance *r* between the two sites at time *t*; *No* is the number of molecules initially released; *D** is the effective diffusion coefficient (Crank, 1975). A sample fitted time course is shown in figure 4.12 (B). Fitting was done in Matlab 6.5 (MathWorks, Natick, MA). Due to damage to the peripheral regions of the tomogram 2, only tomogram 1 was used for this simulation.

The original diffusion coefficient used in the simulations was 5×10^{-6} cm^2/sec. As some of the fits did not converge, the number of simulations used to estimate the effective diffusion coefficient is less than the total number of pairings. The effective diffusion coefficient in the simulations where Ca^{++} had to diffuse between sites inside the glomerulus was 3.3×10^{-6} cm^2/sec with standard deviation of 0.078×10^{-6} cm^2/sec (N = 20). The effective diffusion coefficient on the outside was 3.3×10^{-6} cm^2/sec with

standard deviation of $0.03x10^{-6}$ cm^2/sec (N=20). The effective diffusion coefficient for cross diffusion was $0.26x10^{-6}$ cm^2/sec with standard deviation of $0.015x10^{-6}$ cm^2/sec (N=9). Therefore there was an effective reduction of 20% in the diffusion coefficient.

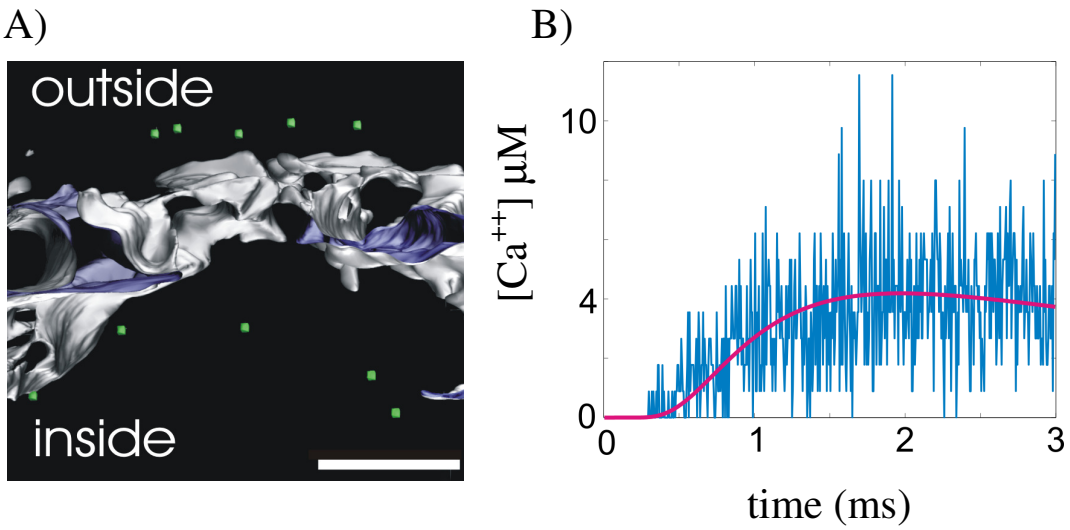

Figure 4.12. Time course of Ca^{++} diffusion across the glial sheath.
A) 5 Ca^{++} release sites were placed inside the glial sheath and 5 were placed outside. Only glial sheath (grey – external surface/dark blue- internal surface) is shown in the image. In the actual simulations, all the structures were used. Bar = 1 µm.
B) $[Ca^{++}]$ was released at each site and measured at every other site for each release event. Subsequently, $[Ca^{++}]$ time course was fitted with 3D diffusion equation (Crank, 1975). Here, in blue is a sample time course of $[Ca^{++}]$ and in red is the fit

These results are consistent with other measurements described in this chapter that indicate a very fast refilling time for an empty glomerulus. This, however, does not necessarily imply that glomeruli cannot experience protracted Ca^{++} depletion as the ensheathment by glial cells may change as a result of biophysical activity. A study of whether such changes are realistic at glomeruli is one of the available future directions in the development of the model of cerebellar glomeruli. Additional enhancements to the model are discussed in the following section.

Appendix: Reflexive boundary conditions.

In the context of differential equations, a reflexive boundary condition is defined as

$$\frac{\partial f(x=0,t)}{\partial x} = 0, \qquad (4.A.1)$$

where *f*, defined over *(0,r)*, is a function of *x* (position) and *t* (time). Here $x = 0$ is the edge of the region for which *f* is defined. Such a condition does not have to exist at edges

only. It can also exist at all points in space *x*, where there the above condition holds for all times during the evolution of *f*. For example, if a system started at steady state equilibrium, this condition holds everywhere at all times.

This condition is equivalent to having a "virtual" function *f'* defined over *(-r,0)* that mirrors evolution of *f* for all times *t*. Figure 4.13 (A) shows a path of a single diffusing particle obeying the reflexive boundary condition – where the path of the particle into the "virtual region" is reflected back across the boundary.

The mirror image property of reflexive boundary condition, for which it presumably bears it's name, makes it a very powerful tool when applied to modeling large systems with inherent symmetries as it allows to reduce the computational load by modeling only a part of the system with reflexive boundary conditions. The part chosen must be large enough to be representative of the conditions in the entire system and it has to have the correct structure that allows a requisite number of these parts or their mirror images be put back together into the original system. Figure 4.13 (B) shows a choice of reflexive boundary condition for a system with a specific asymmetry.

In MCell, reflexive boundary conditions are represented as walls that bounce the diffusing ligands back in a way that follows the reflection rule, i.e. angle of incidence = angle of reflection. It is important to note that it is not the ligand that is being reflected but the path of the ligand into the "virtual space." Thus the ligand only travels the remainder of its step length. It is easy to see why this should be the case: if the ligand were truly reflected, i.e. traveled the same distance after the bounce as before, then it would effectively have travelled a greater distance (unless it hits at

exactly half-way) than if there were no boundary and the requirement for reflexivity would not be faithfully maintained.

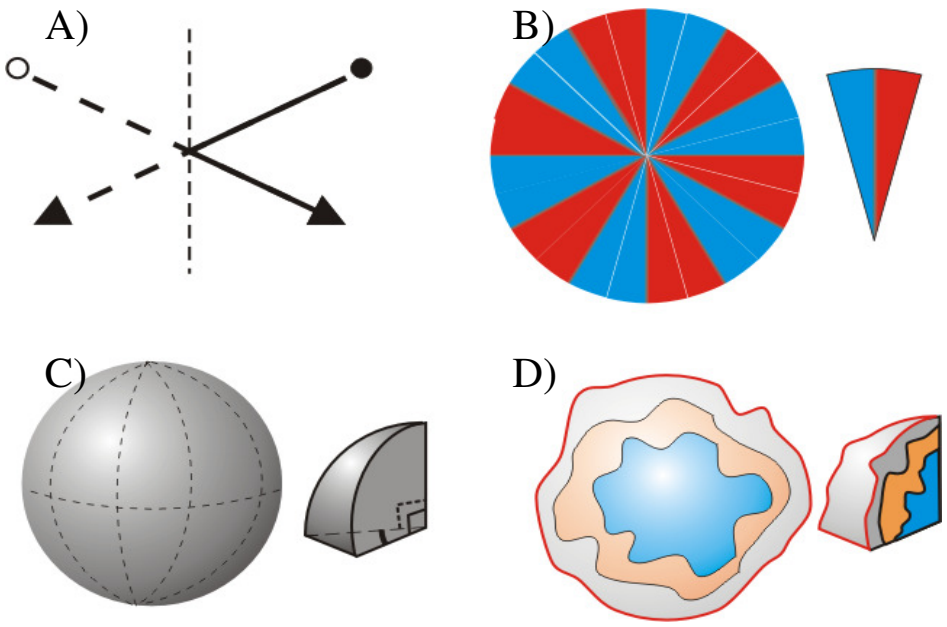

Figure 4.13. Reflexive boundary conditions.
A) Illustration of the meaning of the concept of reflexive boundary condition. Dashed vertical line represents the edge of the simulated space. Space to the right of the dashed vertical line is the simulated space. Filled circle is a diffusing ligand whose movement step in space in a given time step is indicated by a black arrow. Having a reflexive boundary condition is equivalent to having an identical virtual ligand (open circle) in the virtual "simulation" to the left of the dashed vertical line travel the mirror image of the straight path that would have been traveled by the filled circle had the boundary not been there. So, as the filled circle "leaves" the space of the simulation, its virtual "twin" appears and finishes the step.
B) Subdivision of a 2D model system. Assume the colors in the wheel represent intrinsic asymmetry of the system, then care must be taken to represent those asymmetries in proper proportions in the simulated space, which in this case is a slice composed of one red slice and one blue slice.
C) One possible way to subdivide a 3D sphere – into half slices.
D) Assuming a nearly spherical glomerulus, we choose a half slice which is intended to be representative of the entire glomerulus.

References

Albus, J.S. (1971). The theory of cerebellar function. *Math Biosci*, 10:25-61.

Altman, J. (1972). Postnatal development of the cerebellar cortex in the rat. 3. Maturation of the components of the granular layer. *J Comp Neurol*, 145(4):465-513.

Arens, J., Stabel, J. and Heinemann, U. (1992). Pharmacological properties of excitatory amino acid induced changes in extracellular calcium concentration in rat hippocampal slices. *Can J Physiol Pharmacol,* 70:S194-205.

Bahjaoui-Bouhaddi, M., Padilla, F., Nicolet, M., Cifuentes-Diaz, C., Fellmann, D. and Mege, R. M. (1997). Localized deposition of M-cadherin in the glomeruli of the granular layer during the postnatal development of mouse cerebellum. *J Comp Neurol,* 378(2):180-95.

Bajaj, C. L., Coyle, E. J., Lin, K.-N. (1996) Arbitrary topology shape reconstruction from planar cross sections. *Graphical Models and Image Processing*, 58(6):524-543.

Bardoni, R. and Belluzzi, O. (1993). Kinetic study and numerical reconstruction of A-type current in granule cells of rat cerebellar slices. *J Neurophysiol,* 69(6):2222-31.

Bartol, T. M. Jr., Land, B. R., Salpeter, E. E., Salpeter, M., M. (1991). Monte Carlo simulation of miniature endplate current generation in the vertebrate neuromuscular junction. *Biophys J,* 59(6):1290-307.

Benninger, C., Kadis, J. and Prince, D. A. (1980). Extracellular calcium and potassium changes in hippocampal slices. *Brain Res,* 187:165-82.

Borst, J. G. and Sakmann, B. (1999). Depletion of calcium in the synaptic cleft of a calyx-type synapse in the rat brainstem, *J Physiol (London)* 521(1):123-133.

Brodal, P. and Bjaalie, J. G. (1997). Salient anatomic features of the cortico-ponto-cerebellar pathway. *Prog Brain Res,* 114:227-49.

Cathala, L., Holderith, N.B., Nusser, Z., DiGregorio, D.A., Cull-Candy, S.G. (2005). Changes in synaptic structure underlie the developmental speeding of AMPA receptor-mediated EPSCs. *Nat Neurosci*, 8(10):1310-8.

Chadderton, P., Margrie, T. and W., Hausser, M. (2004). Integration of quanta in cerebellar granule cells during sensory processing, *Nature,* 428(6985):856-60.

Courchesne. E. and Allen G. (1997). Prediction and preparation, fundamental functions of the cerebellum. *Learn Mem*, 4(1):1-35.

Crank, J. (1975). The Mathematics of Diffusion. *Oxford University Press*, USA.

D'Angelo, E., Rossi, P. and Taglietti, V. (1993). Different proportions of *N*-methyl-D-aspartate and non-*N*-methyl-D-aspartate receptor currents at the mossy fibre-granule cell synapse of developing rat cerebellum. *Neuroscience*, 53:121-130.

D'Angelo, E., De Filippi, G., Rossi, P., Taglietti, V. (1995). Synaptic excitation of individual rat cerebellar granule cells in situ: evidence for the role of NMDA receptors. *J Physiol*, 484 (Pt 2):397-413.

D'Angelo, E., Nieus, T., Maffei, A., Armano, S., Rossi, P., Taglietti, V., Fontana, A and Naldi, G. (2001). Theta-frequency bursting and resonance in cerebellar granule cells: experimental evidence and modeling of a slow k+-dependent mechanism. *J Neurosci*, 21(3):759-70.

D'Angelo, E., Rossi, P., Gall, D., Prestori, F., Nieus, T., Maffei, A. and Sola, E. (2005). Long-term potentiation of synaptic transmission at the mossy fiber-granule cell relay of cerebellum. *Prog Brain Res*, 2005;148:69-80.

De Schutter, E. and Bower, J. M. (1994). An active membrane model of the cerebellar Purkinje cell. I. Simulation of current clamps in slice. *J Neurophysiol*, 71(1):375-400.

DiGregorio, D., A., Nusser, Z. and Silver, R. A. (2002). Spillover of glutamate onto synaptic AMPA receptors enhances fast transmission at a cerebellar synapse. *Neuron*, 35:521–533.

Eagleman, D., M., Coenen, J-M. D., Mitnser, V., Bartol, T. M., Bell, T. A., Sejnowski, T. J. (2001). Cerebellar glomeruli: Does limited extracellular calcium implement a sparse encoding strategy? *Proceedings of the 8th Annual Joint Symposium on Neural Computation*.

Egelman, D. M., Montague, P. R. (1998). Computational properties of peri-dendritic

calcium fluctuations. *J Neurosci*, 18(21):8580-9.

Egelman, D. M. and Montague, P. R. (1999). Calcium dynamics in the extracellular space of mammalian neural tissue. *Biophys J*, 76(4):1856-67.

Forti, L. and Pietrobon, D. (1993). Functional diversity of 1-type calcium channels in rat
cerebellar neurons. *Neuron*, 10:437–450.

Forti L., Tottene A., Moretti A. and Pietrobon D. (1994) Three novel types of voltage-
dependent calcium channels in rat cerebellar neurons. *J Neurosci*, 14:5243–5256.

Franks, K. M., Bartol, T. M. Jr. and Sejnowski, T. J. (2002). A Monte Carlo model reveals independent signaling at central glutamatergic synapses. *Biophys J*, 83(5):2333-48.

Franks, K., M. and Sejnowski, T., J. (2002). Complexity of calcium signaling in synaptic
spines. *Bioessays,* 12:1130-44.

Franks, K., M., Stevens, C., F. and Sejnowski, T., J. (2003). Independent sources of quantal variability at single glutamatergic synapses. *J Neurosci*, 23(8):3186-95.

Furuta, A., Rothstein, J., D. and Martin, L., J. (1997). Glutamate transporter protein subtypes are expressed differentially during rat CNS development. *J. Neurosci,* 17(21):8363-75.

Gall, D., Roussel, C., Nieus, T., Cheron, G., Servais, L., D'Angelo, E. and Schiffmann, S.
N. (2005). Role of calcium binding proteins in the control of cerebellar granule cell neuronal excitability: experimental and modeling studies. *Prog Brain Res*, 148:321-8.

Garwicz, M., Jörntell H., Ekerot, C.-F. (1998). Cutaneous receptive fields and topography of mossy fibres and climbing fibres projecting to cat cerebellar C3 zone. *J Physiol,* 512(1): 277-293.

Hamon, B. and Heinemann, U. (1986). Effects of GABA and bicuculline on N-methyl-
D-aspartate- and quisqualate-induced reductions in extracellular free calcium in area CA1 of the hippocampal slice. *Exp Brain Res,* 64**:**27-36.

Hamori, J. and Somogyi, J. (1983). Differentiation of cerebellar mossy fiber synapses in
the rat: a quantitative electron microscope study. *J Comp Neurol,* 220(4):365-77.

Helmchen, F., Borst, J. G. and Sakmann, B. (1997). Calcium dynamics associated with a
single action potential in a CNS presynaptic terminal. *Biophys J,* 72: 1458-1471.

Hines, M. (1989). A program for simulation of nerve equations with branching geometries. *Intl J Biomed Comput*, 24:55-68.

Hines, M. (1993). Neuron - a program for simulation of nerve equations. In Eeckman,
FH (ed), *Neural Systems: Analysis and Modeling*, Kluwer Academic Publishers, Boston, MA, 127-136.

Hrabětová, S., Hrabe, J. and Nicholson, C. (2003). Dead-space microdomains hinder extracellular diffusion in rat neocortex during ischemia**.** *J Neurosci*, 23(23):8351-8359

Ito. M. (1984). *The Cerebellum and Neural Control*. Raven Press.

Jakab, R.L. and Hamori, J. (1988). Quantitative morphology and synaptology of cerebellar glomeruli in the rat. *Anatomy and Embryology (Berlin),* 179(1):81-88.

Jakab, R.L. (1989). Three-dimensional reconstruction and synaptic architecture of cerebellar glomeruli in the rat. *Acta Morphologica Hungarica,* 37(1-2):11-20.

Katz, B. and Miledi, R. (1970). Further study of the role of calcium in synaptic transmission. *J Physiol*, 207(3):789-801.

King, R.D., Wiest, M.C. and Montague, P.R. (2001). Extracellular calcium depletion as a
mechanism of short-term synaptic depression. *J Neurophysiol*, 85:1952-1959.

Koester, H., J. and Sakmann, B. (2000). Calcium dynamics associated with action potentials in single nerve terminals of pyramidal cells in layer 2/3 of the young rat neocortex. *J Physiol*, **529.3**: 625-646.

Kremer J. R., Mastronarde, D., N. and McIntosh, J. R. (1996). Computer visualization of
three-dimensional image data using IMOD. *J Struct Biol*, 116:71-76.

Kulik, A., Nakadate, K., Hagiwara, A., Fukazawa, Y., Luján, R., Saito, H., Suzuki, S., Futatsugi, A., Mikoshiba, K., Frotscher, M., Shigemoto R. (2004). Immunocytochemical localization of the α_{1A} subunit of the P/Q-type calcium channel in the rat cerebellum. *European J Neurosci* 19(8):2169–2178.

Lucke, A., Kohling, R., Straub, H., Moskopp, D., Wassmann, H. and Speckmann, E. J.
(1995). Changes of extracellular calcium concentration induced by application of excitatory amino acids in the human neocortex in vitro. *Brain Res,* 671:222-6.

Lehre, K. P. and Danbolt, N., C. (1998). The number of glutamate transporter subtype
molecules at glutamatergic synapses: chemical and stereological quantification in young adult rat brain. *J Neurosci*, 18(21):8751-7.

Lester, R., A. and Jahr, C., E. (1992). NMDA channel behavior depends on agonist affinity. *J Neurosci*, 12(2):635-43.

Maex, R. and DeSchutter, E. (1998). Synchronization of golgi and granule cell firing in a
detailed network model of the cerebellar granule cell layer. *J Neurophys,* 80(5):2521-37.

Magee, J. C. and Johnston, D. (1995b). Synaptic activation of voltage-gated channels in
the dendrites of hippocampal pyramidal neurons. *Science*, 268:301–304.

Maffei, A., Prestori, F., Rossi, P., Taglietti, V. and D'Angelo E. (2002). Presynaptic current changes at the mossy fiber-granule cell synapse of cerebellum during LTP. *J Neurophysiol*, 88(2):627-38.

Markram, H., Helm, P. J. and Sakmann, B. (1995). Dendritic calcium transients evoked
by single back-propagating action potentials in rat neocortical pyramidal neurons. *J Physiol,* 485 (Pt 1):1-20.

Marr, D. (1969). A theory of cerebellar cortex. *J Physiol,* **202**:437–470.

Mastronarde, D. N. (1997) Dual-axis tomography: an approach with alignment methods that preserve resolution, *J. Struct. Biol.* **120** :343–352.

Middleton, F. A. and Strick, P. L. (1997). Cerebellar output channels. *Int Rev Neurobiol*,
41:61-82.

Mintz, I. M., Sabatini, B. L. and Regehr, W. G. (1995). Calcium control of transmitter
release at a cerebellar synapse. *Neuron,* 15:675-88.

Mitchell, S., J. and Silver, R., A. (2000). GABA spillover from single inhibitory axons

suppresses low-frequency excitatory transmission at the cerebellar glomerulus, *J Neurosci*, 20(23):8651-8.

Nicholson, C., ten Bruggencate, G., Stockle, H. and Steinberg, R. (1978). Calcium and potassium changes in extracellular microenvironment of cat cerebellar cortex. *J Neurophysiol*, 41(4):1026-39.

Nicholson, C. and Sykova, E. (1998). Extracellular space structure revealed by diffusion analysis. *Trends Neurosci*, 21(5):207-15.

Nielsen, T., A., DiGregorio, D., A. and Silver, R., A. (2004). Modulation of glutamate mobility reveals the mechanism underlying slow-rising AMPAR EPSCs and the diffusion coefficient in the synaptic cleft. *Neuron,* 42(5):757-71.

Palay, S. and Chan-Palay V. (1974). *Cerebellar cortex. Cytology and Organization.* Springer, New York.

Pearson, H. A., Sutton, K. G., Scott, R. H. and Dolphin, A. C. (1995) Characterization of Ca^{2+} channel currents in cultured rat cerebellar granule neurones. *J Physiol*, 482:493–509.

Petralia, R. S., Wang, Y. X. and Wenthold R. J. (2002). NMDA receptors and PSD-95 are found in attachment plaques in cerebellar granular layer glomeruli. *European J Neurosci,* 15(3):583-587.

Randall, A. and Tsien, R. W. (1995). Pharmacological dissection of multiple types of Ca^{2+} channel currents in rat cerebellar granule neurons. *J Neurosci*, 15:2995–3012.

Randall, A. D. and Tsien, R. W. (1997). Contrasting biophysical and pharmacological properties of T-type and R-type calcium channels. *Neuropharmacol,* 36:879–893.

Rojas, H., Colina, C., Ramos M., Benaim, G., Jaffe, E. H., Caputo, C., DiPolo, R. (2007). Na^{+} entry via glutamate transporter activates the reverse Na^{+}/Ca^{2+} exchange and triggers -induced Ca^{2+} release in rat cerebellar Type-1 astrocytes. *J of Neurochem*, 100(5):1188–1202.

Rose, O.,Grund, C., Reinhardt, S.,Starzinski-Powitz A., Franke W.W. (1995). Contactus

adherens, a special type of plaque-bearing adhering junction containing M-cadherin, in the granule cell layer of the cerebellar glomerulus. *Proc Natl Acad Sci U S A,* 92(13): 6022–6026.

Rossi, P., D'Angelo, E., Magistretti, J., Toselli, M. and Taglietti, V. (1994). Age-dependent expression of high-voltage activated calcium currents during cerebellar granule cell development in situ. *Pflugers Arch*, 429(1):107-16.

Rossi, P., Sola, E., Taglietti, V., Borchardt, T., Steigerwald, F., Utvik, J. K., Ottersen, O.
P., Kohr, G. and D'Angelo E. (2002). NMDA receptor 2 (NR2) C-terminal control of NR open probability regulates synaptic transmission and plasticity at a cerebellar synapse. *J Neurosci,* 22(22):9687-97.

Rusakov, D.A. (2001). The role of peri-synaptic glial sheaths in glutamate spillover and
extracellular Ca2+ depletion. *Biophys J*, 81:1974-1959.

Rusakov, D. A. and Fine, A. (2003). Extracellular Ca2+ depletion contributes to fast activity-dependent modulation of synaptic transmission in the brain. *Neuron,* 37(2):287-97.

Sargent, P., B., Saviane, C., Nielsen, T., A., DiGregorio, D., A.and Silver, R., A. (2005).
Rapid vesicular release, quantal variability, and spillover contribute to the precision and reliability of transmission at a glomerular synapse. *J Neurosci*, 25(36): 8173-87.

Saviane, C. and Silver, R., A. (2006). Fast vesicle reloading and a large pool sustain high
bandwidth transmission at a central synapse. *Nature*, 439(7079):983-7.

Schramm, M., Vajna, R., Pereverzev, A., Tottene, A., Klockner, U., Pietrobon, D., Hescheler, J. and Schneider, T. (1999). Isoforms of α1E voltage-gated calcium channels in rat cerebellar granule cells – detection of major calcium channel α1-transcripts by reverse transcription-polymerase chain reaction. *Neuroscience,* 92:565–575.

Schweighofer, N., Doya, K. and Lay, F. (2001). Unsupervised learning of granule cell
sparse codes enhances cerebellar adaptive control. 103(1):35-50.

Silver, R., A., Traynelis, S., F. and Cull-Candy, S., G. (1992). Rapid-time-course miniature and evoked excitatory currents at cerebellar synapses in situ. *Nature,* 355(6356):163-6.

Smith, S. J. (1992). Do astrocytes process neural information? *Prog Brain Res*, 94:119-
36.

Stanley, E. F. (2000). Presynaptic calcium channels and the depletion of synaptic cleft
calcium ions. *J Neurophys,* 83:477-482.

Stiles, J., R. and Bartol, T., M., Jr. (2001). Monte Carlo methods for simulating realistic
synaptic microphysiology. In *Computational Neuroscience Realistic Modeling for Experimentalists*, E. de Schutter, editor. CRC press, Boca Raton, FL. 681-731.

Stiles, J., R., Bartol, T., M., Jr., Salpeter, M., M., Salpeter, E., E. and Sejnowski, T., J. (2001). Synaptic variability: new insights from reconstructions and Monte Carlo simulations with MCell. In *Synapses* W.M. Cowan, T.C. Sudhof, and C.F. Stevens, editors. Johns Hopkins University Press, Baltimore, MD. 87-128.

Sykova, E., (2004). Extrasynaptic volume transmission and diffusion parameters of the
extracellular space. *Neuroscience,* 129:861-876.

Sykova ,E. (2005). Glia and volume transmission during physiological and pathological
states. *J Neural Transm*, 112(1):137-47.

Tang, L., Hung, C., P., Schuman, E., M. (1998). A role for the cadherin family of cell adhesion molecules in hippocampal long-term potentiation. *Neuron,* 20(6):1165-75.

Tao, L. and Nicholson, C. (2004). Maximum geometrical hindrance to diffusion in brain
extracellular space surrounding uniformly spaced convex cells. *J Theor Biol*, 229(1):59-68.

Tottene, A., Moretti, A. and Pietrobon, D. (1996). Functional diversity of P-type and R.-
type calcium channels in rat cerebellar neurons. *J Neurosci*, 16:6353–6363.

Van Harreveld, A., Crowell, J. and Malhotra, S. K. (1965). A study of extracellular space
in central nervous tissue by freeze-substitution. *J Cell Biol*, 25(1):117-137.

Vassilev, P. M., Mitchel, J., Vassilev, M., Kanazirska, M. and Brown, E. M. (1997). Assessment of frequency-dependent alterations in the level of extracellular Ca2+ in the synaptic cleft. *Biophys J*, 72(5):2103-16.

Wiest, M. C., Eagleman, D. M., King, R. D., Montague, P. R. (2000). Dendritic spikes and their influence on extracellular calcium signaling. *J Neurophysiol*, 83(3):1329-37.

Xu-Friedman, M.A. and Regehr, W.G. (2003). Ultrastructural contributions to desensitization at cerebellar mossy fiber to granule cell synapses. *J Neurosci*, 23(6):2182-92.

Zanotto, L. and Heinemann, U. (1983). Aspartate and glutamate induced reductions in extracellular free calcium and sodium concentration in area CA1 of 'in vitro' hippocampal slices of rats. *Neurosci Lett,* 35:79-84.